Space-Time Adaptive Algorithms for Parabolic Problems: a Posteriori Error Estimates and Application to Microfluidics

THÈSE N^{O} 4338 (2009)

PRÉSENTÉE LE 6 MARS 2009

À LA FACULTE SCIENCES DE BASE

CHAIRE D'ANALYSE ET DE SIMULATION NUMÉRIQUE

PROGRAMME DOCTORAL EN MATHÉMATIQUES

ÉCOLE POLYTECHNIQUE FÉDÉRALE DE LAUSANNE

POUR L'OBTENTION DU GRADE DE DOCTEUR ÈS SCIENCES

PAR

Virabouth PRACHITTHAM

acceptée sur proposition du jury:

Prof. F. Eisenbrand, président du jury
Dr M. Picasso, directeur de thèse
Prof. M. Gijs, rapporteur
Prof. P. Hild, rapporteur
Prof. A. Lozinski, rapporteur

ÉCOLE POLYTECHNIQUE
FÉDÉRALE DE LAUSANNE

Suisse
2009

Abstract

We developed a space and time adaptive method to simulate electroosmosis and mass transport of a sample concentration within a network of microchannels.

The space adaptive criteria is based on an error estimator derived using anisotropic interpolation estimates and a post-processing procedure. In order to improve the accuracy of the numerical solution and to reduce even further the computational cost of the numerical simulation, a time adaptive procedure is combined with the one in space. To do so, a time error estimator is derived for a first model problem, the linear heat equation discretized in time with the Crank-Nicolson scheme. The main difficulty is then to obtain an optimal second order error estimator. Applying standard energy techniques with a continuous, piecewise linear approximation in time fail in recovering the optimal order. To restore the appropriate rate of convergence, a continuous piecewise quadratic polynomial function in time is needed. For this purpose, two different quadratic functions are introduced and two different time error estimators are then derived. It turns out that the second error estimator is more efficient than the first one when considering our adaptive algorithm. Thus, using the second quadratic polynomial, an upper bound for the error is derived for a second model problem, the time-dependent convection-diffusion problem discretized in time with the Crank-Nicolson scheme. The corresponding space and time error estimators are finally used for the numerical simulation of mass transport of a sample concentration within a complex network of microchannels driven by an electroosmotic flow and/or by a pressure-driven flow. Numerical results presented show the efficiency and the robustness of this approach.

Keywords: space and time adaptive method, a posteriori error estimates, anisotropic meshes, finite elements, electroosmotic flow, electrokinetic injection techniques, microfluidics.

Version abrégée

Une méthode adaptative en espace et en temps pour la simulation numérique des mécanismes d'écoulement électroosmotique d'une concentration d'échantillon à l'intérieur d'un réseau de micro-canaux est mise en oeuvre.

Le critère d'adaptation spatiale est basé sur un estimateur d'erreur obtenu en utilisant des estimations d'interpolation anisotrope et une procédure de post-traitement. Afin d'améliorer la précision de la solution et de réduire davantage le coût informatique de la simulation numérique, une procédure d'adaptation temporelle est couplée à celle en espace. Pour ce faire, un estimateur d'erreur en temps est d'abord obtenu pour un premier problème modèle, l'équation de la chaleur linéaire discrétisée en temps par un schéma de type Crank-Nicolson. La difficulté majeure réside dans l'obtention d'un estimateur d'erreur optimal du second ordre. L'application des techniques standards en énergie associées à un polynôme affine par morceaux en temps ne permet pas d'obtenir un estimateur d'erreur temporel possédant le bon ordre de convergence. Afin de l'obtenir une fonction polynomiale continue quadratique par morceaux en temps est nécessaire. Deux différentes fonctions quadratiques sont alors introduites et deux différents estimateurs d'erreur en temps sont ainsi obtenus. Le second estimateur d'erreur apparaît plus efficace que le premier dans notre algorithme adaptatif. Ainsi, en utilisant le second polynôme quadratique, une borne supérieure de l'erreur est ensuite obtenue pour un second problème modèle, le problème de convection-diffusion instationnaire discrétisé en temps par un schéma de type Crank-Nicolson. Les estimateurs d'erreur en espace et en temps correspondant sont finalement utilisés pour la simulation numérique du transport par écoulement électroosmotique et/ou par un écoulement induit par une différence de pression, d'une concentration d'échantillon à l'intérieur d'un réseau complexe de micro-canaux. Les résultats numériques présentés montrent l'efficacité et la robustesse de cette approche.

Mots clés: méthode adaptative en espace et temps, estimations d'erreur a posteriori, maillages anisotropes, éléments finis, écoulement électroosmotique, techniques d'injection électrocinétique, microfluidique.

Acknowledgments

I am deeply indebted to my supervisor, Dr Marco Picasso, for being an outstanding advisor throughout my PhD. His patient guidance, encouragements and excellent advices made this work successful. Merci Marco.

It is a pleasure to thank Prof. Jacques Rappaz for having accepted me in his group both as a researcher and a teaching assistant.

My sincere thanks go to Prof. Alexei Lozinski for the invaluable help he gave and for sharing his point of view on this work. Merci encore Alexei.

I also thank Prof. Martin A.M. Gijs and Dr Frédéric Lacharme for provided important insight into the physical aspects of microfluidics.

Prof. Patrick Hild, Prof. Martin A.M. Gijs and Prof. Alexei Lozinski who honored me by being part of my jury and by reading this work are gratefully acknowledged. I also thank Prof. Friedrich Eisenbrand, President of the jury.

I thank the Swiss National Science Foundation for its financial support.

J'aimerais aussi remercier tous les actuels ou anciens membres de la Chaire d'Analyse et Simulation Numériques pour l'excellente ambiance au sein de notre groupe. Tout spécialement Christophe et Gilles pour toutes ses binchs et bons moments passés ensemble pendant cette thèse.

Un très grand merci à mes amis pour toujours avoir été présents à mes cotés pendant toutes ses années. A Thibaut et Mathieu, deux véritables frères. Nathaël et Émilie pour leur soutien et les très nombreuses soirées partagées. Tous mes amis comme moi fadas de l'OM.

Enfin, un énorme merci à ma petite famille, ma grande soeur et mon petit frère, Vanmany et Édouard, Delphin pour mes pires lendemains, et à mon papa et ma maman pour tout ce qu'ils m'apportent. Merci beaucoup.

Contents

Introduction

Microfluidics is an emerging technology involving fluid dynamics in miniaturized systems. It has drawn a great attention over the last decade due to the development of an increasing number of applications in biomedical diagnosis and analysis. It has diverse and widespread applications intersecting many disciplinary field such as biology, material science, physics and chemistry. Some examples of application of microfluidics include drug delivery [1], genomic sequencing [2, 3], DNA sequencing [4], diagnostics [5].

One of the greatest challenges of microfluidics is the development of miniaturized chemical and biological analysis systems called Laboratory-on-a-Chip devices. A Lab-on-a-chip is a microscale chemical or biological laboratory built on a thin glass or polymer chip of only a few square centimeters, see Figure 1. This miniaturized laboratory is made of a network of microchannels, usually about 10-100 μm diameter and 0.1-10 cm length, which often integrates several microfluidics components such as pumps, valves, sensors and electrodes. These devices represent a complete micro-system of analysis and offer many advantages: significant reduction in the amounts of samples and reagents, usually a few nanoliters, a short time analysis, high throughput, automation and portability.

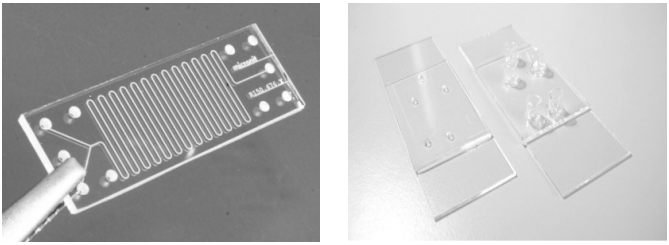

Figure 1. *Lab-on-a-chip device.*

One of the most important techniques practiced in a Lab-on-a-chip is capillary electrophoresis. This process is used to separate charged molecules under the influence of an applied electric field. It is a powerful separation technique that suits ideally for the handling of small amounts of liquid sample. Capillary electrophoresis is governed by two driving forces: electrophoresis and electroosmosis [6, 7, 8]. These two electrokinetic phenomena constitute the two main electrokinetic effects in micro and nano-scale transport applications. Indeed, the sample to be analyzed, introduced at one end of the capillary, moves inside the capillary under the effect of these two mechanisms. Electrophoresis is the movement of a charged molecule under an applied electric field; electroosmosis is the flow of the entire liquid in the microchannel or capillary, and consequently identical for each molecule, and occurs because of the charge surface of the wall of a narrow capillary. Indeed, most substrates acquire an electric charge in contact with an ionic solution. Then, at the fluid-solid interface, the resulting charged surface will attract the ions of the opposite charge, the so-called counterions, and repels the co-ions, the ions which have the same sign as the charge of the surface. Hence, an area will exist in which the concentration of counterions will be larger than that of the co-ions. This phenomenon leads to the formation of a thin charged layer known as the electric double layer (EDL) or the Debye layer. This EDL is composed of two layers, the first one, the Stern layer, immediately next to the charged solid surface where the ions are nearly immobile due to the strong electrostatic forces and the second layer, the Diffuse layer, in which there is an excess of counterions over co-ions and where the ions are mobile, see Figure 2. When an external electric

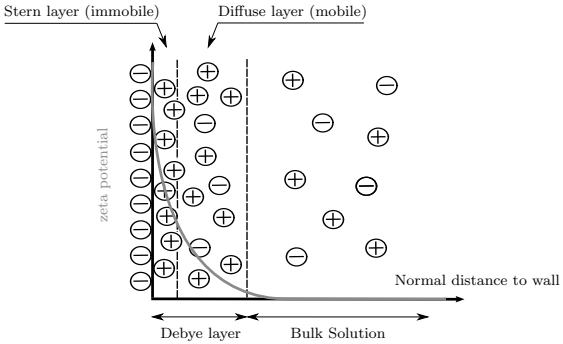

Figure 2. *Schematic representation of the zeta potential and the ionic concentration field near a negatively charged wall in contact with an ionic solution.*

field is applied over the microchannel or capillary, the counterions in the Diffuse layer of the EDL, not attracted by the channel surface, migrate in the direction of their opposite potential and drag the surrounding liquid molecules with them because of the viscous effect. This is known as electroosmosis and leads to a bulk liquid motion. The resulting electroosmotic flow (EOF) rate is generally greater than the electrophoretic migration velocity of each individual species. Thus, under an applied electric field, even if the molecules move according to their charge within the capillary, the EOF rate is usually strong enough to drag all the charged species in the same direction. Finally, the difference in electrophoretic mobility of the sample constituents cause them to separate.

As the EOF is the leading electrokinetic phenomenon used in microfluidic devices, we will particularly focus on this kind of transport and thus treat the electroosmotic transport of a sample concentration within a network of microchannels. A fundamental characteristic of EOF is the electric wall potential across the Debye layer. In the Stern layer, because of the strong attraction of counterions onto the charged solid surface, an electric wall potential is created which drops rapidly across the Debye layer to a constant value at the walls, the so-called zeta potential, to zero in the bulk region, see Figure 2. As the thickness of the EDL is very thin compared to the capillary diameter, the estimation of this potential is a challenging task when considering its numerical simulation. The key issue of simulating EOF is then to compute accurately and efficiently this double layer potential. Some characteristic scales and typical physical parameters are given in Table 1. Thus, the ratio between the channel height and the Debye layer can be up to 10^4. Therefore, the numerical method used to solve the EDL potential across the channel diameter has to provide an accurate solution with a reasonable computation cost. We will take up these numerical challenges using an adaptive finite element method. With this method the mesh grid will be automatically refined in the EDL region ensuring the strong variation of the wall potential to be captured

Parameter	Value
Channel length (m)	1e-2 $\sim$ 1e-1
Channel diameter (m)	1e-5 $\sim$ 1e-4
Debye layer length (m)	1e-9 $\sim$ 1e-6
Zeta potential (mV)	-50 $\sim$ 50
Reynold number, Re	1e-5 $\sim$ 1

Table 1. *Typical physical parameters in electrokinetic driven flows.*

accurately. Thus, instead of assuming a slip electroosmotic condition at the walls, avoiding the computation of the EDL potential, we will be able to fully solve the EDL potential near the capillary walls required to solve the EOF. Moreover this approach is particularly well appropriate for the study of a sample concentration in complex microchannel geometries, see Figure 3 for a schematic representation of two anisotropic meshes used at two different times for the transport of a sample concentration in a straight channel.

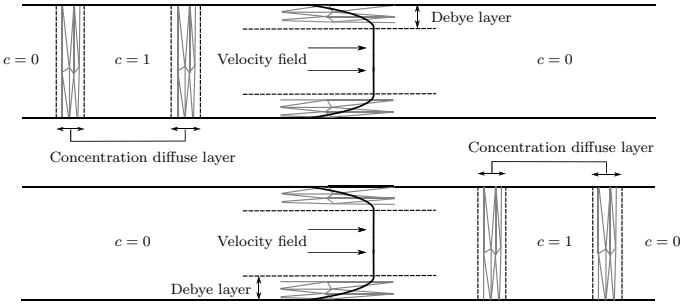

Figure 3. *Schematic representation of two anisotropic meshes used at two different times for the transport of a sample concentration in a straight channel. The mesh has to be refined along the Debye layer but also along the diffuse layer of the concentration field c.*

In general, capillary electrophoresis analysis takes place in two steps: the injection and the separation processes. During the injection process or the loading step, an amount of the sample concentration, the sample plug, is confined at the entrance of the separation channel. In the separation step, this amount is injected in the separation channel where the sample constituents will be separated according to their electrophoretic mobilities. In Figure 4, we present the numerical simulation of the injection and separation processes in a multiple T-form channel. The sample concentration is represented by a white concentration field varying from a value of zero to one. This concentration is driven through the injection channel by an EOF which made the sample moves from the bottom channel to the three top channels (first and second pictures). Then, an amount of the sample concentration, loaded at the center of the cross section, will be injected in the separation channel (third picture). In Figure 5, we can appreciate the mesh corresponding to the first picture presented in Figure 4. At this moment the sample concentration separates in three and starts to move into the three top channels. We can observe

that the mesh is refined at the propagation front of the sample concentration, where its value varies from zero to one, and near the channel walls in order to compute accurately the EDL potential. Thus, in a network of microchannels, the adaptive finite element method allows to obtain accurate solutions of sample mass transport driven by an EOF by refining the mesh wherever needed but also by coarsening the mesh where the solution does not present any variation, reducing then drastically the computational cost of the numerical simulation.

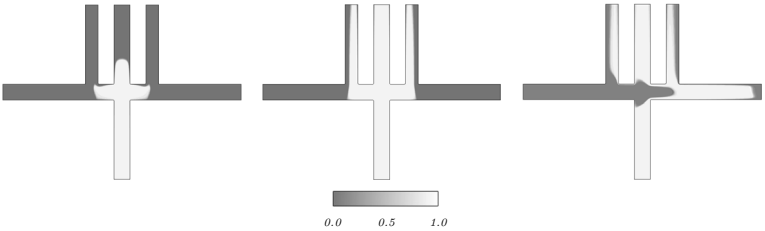

Figure 4. *From left to right: injection process, final time of the injection process and separation process of an injection and separation processes in a multiple T-form channel.*

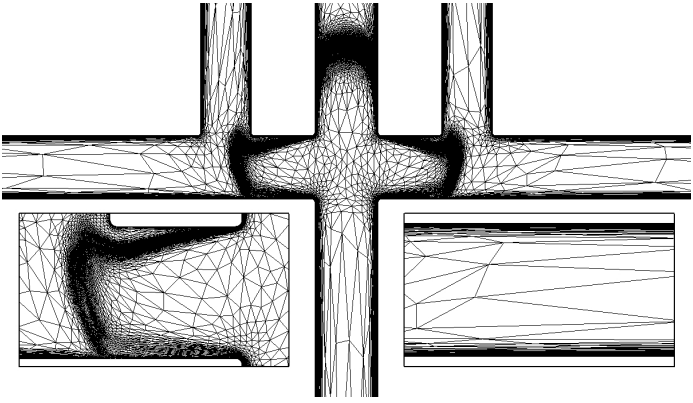

Figure 5. *Zoom on the adapted mesh during the injection process in a multiple T-form channel.*

The refinement and coarsening criteria in adaptive finite element methods rely on a posteriori error estimation. The goal is to bound the true error, the difference between the exact solution and the numerical solution, by an easily computable quantity, the so-called error estimator. Let u and u_h be the exact and the numerical solution of a given problem. Then in a posteriori error analysis, the goal is to find an error estimator η which depends only on the data and the discrete solution such that there exists two constants positive C_1 and C_2 independent of the exact solution u and the typical mesh size h such that

$$C_1\eta \leq \|u - u_h\| \leq C_2\eta,$$

where $\|\cdot\|$ is an appropriate norm, usually the energy norm of the problem. Thus, based on information given by the derived error estimator, adaptive procedures try to automatically refine or coarsen a mesh and/or increase or decrease the time step size so as to compute an accurate numerical solution in an optimal manner. Given an initial mesh or time step size, the adaptive procedure at each time step consists in the three following steps

$$\texttt{Solve} \rightarrow \texttt{Estimate} \rightarrow \texttt{Refine/Coarsen or Increase/Decrease}.$$

This procedure is repeated until the a posteriori error estimator is within a prescribed tolerance. The use of a posteriori error estimator is nowadays an efficient tool to control the quality of numerical solutions of partial differential equations. Rigorous analysis of a posteriori error estimates started with the pioneering work of Babuška and Rheinboldt [9, 10]. An impressive amount of work is now available for a huge number of problems, as evidenced by the reviews [11, 12, 13, 14] and the references therein. Recently, anisotropic a posteriori error estimates have received much more attention, see for instance [15, 16, 17, 18, 19, 20, 21, 22]. The goal is to use finite elements with large aspect ratio in order to reduce even more the number of degrees of freedom and hence the computational cost of the numerical simulation. Finite elements can thus be stretched in the desired direction, that is to say aligned along the boundary layers. Most of anisotropic adaptive finite element algorithms used error estimators based on the approximation of the Hessian matrix of the solution, see for instance [23, 24, 25, 26, 27]. Such approximations can be difficult to achieve when using a first order finite element method. An alternative anisotropic error estimator has then been proposed in [28] which requires only a first order gradient matrix. The anisotropic error estimator has been derived using the interpolation results of [23, 24] and equivalence to the true error has been proved in the case of the Laplace problem in [29]. This error estimator has been extended in [30] to elliptic and parabolic problems but also to nonlinear parabolic systems [31, 22]. Thus, we pursue the approach of [28, 30, 29] and develop a space and time adaptive algorithm, with possibly large aspect ratio finite elements, to

simulate electroosmosis and mass transport of a sample concentration within a complex network of microchannels.

This thesis consists in two parts. In a first part, we derive a posteriori error estimators for two model problems: the heat equation and the time-dependent convection-diffusion problem, both discretized in time using the Crank-Nicolson method. Concerning parabolic problems and the Crank-Nicolson scheme, it was observed in Section 2.1 of [32] that standard energy technique applying with a continuous piecewise linear approximation in time would fail in recovering an optimal second order time error estimator. The so-called Crank-Nicolson reconstruction was then introduced in order to restore the appropriate rate of convergence. In [32] this reconstruction is considered in the case of a semi-discrete time discretization of a general parabolic problem. In the present work, we are interested in the fully discrete situation taking first the example of a simpler problem, the classical linear heat equation. We extend the results of [32] to the fully discrete case by introducing piecewise quadratic time reconstructions of the numerical solution and using them to obtain a posteriori error estimates. We introduce two piecewise quadratic time reconstructions, the first one directly transposed from [32] and the second one based on a finite difference approximation of $\partial^2 u/\partial t^2$. It turns out that the second error estimator, based on the second reconstruction, is more efficient than the first one. In particular, the second error indicator is of optimal order with respect to both the mesh size and the time step when using our adaptive algorithm. Then, based on experiments taken from this first model problem, an a posteriori upper bound is derived for a second model problem, the time-dependent convection-diffusion problem discretized in time using the Crank-Nicolson method. Numerical experiments illustrating the efficiency of this approach are reported and show the same conclusions draw for the heat equation, that is to say an optimal order of convergence with respect to both the mesh size and the time step, even in the convection dominated regime and in presence of boundary layers.

Based on the space and time errors estimators derived from the time-dependent convection-diffusion problem, the second part focuses on it application to microfluidics with the numerical simulation of EOF and mass transport of a sample concentration within a network of microchannels. We introduce the EOF model used to transport the sample concentration and develop a space and time adaptive algorithm. It is based on error estimators already presented for parabolic problems [29] and the Stokes problem [33] but also on new error estimators derived from the time-dependent convection-diffusion problem using the Crank-Nicolson scheme. The space adaptive algorithm will couple three error estimators derived from the EDL potential problem, the Stokes problem and the convection-diffusion

problem. As regards the time adaptive algorithm, it is only based on an error estimator derived from the concentration field. To conclude, numerical experiments are carried out: injection and separation processes in crossing and multiple T-form configuration channels and combined EOF and pressure-driven technique in a double T-shape channel.

Note that the following three Chapters have been submitted to publication and all results can be found in [34, 35, 36].

Chapter 1

A posteriori error estimator for the Crank-Nicolson scheme. First model problem: The heat equation

In this Chapter we derive two a posteriori upper bounds for the heat equation. A continuous, piecewise linear finite element discretization in space and the Crank-Nicolson method for the time discretization are used. The error due to the space discretization is derived using anisotropic interpolation estimates and a post-processing procedure. The error due to the time discretization is obtained using two different continuous, piecewise quadratic time reconstructions. The first reconstruction is developed following [32], while the second one is new. An adaptive algorithm is developed. Numerical studies are reported for several test cases and show that the second time error estimator is more efficient than the first one. In particular, the second time error indicator is of optimal order with respect to both the mesh size and the time step when using our adaptive algorithm.

Contents

1.1 Situation

A posteriori error analysis is at the base of refinement/coarsening procedures in mesh adaptivity techniques. An impressive amount of work is available for a huge number of problems, as evidenced by the reviews [11, 12, 13, 14] and the references therein. The goal is to derive an easily computable bound of the error in order to ensure global control of the solution. The theory is particularly well developed in the case of elliptic problems, see for instance [37, 38, 39, 40]. In the case of parabolic problems, most papers deal with the Euler implicit discretization in time, see for instance [41, 42, 43], or higher order discontinuous Galerkin methods [44, 45]. However, little attention was paid to the popular Crank-Nicolson method for parabolic problems. In [46], an A-stable θ-scheme was considered for the time discretization of the heat equation and a posteriori bounds were then derived applying standard energy techniques with a continuous, piecewise linear approximation in time. However, when considering the case $\theta = 1/2$, which yields to the Crank-Nicolson scheme, the term measuring the error due to the time discretization is of suboptimal order with respect to time. In order to restore the appropriate second order of convergence, Akrivis et al. suggested in [32, 47] to work with a continuous, piecewise quadratic polynomial function in time rather than a linear one. The so-called Crank-Nicolson reconstruction was then introduced. In [32] this reconstruction, that can be explicitly constructed from the numerical solution, is considered in the case of a semi-discrete time discretization of a general parabolic problem. This approach is generalized in [47] to Runge-Kutta and Galerkin methods.

In the present Chapter, we are interested in the fully discrete situation taking the example of the linear heat equation, $\partial u/\partial t - \Delta u = f$, discretized in space by continuous piecewise linear finite elements and in time by the Crank-Nicolson method. We extend the results of [32] to the fully discrete case by introducing piecewise quadratic time reconstructions of the numerical solution and using them to obtain a posteriori error estimates. We consider two reconstructions. The first one is a direct transposition of the reconstruction from [32] to the fully discrete setting whereas the second one is new. It is based on a finite difference approximation of $\partial^2 u/\partial t^2$ rather than an approximation of $\partial f/\partial t + \Delta(\partial u/\partial t)$. A posteriori upper bounds are derived for both reconstructions and are used to construct an adaptive algorithm for both the time step and the space step. Numerical experiments show that the first error estimator does not lead to an optimal rate of convergence with respect to the time step when using our adaptive algorithm, especially in situations when the error is mainly due to the space discretization. On the contrary, the second error estimator always provides a fair representation of the true error. Another feature of this work is the use of finite elements on highly anisotropic

triangulations. We pursue the approach to anisotropic finite elements developed in papers [41, 30, 29], which are in turn based on the theory developed in [23, 24]. The theory is thus presented in the anisotropic framework and the numerical tests are done on examples that lead naturally to highly stretched meshes. Note however, that a posteriori error bounds can be applied also in the isotropic setting, that is to say when the triangulation satisfies the minimum angle condition.

The outline of the Chapter is as follows. In the next Section, we present the model problem and its space and time discretization. We will then introduce in Section 1.3 some definitions and notations relative to the mesh anisotropy. The a posteriori error estimates for the two reconstructions are presented in Section 1.4. Section 1.5 is devoted to the description of an adaptive algorithm in space and time. A numerical study is carried out for several test cases in Section 1.6.

1.2 The heat equation and its discretization

Consider a polygonal domain Ω of $\mathbb{R}^2$ with boundary $\partial\Omega$. Given a final time $T > 0$, a function $f : \Omega \times (0,T) \to \mathbb{R}$ and an initial condition $u^0 : \Omega \to \mathbb{R}$, we consider the following problem: find $u : \Omega \times (0,T) \to \mathbb{R}$ such that

$$\begin{cases} \dfrac{\partial u}{\partial t} - \Delta u = f & \text{in } \Omega \times (0,T), \\ u = 0 & \text{on } \partial\Omega \times (0,T), \\ u(\cdot,0) = u^0 & \text{in } \Omega. \end{cases} \tag{1.1}$$

For the sake of simplicity, homogeneous Dirichlet boundary condition are considered. However, the analysis can be extended to mixed Dirichlet-Neumann boundary conditions. We suppose henceforth $f \in L^2(0,T;H^{-1}(\Omega))$, $u^0 \in L^2(\Omega)$ and seek (see for example [48]) a solution $u \in W$ with

$$W = \{w \in L^2(0,T;H_0^1(\Omega)) \text{ and } \partial w/\partial t \in L^2(0,T;H^{-1}(\Omega))\}$$

such that $u(\cdot,0) = u^0$ and

$$\left\langle \frac{\partial u}{\partial t}, v \right\rangle + \int_\Omega \nabla u \cdot \nabla v \, dx = \langle f, v \rangle \quad \forall v \in H_0^1(\Omega) \text{ and a.e. } t \in (0,T), \tag{1.2}$$

where $< \cdot, \cdot >$ denotes the duality pairing between $H^{-1}(\Omega)$ and $H_0^1(\Omega)$. In order to describe the time discretization corresponding to (1.2), we introduce a partition of the interval [0,T] into subintervals $I_n = [t^{n-1}, t^n]$, $n = 1, \ldots, N$, such that $0 = t^0 < t^1 < \cdots < t^N = T$ and we denote the time steps by $\tau_n = t^n - t^{n-1}$. For

any $0 < h < 1$, let $\mathcal{T}_h$ be a conforming triangulation of $\overline{\Omega}$ into triangles K (not necessarily satisfying the minimum angle condition) with diameter h_K less than h. We define by V_h the usual finite element space of continuous, piecewise linear functions on $\mathcal{T}_h$:

$$V_h = \left\{ v_h \in \mathcal{C}^0(\overline{\Omega});\ v_{h|K} \in P_1;\ \forall K \in \mathcal{T}_h \right\}$$

and we set

$$V_h^0 = V_h \cap H_0^1(\Omega).$$

We suppose that $f \in C^0([0,T]; L^2(\Omega))$ and $u^0 \in C^0(\overline{\Omega})$. We set $f^n(\cdot) = f(\cdot, t^n)$ and we compute $u_h^0 = r_h u^0$ where r_h is the Lagrange interpolant corresponding to V_h^0. The Crank-Nicolson scheme consists in seeking $u_h^n \in V_h^0$, for all $n = 1, \ldots, N$, such that for all $v_h \in V_h^0$

$$\int_\Omega \frac{u_h^n - u_h^{n-1}}{\tau_n} v_h \, dx + \frac{1}{2} \int_\Omega \left(\nabla u_h^n + \nabla u_h^{n-1} \right) \cdot \nabla v_h \, dx = \frac{1}{2} \int_\Omega (f^n + f^{n-1}) v_h \, dx. \tag{1.3}$$

Throughout this Chapter the following notations will be used. For all $n = 1, \ldots, N$, we set

$$\partial_n u_h = \frac{u_h^n - u_h^{n-1}}{\tau_n}, \quad u_h^{n-1/2} = \frac{1}{2}(u_h^n + u_h^{n-1})$$

and

$$\partial_n f = \frac{f^n - f^{n-1}}{\tau_n}, \quad f^{n-1/2} = \frac{1}{2}(f^n + f^{n-1}), \quad t^{n-1/2} = \frac{1}{2}(t^n + t^{n-1}). \tag{1.4}$$

With these notations, we can rewrite (1.3) as

$$\int_\Omega \partial_n u_h \ v_h \, dx + \int_\Omega \nabla u_h^{n-1/2} \cdot \nabla v_h \, dx = \int_\Omega f^{n-1/2} v_h \, dx, \tag{1.5}$$

for all $v_h \in V_h^0$. As in [41], we introduce the continuous, piecewise linear approximation in time defined for all $t \in I_n$ by

$$\begin{aligned} u_{h\tau}(x,t) &= \frac{t - t^{n-1}}{\tau_n} u_h^n + \frac{t^n - t}{\tau_n} u_h^{n-1} \\ &= u_h^{n-1/2} + (t - t^{n-1/2}) \partial_n u_h. \end{aligned} \tag{1.6}$$

So for all $v_h \in V_h^0$, (1.3) or (1.5) can be rewritten as

$$\begin{aligned} \int_\Omega \partial_n u_h \ v_h \, dx + \int_\Omega \nabla u_{h\tau} \cdot \nabla v_h \, dx &= \int_\Omega f^{n-1/2} v_h \, dx \\ &+ (t - t^{n-1/2}) \int_\Omega \nabla \partial_n u_h \cdot \nabla v_h \, dx. \end{aligned} \tag{1.7}$$

1.3 Anisotropic finite elements

In order to describe the mesh anisotropy we introduce some definitions and properties taken from [23, 24]. Alternative notations can be found using the framework of [15, 18]. For any triangle K of $\mathcal{T}_h$, we consider $T_K : \widehat{K} \to K$, the affine application which maps the reference triangle $\widehat{K}$ into K. Let $M_K \in \mathbb{R}^{2\times 2}$ and $t_K \in \mathbb{R}^2$ be the matrix and the vector defining such a map, we have

$$x = T_K(\hat{x}) = M_K \hat{x} + t_K \quad \forall \hat{x} \in \widehat{K}.$$

Since M_K is invertible, it admits a singular value decomposition

$$M_K = R_K^T \Lambda_K P_K,$$

where R_K and P_K are orthogonal and Λ_K is diagonal with positive entries. In the following we set

$$\Lambda_K = \begin{pmatrix} \lambda_{1,K} & 0 \\ 0 & \lambda_{2,K} \end{pmatrix} \quad \text{and} \quad R_K = \begin{pmatrix} r_{1,K}^T \\ r_{2,K}^T \end{pmatrix} \tag{1.8}$$

with the choice $\lambda_{1,K} \geq \lambda_{2,K}$. A simple example of such a transformation is $x_1 = H\hat{x}_1$, $x_2 = h\hat{x}_2$, with $H \geq h$. We can see in Figure 1.1 this transformation with

$$M_K = \begin{pmatrix} H & 0 \\ 0 & h \end{pmatrix} \quad \text{where} \quad \lambda_{1,K} = H, \quad \lambda_{2,K} = h,$$

$$r_{1,K} = \begin{pmatrix} 1 \\ 0 \end{pmatrix} \text{ and } r_{2,K} = \begin{pmatrix} 0 \\ 1 \end{pmatrix}.$$

Another example of such a transformation is given by Figure 1.2. We consider here the case when $\widehat{K}$ is an equilateral triangle with vertices lying on the unit circle. It is easy to see that the image of the unit circle by T_K is an ellipse with directions $r_{1,K}$ and $r_{2,K}$, the amplitudes of stretching being $\lambda_{1,K}$ and $\lambda_{2,K}$.

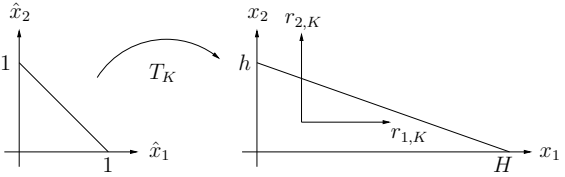

Figure 1.1. *Example of affine transformation T_K of a reference triangle $\widehat{K}$ into K.*

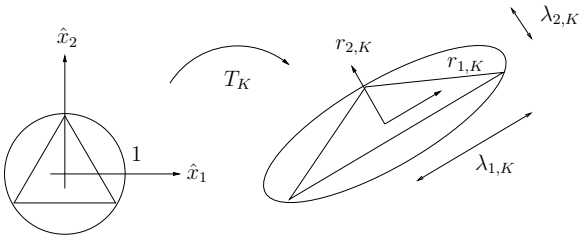

Figure 1.2. *Example of affine transformation T_K of a reference equilateral triangle $\widehat{K}$ into an isosceles triangle K. The unit circle is mapped into an ellipse with directions $r_{1,K}$ and $r_{2,K}$, the amplitudes of stretching being $\lambda_{1,K}$ and $\lambda_{2,K}$.*

In the context of anisotropic meshes, the classical minimum angle condition is not required. However, for each vertex, the number of neighboring vertices should be bounded from above, uniformly with respect to the mesh size h. Also, for each triangle K of the mesh, there is a restriction related to the patch Δ_K, the set of triangles of $\mathcal{T}_h$ having a common vertex with K. More precisely, the diameter of the reference patch $\Delta_{\widehat{K}} = T_K^{-1}(\Delta_K)$ must be uniformly bounded independently of the geometry. This assumption prevents, loosely speaking, the stretching directions, $r_{1,K}$ and $r_{2,K}$, from changing too abruptly between the adjacent triangles of the mesh, see Figure 1.3 for examples of acceptable and non acceptable patches. We suppose that the meshes meet the above mentioned restrictions which is the case of the BL2D anisotropic mesh generator [49] that we use. Let us now recall some interpolation results on anisotropic meshes proved in [24, 23, 50].

Proposition 1.3.1 ([24, 23, 50])**.** *Let $I_h : H_0^1(\Omega) \to V_h^0$ be the Clément interpolation operator [51]. There is a constant C independent of the mesh size and aspect ratio such that, for any $v \in H^1(\Omega)$ and any $K \in \mathcal{T}_h$ we have:*

$$\|v - I_h v\|_{L^2(K)} \leq C\omega_K(v),$$

$$\lambda_{2,K}\|\nabla(v - I_h v)\|_{L^2(K)} \leq C\omega_K(v),$$

$$\|v - I_h v\|_{L^2(\partial K)} \leq C\frac{1}{\lambda_{2,K}^{1/2}}\omega_K(v).$$

Here $\omega_K(v)$ is defined by

$$\omega_K^2(v) = \lambda_{1,K}^2 \left(r_{1,K}^T G_K(v) r_{1,K}\right) + \lambda_{2,K}^2 \left(r_{2,K}^T G_K(v) r_{2,K}\right),$$

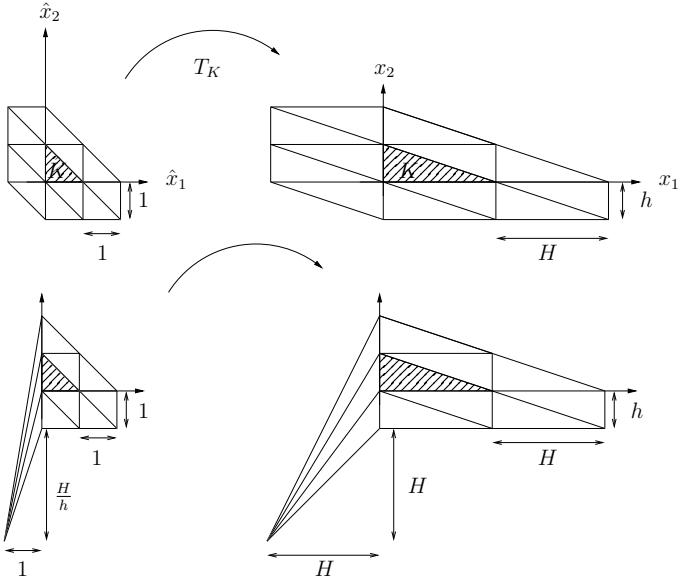

Figure 1.3. *Example of an acceptable patch (top): the size of the reference patch $\Delta_{\widehat{K}}$ does not depend on the aspect ratio H/h. Example of a non acceptable patch (bottom): the size of the reference patch $\Delta_{\widehat{K}}$ now depends on the aspect ratio H/h.*

$\lambda_{i,K}$ and $r_{i,K}$ are given by (1.8) and $G_K(v)$ is the following 2×2 matrix

$$G_K(v) = \sum_{T \in \Delta_K} \begin{pmatrix} \displaystyle\int_T \left(\frac{\partial v}{\partial x_1}\right)^2 dx & \displaystyle\int_T \frac{\partial v}{\partial x_1}\frac{\partial v}{\partial x_2} dx \\ \displaystyle\int_T \frac{\partial v}{\partial x_1}\frac{\partial v}{\partial x_2} dx & \displaystyle\int_T \left(\frac{\partial v}{\partial x_2}\right)^2 dx \end{pmatrix},$$

where $\triangle_K$ represents the set of triangles of $\mathcal{T}_h$ having a common vertex with K.

Remark 1.3.2. *The reader should note that similar interpolation error estimates can be found in [15, 18]. We can refer to Section 2 Remark 3 of [33] for a comparison of both anisotropic interpolation estimates in a similar context.*

1.4 A posteriori error estimates

1.4.1 Piecewise quadratic time reconstructions

It was observed in [32] that a direct use of $u_{h\tau}$ in an a posteriori error analysis of the Crank-Nicolson scheme would lead to a suboptimal estimate. It was proposed there to work rather with a piecewise quadratic time reconstruction of the numerical solution. We now recall briefly the construction of [32] made for a Crank-Nicolson discretization of an abstract evolutionary equation,

$$\frac{\partial u}{\partial t} + Au = f(t),$$

posed in a Hilbert space V, where A is a positive definite, selfadjoint, linear operator on V with the dense domain in V. We discretize the last equation in time as

$$\frac{u^n - u^{n-1}}{\tau_n} + A\frac{u^n + u^{n-1}}{2} = \frac{f(t^n) + f(t^{n-1})}{2} \tag{1.9}$$

and consider the linear interpolation

$$u_\tau(t) = u^{n-1} + (t - t^{n-1})\frac{u^n - u^{n-1}}{\tau_n}, \quad t \in I_n,$$

and the quadratic one

$$\widehat{u}_\tau(t) = u_\tau(t) + \frac{1}{2}(t - t^{n-1})(t - t^n)\left(\frac{f(t^n) - f(t^{n-1})}{\tau_n} - A\frac{u^n - u^{n-1}}{\tau_n}\right), \quad t \in I_n, \tag{1.10}$$

see (3.5) in [32] in which we replace $f(t^{n-\frac{1}{2}})$ with $(f(t^n)+f(t^{n-1}))/2$ in accordance with (1.9). The latter reconstruction allows an a posteriori error estimate to be obtained for (1.9), which is of optimal second order.

We return now to the heat equation (1.2) and its discretization (1.3) or equivalently (1.5). Comparing (1.5) and (1.9) we can interpret the operator A in (1.5) as the finite dimensional approximation of $-\Delta$ in (1.5). This analogy allows us to introduce the following quadratic reconstruction,

$$\widehat{u}_{h\tau}(x,t) = u_{h\tau}(x,t) + \frac{1}{2}(t - t^{n-1})(t - t^n)w_h^n, \quad t \in I_n,\ 1 \le n \le N, \tag{1.11}$$

where $w_h^n \in V_h^0$ is defined by

$$\int_\Omega w_h^n v_h \, dx = \int_\Omega (\partial_n f \; v_h - \nabla\partial_n u_h \cdot \nabla v_h) \, dx \quad \forall v_h \in V_h^0. \tag{1.12}$$

This reconstruction is the analogue of (1.10) in the case of the heat equation discretized both in space and in time. We will refer to $\widehat{u}_{h\tau}$ as the two-point reconstruction since it involves only u_h^n and u_h^{n-1}. We will use it to construct an upper bound for the error analogous to that of [32]. However, the use of the time error estimator based on $\widehat{u}_{h\tau}$ in our adaptive algorithm does not lead to the optimal rate of convergence with respect to the time step. That is why we propose in the next paragraph an alternative quadratic reconstruction.

As a motivation, we observe that w_h^n in (1.11) is formally an approximation of $\partial f/\partial t + \Delta \partial u/\partial t$ in the time slab I_n. And the latter is equal to $\partial^2 u/\partial t^2$ by (1.1). It seems natural then to try to replace w_h^n in (1.11) by a finite difference approximation of $\partial^2 u/\partial t^2$. We introduce thus

$$\widetilde{u}_{h\tau}(x,t) = u_{h\tau}(x,t) + \frac{1}{2}(t-t^{n-1})(t-t^n)\partial_n^2 u_h, \quad t \in I_n,\ 2 \le n \le N, \tag{1.13}$$

where

$$\partial_n^2 u_h = \frac{\dfrac{u_h^n - u_h^{n-1}}{\tau_n} - \dfrac{u_h^{n-1} - u_h^{n-2}}{\tau_{n-1}}}{(\tau_n + \tau_{n-1})/2}.$$

Note that $\widetilde{u}_{h\tau}$ is again continuous piecewise quadratic in time. We will refer to it as the three-point quadratic reconstruction since it involves u_h^n, u_h^{n-1} and u_h^{n-2}. Note that $u_{h\tau}$, $\widehat{u}_{h\tau}$ and $\widetilde{u}_{h\tau}$ coincide at all times $t^1, \dots, t^N$.

Remark 1.4.1. *The reconstruction $\widetilde{u}_{h\tau}$ restricted to the time interval I_n is the unique quadratic polynomial which coincides with u_h^{n-2}, u_h^{n-1}, u_h^n at time t^{n-2}, t^{n-1}, t^n, respectively. Indeed, denoting the latter by $P_n(x,t)$ we observe that it is equal to $u_{h\tau}$ at $t = t^{n-1}$ and $t = t^n$ and $u_{h\tau}$ is linear in time on I_n. Hence necessarily*

$$P_n(x,t) = u_{h\tau}(x,t) + C_n(x)(t-t^{n-1})(t-t^n)$$

for some $C_n \in V_h^0$. Then, we find C_n deriving P_n twice with respect to t and taking into account that $P_n(\cdot, t^{n-2}) = u_h^{n-2}$. We thus find that $C_n = \partial_n^2 u_h/2$ and recover (1.13).

Remark 1.4.2. *The requirement for w_h^n to vanish on the boundary may seem useless. However, since w_h^n can be interpreted as an approximation of $\partial f/\partial t + \Delta \partial u/\partial t = \partial^2 u/\partial t^2$ and since u is equal to zero on $\partial\Omega$, then $\partial^2 u/\partial t^2$ also vanishes on $\partial\Omega$. Consequently, it is reasonable to define w_h^n as an element of V_h^0.*

1.4.2 The upper bounds for the error

We will now present the two error indicators based on $\widehat{u}_{h\tau}$ and $\widetilde{u}_{h\tau}$ and used subsequently in our adaptive algorithm. In both cases, a standard energy technique is used that leads to combined error indicators in space and time. The estimator in space is similar to the one considered in [30, 29]. In what follows we keep the notations of Sections 1.2 and 1.4.1 and set $e = u - u_{h\tau}$, $\widehat{e} = u - \widehat{u}_{h\tau}$ and $\widetilde{e} = u - \widetilde{u}_{h\tau}$. We announce now our main results:

Theorem 1.4.3. *Let $\widehat{f}$ be the linear interpolant of f defined by*

$$\widehat{f}(\cdot,t) = \frac{t-t^{n-1}}{\tau_n} f^n + \frac{t^n - t}{\tau_n} f^{n-1}, \quad t \in I_n,\ 1 \le n \le N,$$

and suppose that the mesh is such that there exists a constant c independent of the time step, mesh size and aspect ratio such that

$$\lambda_{1,K}^2 \left(r_{1,K}^T G_K(\widehat{e}) r_{1,K} \right) \le c \lambda_{2,K}^2 \left(r_{2,K}^T G_K(\widehat{e}) r_{2,K} \right) \quad \forall K \in \mathcal{T}_h. \tag{1.14}$$

Then there is a constant C independent of the time step, mesh size and aspect ratio such that

$$\begin{aligned}
\int_0^T \|\nabla e\|_{L^2(\Omega)}^2 \, dt + \|e(\cdot,T)\|_{L^2(\Omega)}^2 &\le \|e(\cdot,0)\|_{L^2(\Omega)}^2 \\
&+ C \sum_{n=1}^N \sum_{K \in \mathcal{T}_h} \left\{ \int_{t^{n-1}}^{t^n} \left(\|f - \partial_n u_h + \Delta u_{h\tau}\|_{L^2(K)} + \frac{1}{2\lambda_{2,K}^{1/2}} \|[\nabla u_{h\tau} \cdot \mathbf{n}]\|_{L^2(\partial K)} \right) \right. \\
&\qquad \times \left(\lambda_{1,K}^2 \left(r_{1,K}^T G_K(\widehat{e}) r_{1,K} \right) + \lambda_{2,K}^2 \left(r_{2,K}^T G_K(\widehat{e}) r_{2,K} \right) \right)^{1/2} dt \\
&\qquad \left. + \int_{t^{n-1}}^{t^n} \left\| f - \widehat{f} \right\|_{L^2(K)}^2 dt + \frac{\tau_n^5}{120} \|\nabla w_h^n\|_{L^2(K)}^2 + \frac{\lambda_{2,K}^2 \tau_n^3}{12} \|w_h^n\|_{L^2(K)}^2 \right\}.
\end{aligned}$$

Here $[\cdot]$ denotes the jump of the bracketed quantity across an internal edge, $[\cdot] = 0$ for an edge on the boundary $\partial\Omega$, and $\mathbf{n}$ is the unit edge normal (in arbitrary direction).

Theorem 1.4.4. *Let*

$$\widetilde{f} = f^{n-1/2} + (t - t^{n-1/2}) \frac{f^n - f^{n-2}}{\tau_n + \tau_{n-1}}, \quad t \in I_n,\ 2 \le n \le N \tag{1.15}$$

and suppose that the mesh is such that there exists a constant c independent of the time step, mesh size and aspect ratio such that

$$\lambda_{1,K}^2 \left(r_{1,K}^T G_K(\widetilde{e}) r_{1,K} \right) \le c \lambda_{2,K}^2 \left(r_{2,K}^T G_K(\widetilde{e}) r_{2,K} \right) \quad \forall K \in \mathcal{T}_h. \tag{1.16}$$

Then there is a constant C independent of the time step, mesh size and aspect ratio such that

$$\int_{t^1}^{T} \|\nabla e\|^2_{L^2(\Omega)}\, dt + \|e(\cdot,T)\|^2_{L^2(\Omega)} \le \left\|e(\cdot,t^1)\right\|^2_{L^2(\Omega)}$$
$$+ C\sum_{n=2}^{N}\sum_{K\in\mathcal{T}_h}\left\{\int_{t^{n-1}}^{t^n}\left(\|f-\partial_n u_h+\Delta u_{h\tau}\|_{L^2(K)}+\frac{1}{2\lambda_{2,K}^{1/2}}\|[\nabla u_{h\tau}\cdot\mathbf{n}]\|_{L^2(\partial K)}\right)\right.$$
$$\left.\times\left(\lambda_{1,K}^2\left(r_{1,K}^T G_K(\widetilde{e})r_{1,K}\right)+\lambda_{2,K}^2\left(r_{2,K}^T G_K(\widetilde{e})r_{2,K}\right)\right)^{1/2} dt\right.$$
$$\left.+\int_{t^{n-1}}^{t^n}\left\|f-\widetilde{f}\right\|^2_{L^2(K)}dt+\left\{\frac{\tau_{n-1}^2\tau_n^3}{48}+\frac{\tau_n^5}{120}\right\}\|\nabla\partial_n^2 u_h\|^2_{L^2(K)}+\frac{\lambda_{2,K}^2\tau_n^3}{12}\|\partial_n^2 u_h\|^2_{L^2(K)}\right\}.$$

Remark 1.4.5. *The upper bounds in Theorems 1.4.3 and 1.4.4 are not traditional a posteriori error estimates since they involve $\omega_K(\widetilde{e})$ or $\omega_K(\widetilde{e})$ and hence the gradient of the exact solution u. A way to approximate it by a computable quantity was proposed in [30, 29] and is presented in Section 1.4.3. The resulting error estimator was proved very efficient for several problems, in particular the Poisson equation and the Euler discretization of the heat equation. We will also apply this technique in constructing our error estimators and the adaptive algorithm for the Crank-Nicolson scheme.*

Remark 1.4.6. *As we will see in Section 1.5, our anisotropic adaptive algorithm ensures assumptions (1.14) and (1.16) to be fulfilled with $c = 1$. A similar assumption has been made in [29] in order to prove a lower bound in the framework of the Laplace problem.*

Remark 1.4.7. *In the case of isotropic meshes $\lambda_{1,K} \simeq \lambda_{2,K} \simeq h_K$, the above a posteriori error estimates become*

$$\int_0^T \|\nabla e\|^2_{L^2(\Omega)}\ dt + \|e(\cdot,T)\|^2_{L^2(\Omega)} \le \|e(\cdot,0)\|^2_{L^2(\Omega)}$$
$$+ C\sum_{n=1}^{N}\sum_{K\in\mathcal{T}_h}\left\{\int_{t^{n-1}}^{t^n}\left(h_K^2\|f-\partial_n u_h+\Delta u_{h\tau}\|^2_{L^2(K)}+h_K\|[\nabla u_{h\tau}\cdot\mathbf{n}]\|^2_{L^2(\partial K)}\right)dt\right.$$
$$\left.+\int_{t^{n-1}}^{t^n}\left\|f-\widehat{f}\right\|^2_{L^2(K)}dt+\frac{\tau_n^5}{120}\|\nabla w_h^n\|^2_{L^2(K)}+\frac{h_K^2\tau_n^3}{12}\|w_h^n\|^2_{L^2(K)}\right\}$$

and

$$\int_{t^1}^{T} \|\nabla e\|^2_{L^2(\Omega)}\ dt + \|e(\cdot,T)\|^2_{L^2(\Omega)} \le \left\|e(\cdot,t^1)\right\|^2_{L^2(\Omega)}$$
$$+ C\sum_{n=2}^{N}\sum_{K\in\mathcal{T}_h}\left\{\int_{t^{n-1}}^{t^n}\left(h_K^2\left\|f-\partial_n u_h+\Delta u_{h\tau}\right\|^2_{L^2(K)} + h_K\left\|[\nabla u_{h\tau}\cdot\mathbf{n}]\right\|^2_{L^2(\partial K)}\right)dt\right.$$
$$\left.+\int_{t^{n-1}}^{t^n}\left\|f-\widetilde{f}\right\|^2_{L^2(K)}dt + \left\{\frac{\tau_{n-1}^2\tau_n^3}{48}+\frac{\tau_n^5}{120}\right\}\left\|\nabla\partial_n^2 u_h\right\|^2_{L^2(K)} + \frac{h_K^2\tau_n^3}{12}\left\|\partial_n^2 u_h\right\|^2_{L^2(K)}\right\},$$

without having to assume (1.14) *or* (1.16)*, but with a constant C depending on the mesh aspect ratio.*

Remark 1.4.8. *The last three terms in the error estimates of both Theorem 1.4.3 and 1.4.4 will be used to estimate the error due to the time discretization. When u is smooth enough, the error e in the $L^2(0,T;H^1(\Omega))$ norm is $O\left(h+\tau^2\right)$, thus the first of these three terms are of optimal order. The terms involving ∇w_n^h and $\nabla\partial_n^2 u_h$ are of optimal order provided $\sum_{n=1}^N \tau_n \left\|\nabla w_h^n\right\|^2_{L^2(\Omega)}$ and $\sum_{n=1}^N \tau_n \left\|\nabla\partial_n^2 u_h\right\|^2_{L^2(\Omega)}$ are bounded uniformly with respect to h and τ. The last terms are even of a higher order if we keep h proportional to τ^2 which is the natural choice in view of the error behavior $O\left(h+\tau^2\right)$.*

Proof of Theorem 1.4.3. We choose any $1\le n\le N$ and $t\in I_n$. We have from (1.11)

$$\frac{\partial\widehat{u}_{h\tau}}{\partial t} = \partial_n u_h + (t-t^{n-1/2})w_h^n.$$

Hence, for all $v\in H_0^1(\Omega)$

$$\int_\Omega \frac{\partial\widehat{e}}{\partial t}v\ dx + \int_\Omega \nabla e\cdot\nabla v\ dx = \int_\Omega (f-\partial_n u_h)\ v\ dx - \int_\Omega \nabla u_{h\tau}\cdot\nabla v\ dx$$
$$-(t-t^{n-1/2})\int_\Omega w_h^n\ v\ dx.$$

Then using (1.7) and (1.12), we obtain for all $v\in H_0^1(\Omega)$ and all $v_h\in V_h^0$

$$\int_\Omega \frac{\partial\widehat{e}}{\partial t}v\ dx + \int_\Omega \nabla e\cdot\nabla v\ dx$$
$$= \int_\Omega (f-\partial_n u_h)\ (v-v_h)\ dx - \int_\Omega \nabla u_{h\tau}\cdot\nabla(v-v_h)\ dx$$
$$-(t-t^{n-1/2})\int_\Omega w_h^n\ (v-v_h)\ dx + \int_\Omega (f-\widehat{f})\ v_h\ dx.$$

Taking $v = \widehat{e}$, $v_h = I_h\widehat{e}$ and integrating by parts on each triangle K leads to

$$\begin{aligned}
&\frac{1}{2}\frac{d}{dt}\int_\Omega |\widehat{e}|^2\,dx + \int_\Omega \nabla e\cdot\nabla\widehat{e}\,dx \\
&\quad = \sum_{K\in\mathcal{T}_h}\left\{\int_K (f-\partial_n u_h + \Delta u_{h\tau})\,(\widehat{e}-I_h\widehat{e})\,dx - \frac{1}{2}\int_{\partial K}[\nabla u_{h\tau}\cdot\mathbf{n}]\,(\widehat{e}-I_h\widehat{e})\,dx\right. \\
&\qquad \left. -(t-t^{n-1/2})\int_K w_h^n\,(\widehat{e}-I_h\widehat{e})\,dx + \int_K (f-\widehat{f})\,I_h\widehat{e}\,dx\right\}.
\end{aligned}$$

Using the fact that $ab = \frac{1}{2}a^2 + \frac{1}{2}b^2 - \frac{1}{2}(a-b)^2$, the Cauchy-Schwarz inequality, the first and third inequalities of Proposition 1.3.1 and the Poincaré inequality we have

$$\begin{aligned}
&\frac{1}{2}\frac{d}{dt}\int_\Omega |\widehat{e}|^2\,dx + \frac{1}{2}\int_\Omega |\nabla e|^2\,dx + \frac{1}{2}\int_\Omega |\nabla\widehat{e}|^2\,dx \\
&\le \sum_{K\in\mathcal{T}_h}\left\{C_1\left[\left(\|f-\partial_n u_h+\Delta u_{h\tau}\|_{L^2(K)} + \frac{1}{2\lambda_{2,K}^{1/2}}\,\|[\nabla u_{h\tau}\cdot\mathbf{n}]\|_{L^2(\partial K)}\right)\omega_K(\widehat{e})\right.\right. \\
&\qquad \left.\left. + |t-t^{n-1/2}|\,\|w_h^n\|_{L^2(K)}\,\omega_K(\widehat{e})\right] + C_2\left\|f-\widehat{f}\right\|_{L^2(K)}\|\nabla I_h\widehat{e}\|_{L^2(K)}\right. \\
&\qquad \left. + \frac{1}{2}\,\|\nabla(e-\widehat{e})\|_{L^2(K)}^2\right\},
\end{aligned}$$

where C_1 is the constant of Proposition 1.3.1 and C_2 is the constant in the Poincaré inequality. Considering that inequality (1.14) implies that

$$\omega_K(\widehat{e}) \le C_3\lambda_{2,K}\,\|\nabla\widehat{e}\|_{L^2(K)} \quad \forall K\in\mathcal{T}_h, \tag{1.17}$$

where C_3 is independent of the mesh size and aspect ratio and using the fact that

$ab \leq \frac{1}{2p}a^2 + \frac{p}{2}b^2$, for all $p \in \mathbb{R}^+$, we have

$$\begin{aligned}
&\frac{1}{2}\frac{d}{dt}\int_\Omega |\widehat{e}|^2\,dx + \frac{1}{2}\int_\Omega |\nabla e|^2\,dx + \frac{1}{2}\int_\Omega |\nabla\widehat{e}|^2\,dx \qquad (1.18)\\
&\leq \sum_{K\in\mathcal{T}_h}\left\{ C_1\left[\left(\|f-\partial_n u_h + \Delta u_{h\tau}\|_{L^2(K)} + \frac{1}{2\lambda_{2,K}^{1/2}}\|[\nabla u_{h\tau}\cdot\mathbf{n}]\|_{L^2(\partial K)}\right)\omega_K(\widehat{e})\right.\right.\\
&\quad \left.\left. + \frac{p}{2}(t-t^{n-1/2})^2\lambda_{2,K}^2\|w_h^n\|_{L^2(K)}^2\right] + \frac{C_1C_3^2}{2p}\|\nabla\widehat{e}\|_{L^2(K)}^2 + \frac{p}{2}\left\|f-\widehat{f}\right\|_{L^2(K)}^2\right.\\
&\quad \left. + \frac{C_2^2}{2p}\|\nabla I_h\widehat{e}\|_{L^2(K)}^2 + \frac{1}{2}\|\nabla(e-\widehat{e})\|_{L^2(K)}^2\right\}.
\end{aligned}$$

We want now to have an upper bound for $\|\nabla I_h\widehat{e}\|_{L^2(K)}^2$. Thus, using (1.17) in the second inequality of Proposition 1.3.1, we have

$$\|\nabla(\widehat{e}-I_h\widehat{e})\|_{L^2(K)} \leq C_4\|\nabla\widehat{e}\|_{L^2(K)} \quad \forall K\in\mathcal{T}_h,$$

with $C_4 = C_1C_3$. Thus

$$\|\nabla I_h\widehat{e}\|_{L^2(K)} \leq \|\nabla(\widehat{e}-I_h\widehat{e})\|_{L^2(K)} + \|\nabla\widehat{e}\|_{L^2(K)} \leq (1+C_4)\|\nabla\widehat{e}\|_{L^2(K)}. \qquad (1.19)$$

Finally, use (1.19) in (1.18), choose $p = C_1C_3^2 + (1+C_4)^2C_2^2$, recall that from (1.11) we have

$$e-\widehat{e} = \widehat{u}_{h\tau} - u_{h\tau} = \frac{1}{2}(t-t^{n-1})(t-t^n)w_h^n$$

and integrate (1.18) between $t=t^{n-1}$ and $t=t^n$, we obtain

$$\begin{aligned}
&\int_{t^{n-1}}^{t^n}\|\nabla e\|_{L^2(\Omega)}^2\,dt + \|\widehat{e}(\cdot,t^n)\|_{L^2(\Omega)}^2 \leq \left\|\widehat{e}(\cdot,t^{n-1})\right\|_{L^2(\Omega)}^2\\
&+ C\sum_{K\in\mathcal{T}_h}\left\{\int_{t^{n-1}}^{t^n}\left(\|f-\partial_n u_h+\Delta u_{h\tau}\|_{L^2(K)} + \frac{1}{2\lambda_{2,K}^{1/2}}\|[\nabla u_{h\tau}\cdot\mathbf{n}]\|_{L^2(\partial K)}\right)\omega_K(\widehat{e})\,dt\right.\\
&\left. + \int_{t^{n-1}}^{t^n}\left\|f-\widehat{f}\right\|_{L^2(K)}^2\,dt + \frac{\tau_n^5}{120}\|\nabla w_h^n\|_{L^2(K)}^2 + \frac{\lambda_{2,K}^2\tau_n^3}{12}\|w_h^n\|_{L^2(K)}^2\right\},
\end{aligned}$$

where $C = \max(1, 2C_1, pC_1, p)$. Summing up these inequalities on $n = 1,\ldots,N$ and noting that $\widehat{e}(t^n) = e(t^n)\ \forall n$, leads to the final result. □

We will now prove Theorem 1.4.4. In order to derive an a posteriori error estimate involving $\widetilde{u}_{h\tau}$, we first need the following result.

Proposition 1.4.9. *Let $\widetilde{u}_{h\tau}$ be defined by (1.13) and $\widetilde{f}$ by (1.15), then for all $v_h \in V_h^0$ and for any $t \in I_n$, $2 \le n \le N$, we have*

$$\int_\Omega \frac{\partial \widetilde{u}_{h\tau}}{\partial t} v_h \, dx + \int_\Omega \nabla u_{h\tau} \cdot \nabla v_h \, dx = \int_\Omega \widetilde{f} v_h \, dx + (t - t^{n-1/2}) \frac{\tau_{n-1}}{2} \int_\Omega \nabla \partial_n^2 u_h \cdot \nabla v_h \, dx.$$

Proof. We choose any $2 \le n \le N$ and $t \in I_n$ in this proof. We have from (1.13) that

$$\frac{\partial \widetilde{u}_{h\tau}}{\partial t} = \partial_n u_h + (t - t^{n-1/2}) \partial_n^2 u_h. \tag{1.20}$$

Then, using (1.7), we have for all $v_h \in V_h^0$

$$\int_\Omega \frac{\partial \widetilde{u}_{h\tau}}{\partial t} v_h \, dx + \int_\Omega \nabla u_{h\tau} \cdot \nabla v_h \, dx = \int_\Omega f^{n-1/2} \, v_h \, dx + (t - t^{n-1/2}) \int_\Omega \left\{ \partial_n^2 u_h \, v_h + \nabla \partial_n u_h \cdot \nabla v_h \right\} dx. \tag{1.21}$$

We invoke now (1.3) at the time t^{n-1},

$$\int_\Omega \frac{u_h^{n-1} - u_h^{n-2}}{\tau_{n-1}} \, v_h \, dx + \int_\Omega \frac{\nabla (u_h^{n-1} + u_h^{n-2})}{2} \cdot \nabla v_h \, dx = \int_\Omega \frac{f^{n-1} + f^{n-2}}{2} \, v_h \, dx$$

and subtract it from (1.3) to obtain for all $v_h \in V_h^0$

$$\int_\Omega \left\{ \partial_n^2 u_h \, v_h + \nabla \left(\frac{u_h^n - u_h^{n-2}}{\tau_n + \tau_{n-1}} \right) \cdot \nabla v_h \right\} dx = \frac{1}{\tau_n + \tau_{n-1}} \int_\Omega (f^n - f^{n-2}) v_h \, dx.$$

Thus

$$\int_\Omega \left\{ \partial_n^2 u_h \, v_h + \nabla \partial_n u_h \cdot \nabla v_h \right\} dx = \frac{1}{\tau_n + \tau_{n-1}} \int_\Omega (f^n - f^{n-2}) v_h \, dx + \frac{\tau_{n-1}}{2} \int_\Omega \nabla \partial_n^2 u_h \cdot \nabla v_h \, dx. \tag{1.22}$$

It suffices now to insert (1.22) in (1.21) to obtain the result. □

Proof of Theorem 1.4.4. We choose any $2 \leq n \leq N$ and $t \in I_n$. Using (1.7), (1.20) and Proposition 1.4.9, we obtain for all $v \in H_0^1(\Omega)$ and all $v_h \in V_h^0$

$$
\begin{aligned}
&\int_\Omega \frac{\partial \widetilde{e}}{\partial t} v \, dx + \int_\Omega \nabla e \cdot \nabla v \, dx \\
&= \int_\Omega (f - \partial_n u_h)\, v \, dx - \int_\Omega \nabla u_{h\tau} \cdot \nabla v \, dx - (t - t^{n-1/2}) \int_\Omega \partial_n^2 u_h \, v \, dx \\
&= \int_\Omega (f - \partial_n u_h)\, (v - v_h) \, dx - \int_\Omega \nabla u_{h\tau} \cdot \nabla (v - v_h) \, dx \\
&\quad + \int_\Omega \left(f - \frac{\partial \widetilde{u}_{h\tau}}{\partial t} \right) v_h \, dx - \int_\Omega \nabla u_{h\tau} \cdot \nabla v_h \, dx - (t - t^{n-1/2}) \int_\Omega \partial_n^2 u_h (v - v_h) dx \\
&= \int_\Omega (f - \partial_n u_h)\, (v - v_h) \, dx - \int_\Omega \nabla u_{h\tau} \cdot \nabla (v - v_h) \, dx \\
&\quad - (t - t^{n-1/2}) \frac{\tau_{n-1}}{2} \int_\Omega \nabla \partial_n^2 u_h \cdot \nabla v_h \, dx + \int_\Omega (f - \widetilde{f}) \, v_h \, dx \\
&\quad - (t - t^{n-1/2}) \int_\Omega \partial_n^2 u_h \, (v - v_h) \, dx.
\end{aligned}
$$

Then taking $v = \widetilde{e}$ and $v_h = I_h \widetilde{e}$ and integrating by parts on each triangle K, we obtain

$$
\begin{aligned}
&\frac{1}{2} \frac{d}{dt} \int_\Omega |\widetilde{e}|^2 \, dx + \int_\Omega \nabla e \cdot \nabla \widetilde{e} \, dx = \\
&\quad \sum_{K \in \mathcal{T}_h} \Bigg\{ \int_K (f - \partial_n u_h + \Delta u_{h\tau}) \, (\widetilde{e} - I_h \widetilde{e}) \, dx - \frac{1}{2} \int_{\partial K} [\nabla u_{h\tau} \cdot \mathbf{n}] \, (\widetilde{e} - I_h \widetilde{e}) \, dx \\
&\quad - (t - t^{n-1/2}) \frac{\tau_{n-1}}{2} \int_K \nabla \partial_n^2 u_h \cdot \nabla I_h \widetilde{e} \, dx + \int_K (f - \widetilde{f}) \, I_h \widetilde{e} \, dx \\
&\quad - (t - t^{n-1/2}) \int_K \partial_n^2 u_h \, (\widetilde{e} - I_h \widetilde{e}) \, dx \Bigg\}.
\end{aligned}
$$

Using the fact that $ab = \frac{1}{2}a^2 + \frac{1}{2}b^2 - \frac{1}{2}(a-b)^2$, the Cauchy-Schwarz inequality, Proposition 1.3.1, the Poincaré inequality, the inequality $ab \leq \frac{1}{2p}a^2 + \frac{p}{2}b^2$, for all $p \in \mathbb{R}^+$ and the relation

$$
\|\nabla(e - \widetilde{e})\|^2_{L^2(\Omega)} = \|\nabla(\widetilde{u}_{h\tau} - u_{h\tau})\|^2_{L^2(\Omega)} = \frac{1}{4}(t - t^{n-1})^2 (t - t^n)^2 \|\nabla \partial_n^2 u_h\|^2_{L^2(\Omega)},
$$

we have

$$\begin{aligned}
&\frac{1}{2}\frac{d}{dt}\int_\Omega |\widetilde{e}|^2\,dx + \frac{1}{2}\int_\Omega |\nabla e|^2\,dx + \frac{1}{2}\int_\Omega |\nabla\widetilde{e}|^2\,dx \\
&\le \sum_{K\in\mathcal{T}_h}\left\{ C_1\left[\left(\|f-\partial_n u_h + \Delta u_{h\tau}\|_{L^2(K)} + \frac{1}{2\lambda_{2,K}^{1/2}}\,\|[\nabla u_{h\tau}\cdot\mathbf{n}]\|_{L^2(\partial K)}\right)\omega_K(\widetilde{e})\right.\right. \\
&\qquad \left.\left. + |t-t^{n-1/2}|\,\left\|\partial_n^2 u_h\right\|_{L^2(K)}\,\omega_K(\widetilde{e})\right]\right. \\
&\qquad + \left\{\frac{p}{8}(\tau_{n-1})^2(t-t^{n-1/2})^2 + \frac{1}{8}(t-t^{n-1})^2(t-t^n)^2\right\}\left\|\nabla\partial_n^2 u_h\right\|^2_{L^2(K)} \\
&\qquad \left. + \frac{p}{2}\left\|f-\widetilde{f}\right\|^2_{L^2(K)} + \frac{1+C_2^2}{2p}\,\|\nabla I_h\widetilde{e}\|^2_{L^2(K)}\right\},
\end{aligned}$$

where C_1 is the constant of Proposition 1.3.1 and C_2 is the constant in the Poincaré inequality. Error equidistribution inequality (1.16) combined with Proposition 1.3.1 implies that

$$\omega_K(\widetilde{e}) \le C_3\lambda_{2,K}\,\|\nabla\widetilde{e}\|_{L^2(K)} \quad\text{and}\quad \|\nabla I_h\widetilde{e}\|_{L^2(K)} \le C_4\,\|\nabla\widetilde{e}\|_{L^2(K)}\,. \tag{1.23}$$

We have then

$$\begin{aligned}
&\frac{1}{2}\frac{d}{dt}\int_\Omega |\widetilde{e}|^2\,dx + \frac{1}{2}\int_\Omega |\nabla e|^2\,dx + \frac{1}{2}\int_\Omega |\nabla\widetilde{e}|^2\,dx \qquad (1.24)\\
&\le \sum_{K\in\mathcal{T}_h}\left\{ C_1\left[\left(\|f-\partial_n u_h + \Delta u_{h\tau}\|_{L^2(K)} + \frac{1}{2\lambda_{2,K}^{1/2}}\,\|[\nabla u_{h\tau}\cdot\mathbf{n}]\|_{L^2(\partial K)}\right)\omega_K(\widetilde{e})\right.\right. \\
&\qquad \left.\left. + \frac{p}{2}\lambda_{2,K}^2(t-t^{n-1/2})^2\,\left\|\partial_n^2 u_h\right\|^2_{L^2(K)}\right] + \frac{C_1C_3^2}{2p}\,\|\nabla\widetilde{e}\|^2_{L^2(K)}\right. \\
&\qquad + \left\{\frac{p}{8}\tau_{n-1}^2(t-t^{n-1/2})^2 + \frac{1}{8}(t-t^{n-1})^2(t-t^n)^2\right\}\left\|\nabla\partial_n^2 u_h\right\|^2_{L^2(K)} \\
&\qquad \left. + \frac{p}{2}\left\|f-\widetilde{f}\right\|^2_{L^2(K)} + \frac{1+C_2^2}{2p}\,\|\nabla I_h\widetilde{e}\|^2_{L^2(K)}\right\}.
\end{aligned}$$

Finally, use the second inequality of (1.23) in (1.24), choose $p = C_1C_3^2 + C_4^2(1+C_2^2)$, and integrate (1.24) between $t = t^{n-1}$ and $t = t^n$, to obtain

$$\int_{t^{n-1}}^{t^n} \|\nabla e\|^2_{L^2(\Omega)}\ dt + \|\widetilde{e}(\cdot,t^n)\|^2_{L^2(\Omega)} \leq \left\|\widetilde{e}(\cdot,t^{n-1})\right\|^2_{L^2(\Omega)}$$
$$+ C \sum_{K\in\mathcal{T}_h} \left\{ \int_{t^{n-1}}^{t^n} \left(\|f - \partial_n u_h + \Delta u_{h\tau}\|_{L^2(K)} + \frac{1}{2\lambda_{2,K}^{1/2}} \|[\nabla u_{h\tau}\cdot\mathbf{n}]\|_{L^2(\partial K)} \right) \right.$$
$$\left. \times \left(\lambda_{1,K}^2 \left(r_{1,K}^T G_K(\widetilde{e}) r_{1,K}\right) + \lambda_{2,K}^2 \left(r_{2,K}^T G_K(\widetilde{e}) r_{2,K}\right) \right)^{1/2} dt \right.$$
$$\left. + \int_{t^{n-1}}^{t^n} \left\|f - \widetilde{f}\right\|^2_{L^2(K)} dt + \left\{ \frac{\tau_{n-1}^2 \tau_n^3}{48} + \frac{\tau_n^5}{120} \right\} \left\|\nabla \partial_n^2 u_h\right\|^2_{L^2(K)} + \frac{\lambda_{2,K}^2 \tau_n^3}{12} \left\|\partial_n^2 u_h\right\|^2_{L^2(K)} \right\},$$

where $C = \max(1, 2C_1, pC_1, p)$. Summing up this inequality on n and noting that $\widetilde{e}(t^n) = e(t^n)\ \forall n$, leads to the final result. □

1.4.3 A posteriori error indicators

As already noted in the previous Section, the upper bounds for the error derived in Theorems 1.4.3 and 1.4.4 are not traditional a posteriori error estimates since they involve $\omega_K(\widehat{e})$ and $\omega_K(\widetilde{e})$ and hence u. Therefore, following [30, 29], we introduce the Zienkiewicz-Zhu error estimator [52, 53], namely, the difference between $\nabla u_{h\tau}$ and an approximate $L^2(\Omega)$ projection onto V_h:

$$\eta^{ZZ}(u_{h\tau}) = \begin{pmatrix} \eta_1^{ZZ}(u_{h\tau}) \\ \eta_2^{ZZ}(u_{h\tau}) \end{pmatrix} = \begin{pmatrix} (I - \Pi_h)\left(\dfrac{\partial u_{h\tau}}{\partial x_1}\right) \\ (I - \Pi_h)\left(\dfrac{\partial u_{h\tau}}{\partial x_2}\right) \end{pmatrix}, \tag{1.25}$$

where $\Pi_h(\nabla u_{h\tau}) \in V_h$ is defined by its values at each vertex P as

$$\Pi_h(\nabla u_{h\tau})(P) = \begin{pmatrix} \Pi_h\left(\dfrac{\partial u_{h\tau}}{\partial x_1}\right)(P) \\ \Pi_h\left(\dfrac{\partial u_{h\tau}}{\partial x_2}\right)(P) \end{pmatrix} = \frac{1}{\displaystyle\sum_{\substack{K\in\mathcal{T}_h \\ P\in K}} |K|} \begin{pmatrix} \displaystyle\sum_{\substack{K\in\mathcal{T}_h \\ P\in K}} |K| \left(\dfrac{\partial u_{h\tau}}{\partial x_1}\right)_{|K} \\ \displaystyle\sum_{\substack{K\in\mathcal{T}_h \\ P\in K}} |K| \left(\dfrac{\partial u_{h\tau}}{\partial x_2}\right)_{|K} \end{pmatrix}. \tag{1.26}$$

Our error indicator is then obtained by replacing $G_K(\widehat{e})$ in $\omega_K(\widehat{e})$ and $G_K(\widetilde{e})$ in $\omega_K(\widetilde{e})$ by $\breve{G}_K(u_{h\tau})$ defined for any $v_h \in V_h$ by

$$\breve{G}_K(v_h) = \begin{pmatrix} \displaystyle\int_K \left(\eta_1^{ZZ}(v_h)\right)^2\ dx & \displaystyle\int_K \eta_1^{ZZ}(v_h)\eta_2^{ZZ}(v_h)\ dx \\ \displaystyle\int_K \eta_1^{ZZ}(v_h)\eta_2^{ZZ}(v_h)\ dx & \displaystyle\int_K \left(\eta_2^{ZZ}(v_h)\right)^2\ dx \end{pmatrix}. \tag{1.27}$$

Approximating in such a way $G_K(\widehat{e})$ in Theorem 1.4.3 and $G_K(\widetilde{e})$ in Theorem 1.4.4, we define the anisotropic space error estimator η^A as

$$\eta^A = \left(\sum_{n=1}^{N} \sum_{K \in \mathcal{T}_h} \left(\eta_{K,n}^A(u_{h\tau}) \right)^2 \right)^{1/2}$$

where the contributions $\eta_{K,n}^A$ are defined on each triangle K of $\mathcal{T}_h$ and each time interval I_n as

$$\left(\eta_{K,n}^A(u_{h\tau}) \right)^2 = \int_{t^{n-1}}^{t^n} \left(\|f - \partial_n u_h + \Delta u_{h\tau}\|_{L^2(K)} + \frac{1}{2\lambda_{2,K}^{1/2}} \|[\nabla u_{h\tau} \cdot \mathbf{n}]\|_{L^2(\partial K)} \right)$$
$$\times \left(\lambda_{1,K}^2 \left(r_{1,K}^T \breve{G}_K(u_{h\tau}) r_{1,K} \right) + \lambda_{2,K}^2 \left(r_{2,K}^T \breve{G}_K(u_{h\tau}) r_{2,K} \right) \right)^{1/2} dt. \tag{1.28}$$

We introduce now two time error estimators: $\widehat{\eta}^T$ corresponding to the two-point reconstruction $\widehat{u}_{h\tau}$ (cf Theorem 1.4.3) and $\widetilde{\eta}^T$ corresponding to the three-point reconstruction $\widetilde{u}_{h\tau}$ (cf Theorem 1.4.4) defined respectively by

$$\widehat{\eta}^T = \left(\sum_{n=1}^{N} \sum_{K \in \mathcal{T}_h} \left(\widehat{\eta}_{K,n}^T(u_{h\tau}) \right)^2 \right)^{1/2} \text{ and } \widetilde{\eta}^T = \left(\sum_{n=2}^{N} \sum_{K \in \mathcal{T}_h} \left(\widetilde{\eta}_{K,n}^T(u_{h\tau}) \right)^2 \right)^{1/2}.$$

The contributions $\widehat{\eta}_{K,n}^T$ and $\widetilde{\eta}_{K,n}^T$ are computed on each triangle K of $\mathcal{T}_h$ and each time interval I_n via, for $n \geq 1$,

$$\left(\widehat{\eta}_{K,n}^T(u_{h\tau}) \right)^2 = \int_{t^{n-1}}^{t^n} \left\| f - \widehat{f} \right\|_{L^2(K)}^2 dt + \frac{\tau_n^5}{120} \|\nabla w_h^n\|_{L^2(K)}^2 + \frac{\lambda_{2,K}^2 \tau_n^3}{12} \|w_h^n\|_{L^2(K)}^2, \tag{1.29}$$

and for $n \geq 2$,

$$\left(\widetilde{\eta}_{K,n}^T(u_{h\tau}) \right)^2 = \int_{t^{n-1}}^{t^n} \left\| f - \widetilde{f} \right\|_{L^2(K)}^2 dt + \left\{ \frac{\tau_{n-1}^2 \tau_n^3}{48} + \frac{\tau_n^5}{120} \right\} \left\| \nabla \partial_n^2 u_h \right\|_{L^2(K)}^2$$
$$+ \frac{\lambda_{2,K}^2 \tau_n^3}{12} \left\| \partial_n^2 u_h \right\|_{L^2(K)}^2. \tag{1.30}$$

In our implementation, all the integral between t^{n-1} and t^n are approximated by the midpoint rule. Moreover, we introduce the time error estimator η^T defined by

$$\eta^T = \left(\sum_{n=1}^{N} \sum_{K \in \mathcal{T}_h} \left(\eta_{K,n}^T(u_{h\tau}) \right)^2 \right)^{1/2}, \tag{1.31}$$

where the contributions $\eta_{K,n}^T$ are defined on each triangle K of $\mathcal{T}_h$ and each time interval I_n as

$$\left(\eta_{K,n}^T(u_{h\tau})\right)^2 = \tau_n \left\|\nabla\left(u_h^n - u_h^{n-1}\right)\right\|_{L^2(K)}^2.$$

This time error estimator corresponds to the time error indicator derived in [46] for the heat equation discretized in time using the Crank-Nicolson method. This time error estimator is similar to that obtained in Section 2.3 of [30] for the Euler implicit time discretization of the heat equation and is of suboptimal order with respect to time when considering the Crank-Nicolson scheme.

In order to measure the quality of our estimators, the estimated error is compared to the true error introducing the so-called effectivity index, ei. Thus, we define the following effectivity indices in space

$$ei^A = \frac{\eta^A}{\left(\int_0^T \int_\Omega |\nabla e|^2 \, dx \, dt\right)^{1/2}} \tag{1.32}$$

and in time

$$\widehat{ei}^T = \frac{\widehat{\eta}^T}{\left(\int_0^T \int_\Omega |\nabla e|^2 \, dx \, dt\right)^{1/2}}, \; ei^T = \frac{\eta^T}{\left(\int_0^T \int_\Omega |\nabla e|^2 \, dx \, dt\right)^{1/2}},$$

and

$$\widetilde{ei}^T = \frac{\widetilde{\eta}^T}{\left(\int_{t^1}^T \int_\Omega |\nabla e|^2 \, dx \, dt\right)^{1/2}}. \tag{1.33}$$

We will also check the behavior of the Zienkiewicz-Zhu error estimator. We thus introduce the corresponding global estimator and the effectivity index

$$\eta^{ZZ} = \left(\sum_{n=1}^N \sum_{K \in \mathcal{T}_h} \int_{t^{n-1}}^{t^n} \int_K |\eta^{ZZ}(u_{h\tau})|^2 \, dx \, dt\right)^{1/2} \tag{1.34}$$

and

$$ei^{ZZ} = \frac{\eta^{ZZ}}{\left(\int_0^T \int_\Omega |\nabla e|^2 \, dx \, dt\right)^{1/2}}. \tag{1.35}$$

The error estimator is said to be equivalent to the true error when there exists two constants C_1 and C_2 independent of the mesh such that

$$C_1 \leq ei \leq C_2,$$

and the error estimator is said to be asymptotically exact if

$$ei \underset{h\to 0}{\longrightarrow} 1.$$

Remark 1.4.10. *An alternative gradient recovery based on least square fitting has been proposed in [54, 55]. Here we do not attempt to use this method since the Zienkiewicz-Zhu error estimator performs surprisingly well.*

1.4.4 A numerical study of the error estimators with uniform time steps and mesh size

We study here the effectivity indices corresponding to the two error estimators $\widehat{\eta}^T$ and $\widetilde{\eta}^T$ on several test cases for which the error comes either from the space discretization, or from the time discretization, or from both of them. Set $\Omega = (0,1)\times(0,1)$ the unit square, $T = 1$ and choose u^0 and f so that the solution u of (1.1) is given by

$$\begin{aligned}
&\text{case (a)} \qquad u(x,y,t) = sin(15\pi t)\ sin(\pi x)\ sin(\pi y),\\
&\text{case (b)} \qquad u(x,y,t) = sin(\pi t/2)\ sin(10\pi x)\ sin(10\pi y),\\
&\text{case (c)} \qquad u(x,y,t) = sin(\pi t)\ sin(\pi x)\ sin(\pi y).
\end{aligned}$$

Note that in case (a) the error should be mainly due to the time discretization, while in case (b) it should be mainly due to space discretization. Case (c) provides an example in which the error comes from both space and time discretization. The numerical results are reported in Tables 1.1–1.3. Uniform isotropic meshes and constant time steps are used in all the experiments of this Subsection.

Referring to Table 1.1, we observe that the computed error in the test case (a) is mainly due to the time discretization. Indeed, for a given time step, the error does not depend on the space step h, and for constant h, the error is divided by four when the time step τ is divided by two. Moreover the two time error estimators $\widetilde{\eta}^T$ and $\widehat{\eta}^T$ behave as the true error. Referring to Table 1.2, case (b), the error is now mainly due to space discretization. We observe that for constant h, the error does not depend on the time step τ, that the space effectivity index stays close to 2.5 and that the Zienkiewicz-Zhu error estimator is asymptotically exact. Thus, when the error is mainly due to the space discretization we can see that the space error estimator η^A behaves as the true error. Referring to Table 1.3, case (c), the error comes now from both space and time discretizations. We observe that the error in the $L^2(0,T;H^1(\Omega))$ norm is $O\left(h+\tau^2\right)$, that the space error estimator and the two time error estimators, $\widehat{\eta}^T$ and $\widetilde{\eta}^T$, are equivalent to the true error and that the Zienkiewicz-Zhu error estimator is asymptotically exact. Thus, using

h	τ	$\left(\int_0^T \int_\Omega \lvert\nabla e\rvert^2\right)^{1/2}$	ei^{ZZ}	ei^A	$\widetilde{ei}^T$	$\widehat{ei}^T$
0.0125	0.025	0.17	0.10	0.25	17.23	14.05
0.00625	0.025	0.17	0.05	0.125	17.35	14.15
0.003125	0.025	0.17	0.024	0.06	17.39	14.17
0.0125	0.0125	0.047	0.44	1.09	16.25	13.22
0.00625	0.0125	0.043	0.24	0.60	17.85	14.53
0.003125	0.0125	0.042	0.12	0.30	18.42	14.92

Table 1.1. *Convergence results using uniform isotropic meshes and constant time steps, case (a).*

h	τ	$\left(\int_0^T \int_\Omega \lvert\nabla e\rvert^2\right)^{1/2}$	ei^{ZZ}	ei^A	$\widetilde{ei}^T$	$\widehat{ei}^T$
0.00625	0.05	1.11	1.01	2.47	0.48	0.61
0.00625	0.025	1.11	1.01	2.47	0.12	0.16
0.00625	0.0125	1.11	1.01	2.47	0.03	0.04
0.003125	0.05	0.56	1.00	2.46	0.96	1.21
0.003125	0.025	0.56	1.00	2.46	0.24	0.31
0.003125	0.0125	0.56	1.00	2.46	0.06	0.078

Table 1.2. *Convergence results using uniform isotropic meshes and constant time steps, case (b).*

h	τ	$\left(\int_0^T \int_\Omega \lvert\nabla e\rvert^2\right)^{1/2}$	ei^{ZZ}	ei^A	$\widetilde{ei}^T$	$\widehat{ei}^T$	ei^T
0.025	0.05	0.044	1.00	2.46	0.52	0.42	5.29
0.00625	0.025	0.011	1.00	2.45	0.51	0.43	10.75
0.0015625	0.0125	0.0028	1.00	2.45	0.51	0.49	21.73
0.025	0.0125	0.044	1.00	2.46	0.032	0.027	1.38
0.00625	0.00625	0.011	1.00	2.45	0.032	0.034	2.74
0.0015625	0.003125	0.0028	1.00	2.45	0.032	0.067	5.48

Table 1.3. *Convergence results using uniform isotropic meshes and constant time steps, case (c).*

uniform time steps and mesh size we observe that the two time error estimators, $\widehat{\eta}^T$ and $\widetilde{\eta}^T$, provide a good representation of the true error. In Table 1.3, we have also reported the effectivity index ei^T corresponding to the time estimator (1.31)

derived in [46]. We observe that its effectivity index is multiplied by two each time the space step and the time step are respectively divided by four and two. In Table 1.4, case (c), we report the effectivity index ei^T when dividing the space step and the time step by two. We observe that ei^T is constant. The time error estimator η^T then behaves as $O(h+\tau)$ and is consequently of suboptimal order with respect to time when considering the Crank-Nicolson time discretization.

h	τ	$\left(\int_0^T \int_\Omega \lvert\nabla e\rvert^2\right)^{1/2}$	ei^{ZZ}	ei^A	ei^T
0.025	0.05	0.044	1.00	2.46	5.29
0.0125	0.025	0.022	1.00	2.45	5.37
0.00625	0.0125	0.011	1.00	2.45	5.45
0.003125	0.00625	0.0056	1.00	2.45	5.47

Table 1.4. *Convergence results for η^T using uniform isotropic meshes and constant time steps, case (c).*

1.5 Adaptive algorithm in space and time

We now propose an adaptive algorithm in space and time. We will describe this algorithm while using (1.28) and (1.30). Since the time error estimator needs a solution u_h^{n-2}, we do not change the first time step. For $n \geq 2$, the idea is to build successive triangulations $\mathcal{T}_h^n$ with possibly large aspect ratio and to choose appropriate time steps τ_n so that the relative estimated error in space and time in the $L^2(0,T;H^1(\Omega))$ norm is close to a preset tolerance TOL, for example

$$0.875 \text{ TOL } \leq \frac{\left((\eta^A)^2 + (\widetilde{\eta}^T)^2\right)^{1/2}}{\left(\displaystyle\int_0^T \int_\Omega |\nabla u_{h\tau}|^2 \, dx \, dt\right)^{1/2}} \leq 1.125 \text{ TOL}. \tag{1.36}$$

In doing so, we are beyond the scope of the theory developed in the previous Section since the mesh $\mathcal{T}_h$ was not allowed to vary in time there. A more rigorous adaptive procedure would have to include the error due to the interpolations from $\mathcal{T}_h^{n-1}$ to $\mathcal{T}_h^n$. We do not attempt to develop such a theory here and conjecture that the interpolation error can be neglected provided the total number of remeshings does not depend on the prescribed tolerance TOL. This point will be observed numerically in Section 1.6.

In order to satisfy (1.36) we require that, for all $n \geq 1$, the error indicator in space is such that

$$\frac{1}{2}\ 0.875^2\ \mathrm{TOL}^2 \int_{t^{n-1}}^{t^n} \int_\Omega |\nabla u_{h\tau}|^2\ dx\ dt\ \leq \sum_{K\in\mathcal{T}_h} \left(\eta^A_{K,n}(u_{h\tau})\right)^2 \leq \frac{1}{2}\ 1.125^2\ \mathrm{TOL}^2 \int_{t^{n-1}}^{t^n} \int_\Omega |\nabla u_{h\tau}|^2\ dx\ dt, \tag{1.37}$$

and for all $n \geq 2$, the error indicator in time is such that

$$\frac{1}{2}\ 0.875^2\ \mathrm{TOL}^2 \int_{t^{n-1}}^{t^n} \int_\Omega |\nabla u_{h\tau}|^2\ dx\ dt\ \leq \sum_{K\in\mathcal{T}_h} \left(\widetilde{\eta}^T_{K,n}(u_{h\tau})\right)^2 \leq \frac{1}{2}\ 1.125^2\ \mathrm{TOL}^2 \int_{t^{n-1}}^{t^n} \int_\Omega |\nabla u_{h\tau}|^2\ dx\ dt. \tag{1.38}$$

Note that we do not take into account the error in time corresponding to the first time step. If (1.37) is not satisfied, the BL2D anisotropic mesh generator [49] is invoked to construct another mesh based on the space error indicator η^A. The P_1-interpolation between the previous mesh $\mathcal{T}_h^{n-1}$ and the new mesh $\mathcal{T}_h^n$ is carried out by the BL2D mesh generator. Thus, BL2D provides us an interpolated solution $r_h^n(u_h^{n-1})$ of u_h^{n-1} on the new mesh, where r_h^n is the Lagrange interpolant operator on $\mathcal{T}_h^n$. Then, after each remeshing, we seek $u_h^n \in V_{h,n}^0$ such that $\forall v_h \in V_{h,n}^0$

$$\int_\Omega \frac{u_h^n - r_h^n(u_h^{n-1})}{\tau_n} v_h\ dx + \frac{1}{2}\int_\Omega \left(\nabla u_h^n + \nabla r_h^n(u_h^{n-1})\right)\cdot \nabla v_h\ dx = \frac{1}{2}\int_\Omega (f^n + f^{n-1}) v_h\ dx. \tag{1.39}$$

Since BL2D requires the data to be given at the mesh vertices rather than triangles, the condition (1.37) has to be translated to a condition for the mesh vertices. For this purpose, we introduce at each vertex P the anisotropic error estimator defined by

$$\eta^A_{P,n}\big(u_{h\tau}\big) = \left(\sum_{\substack{K\in\mathcal{T}_h \\ P\in K}} \left(\eta^A_{K,n}(u_{h\tau})\right)^4\right)^{1/4}.$$

Since

$$\sum_{P\in\mathcal{T}_h}\left(\eta^A_{P,n}(u_{h\tau})\right)^4 = 3\sum_{K\in\mathcal{T}_h}\left(\eta^A_{K,n}(u_{h\tau})\right)^4,$$

then (1.37) holds whenever the following condition for every vertex P is satisfied

$$\frac{\sqrt{3}}{2N_V}\,0.875^2\ \mathrm{TOL}^2\int_{t^{n-1}}^{t^n}\int_\Omega |\nabla u_{h\tau}|^2\,dx\,dt\ \le \tag{1.40}$$
$$\left(\eta^A_{P,n}(u_{h\tau})\right)^2$$
$$\le \frac{\sqrt{3}}{2N_V}\,1.125^2\ \mathrm{TOL}^2\int_{t^{n-1}}^{t^n}\int_\Omega |\nabla u_{h\tau}|^2\,dx\,dt,$$

where N_V is the number of vertices of the mesh at time t^n. The mesh generator BL2D requires the metric to be given at each vertex P, namely, the direction of anisotropy θ_P and the two stretching amplitudes $h_{1,P}$ and $h_{2,P}$, see Figure 1.4.

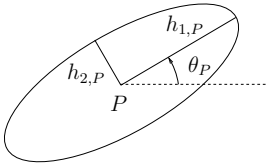

Figure 1.4. *The input values of the BL2D mesh generator at vertex P.*

The space adaptive algorithm is then as follows. First, we introduce at each vertex P the two anisotropic error estimators in the direction of maximum and minimum stretching defined by

$$\eta^A_{i,P,n}\big(u_{h\tau}\big) = \left(\sum_{\substack{K\in\mathcal{T}_h\\ P\in K}}\left(\eta^A_{i,K,n}(u_{h\tau})\right)^4\right)^{1/4},$$

where $\eta^A_{i,K,n}$ is the local error estimator on triangle K in the direction $r_{i,K}$ defined as

$$\left(\eta^A_{i,K,n}(u_{h\tau})\right)^2 = \int_{t^{n-1}}^{t^n}\left(\|f-\partial_n u_h+\Delta u_{h\tau}\|_{L^2(K)}+\frac{1}{2\lambda_{2,K}^{1/2}}\,\|[\nabla u_{h\tau}\cdot\mathbf{n}]\|_{L^2(\partial K)}\right)$$
$$\times\left(\lambda^2_{i,K}\left(r^T_{i,K}\breve{G}_K(u_{h\tau})r_{i,K}\right)\right)^{1/2}dt.$$

Thus, condition (1.40) holds whenever for $i = 1, 2$,

$$\frac{3}{8N_V^2}\ 0.875^4\ \mathrm{TOL}^4 \left(\int_{t^{n-1}}^{t^n} \int_\Omega |\nabla u_{h\tau}|^2\ dx\ dt \right)^2 \leq \left(\eta^A_{i,P,n}(u_{h\tau})\right)^4 \leq \frac{3}{8N_V^2}\ 1.125^4\ \mathrm{TOL}^4 \left(\int_{t^{n-1}}^{t^n} \int_\Omega |\nabla u_{h\tau}|^2\ dx\ dt \right)^2 .$$

Then, for all vertices P of the mesh, a value of the mesh size $\lambda_{1,P}$ and $\lambda_{2,P}$ are computed averaging the values $\lambda_{1,K}$ and $\lambda_{2,K}$ of the triangles K containing a given vertex P. The desired stretching metric $h_{1,P}$ and $h_{2,P}$ defined in Figure 1.4 are then changed as follows. If

$$8\left(\eta^A_{i,P,n}(u_{h\tau})\right)^4 < \frac{3}{N_V^2}\ 0.875^4\ \mathrm{TOL}^4 \left(\int_{t^{n-1}}^{t^n} \int_\Omega |\nabla u_{h\tau}|^2\ dx\ dt \right)^2$$

then $h_{i,P} = \ 3/2\ \lambda_{i,P}$, $i = 1, 2$, if

$$8\left(\eta^A_{i,P,n}(u_{h\tau})\right)^4 > \frac{3}{N_V^2}\ 1.125^4\ \mathrm{TOL}^4 \left(\int_{t^{n-1}}^{t^n} \int_\Omega |\nabla u_{h\tau}|^2\ dx\ dt \right)^2$$

then $h_{i,P} = \ 2/3\ \lambda_{i,P}$, $i = 1, 2$, else $h_{i,P} = \lambda_{i,P}$, $i = 1, 2$. In practice, the error is equidistributed in the two directions of maximum and minimum stretching. This ensures conditions (1.14) and (1.16) to be fulfilled with $c = 1$. Note that we use the same algorithm with the space error estimator (1.28) and time error estimator (1.29).

Finally, we wish to align the triangles K with the eigenvectors of the matrix $\breve{G}_{K,n}$ defined in (1.27). To do so, for each vertex P of the mesh the eigenvalues of the gradient matrix

$$\breve{G}_{P,n}(u_{h\tau}) = \sum_{\substack{K \in \mathcal{T}_h \\ P \in K}} \left(\left(\eta^A_{1,K,n}(u_{h\tau})\right)^4 + \left(\eta^A_{2,K,n}(u_{h\tau})\right)^4 \right) \breve{G}_K(u_{h\tau})$$

are computed. Then θ_P defined in Figure 1.4 is set to the angle between the axis Ox and the largest eigenvalue of the matrix $\breve{G}_{P,n}$. After the space adaptation, we proceed to the time adaptation. This procedure is quite simple. We check condition (1.38) and increase or decrease the current time step if necessary. Our space and time adaptive algorithm is summarized in Figure 1.5.

Set $\mathcal{T}_h^0$, u_h^0, $n = 1$, $t = 0$	Initializations
Do while $t < T$	Time loop
$t := t + \tau_n$	Increment the current time step
Compute u_h^n on mesh $\mathcal{T}_h^{n-1}$	
Do for all triangles K of $\mathcal{T}_h^{n-1}$	
Compute $r_{1,K}$, $r_{2,K}$, $\lambda_{1,K}$, $\lambda_{2,K}$	Directions and amplitudes of stretching
Compute $\breve{G}_K$ using (1.27)	Approximated error gradient matrix
Compute $\widetilde{\eta}_{K,n}^T$ using (1.30)	Time error estimator
Compute $\eta_{K,n}^A$ using (1.28)	Space error estimator
End Do	
If (1.37) and (1.38) are satisfied	The mesh and the time step are correct
$\mathcal{T}_h^n := \mathcal{T}_h^{n-1}$	Same mesh
$n := n + 1$	Next time step
Else	
If (1.37) is not satisfied	Mesh adaptation
Do for all vertices P	
Compute $\breve{G}_{P,n}$, $\eta_{1,P,n}^A$, $\eta_{2,P,n}^A$	Averaged error indicator on vertices
Set directions of mesh anisotropy $r_{1,P}$ and $r_{2,P}$ to eigenvectors of $\breve{G}_P$	
If $\eta_{1,P,n}^A$ is too small (resp. too large) the mesh size in the first direction of anisotropy should be increased (resp. decreased)	coarsening (resp. refinement) in the direction $r_{1,P}$.
If $\eta_{2,P,n}^A$ is too small (resp. too large) the mesh size in the second direction of anisotropy should be increased (resp. decreased)	coarsening (resp. refinement) in the direction $r_{2,P}$
End Do	
Build new anisotropic mesh $\mathcal{T}_h^n$ using BL2D	
If (1.38) is not satisfied	Time adaptation
If $\sum_{K \in \mathcal{T}_h} \left(\eta_{K,n}^T(u_{h\tau})\right)^2$ is too small (resp. too large) τ_n should be increased (resp. decreased)	
$\mathcal{T}_h^{n-1} := \mathcal{T}_h^n$	
$t := t - \tau_n$	
End If	
End Do	

Figure 1.5. *Adaptive algorithm.*

1.6 A numerical study of the adaptive algorithm

We apply here the adaptive algorithm described in Figure 1.5 to several test cases requiring increasing level of mesh anisotropy. We start all our simulations on an isotropic 10×10 mesh and with the time step $\tau_1 = 0.05$ except for the third example where we start with an anisotropic 100×2 mesh. We monitor the absolute error

$$\epsilon_{abs} = \left(\int_0^T \int_\Omega |\nabla e|^2 \, dx \, dt \right)^{1/2}, \tag{1.41}$$

the relative error

$$\epsilon_{rel} = \frac{\left(\int_0^T \int_\Omega |\nabla e|^2 \, dx \, dt \right)^{1/2}}{\left(\int_0^T \int_\Omega |\nabla u_{h\tau}|^2 \, dx \, dt \right)^{1/2}}, \tag{1.42}$$

maximum and mean aspect ratio, respectively defined

$$ar = \max_{K\in\mathcal{T}_h} \frac{\lambda_{1,K}}{\lambda_{2,K}} \tag{1.43}$$

and

$$\overline{ar} = \frac{\displaystyle\sum_{K\in\mathcal{T}_h} \frac{\lambda_{1,K}}{\lambda_{2,K}}}{\displaystyle\sum_{K\in\mathcal{T}_h} 1}, \tag{1.44}$$

and the number of nodes nb_n, all computed for the mesh at final time T. We also report the number of time steps nb_τ needed to reach the final time T and the number of remeshings nb_m that occurred during the simulation.

Example 1.6.1 Set $\Omega = (0,1)\times(0,1)$ the unit square, $T = 1$ and choose u^0 and f so that the solution u of (1.1) is given by

$$u(x,y,t) = e^{-100r^2(x,y,t)},$$

where

$$r^2(x,y,t) = (x - 0.3 - 0.4\,\beta(t))^2 + (y - 0.3 - 0.4\,\beta(t))^2$$

and

$$\beta(t) = 0.5 + 0.5\tanh\left(\frac{t-0.5}{0.2}\right).$$

Thus, u is a Gaussian function, whose center moves from point $(0.3, 0.3)$ at $t = 0$ to point $(0.7, 0.7)$ at $t = 1$. The transport velocity $0.4\beta'(t)$ is maximum at $t = 0.5$, see Figure 1.6.

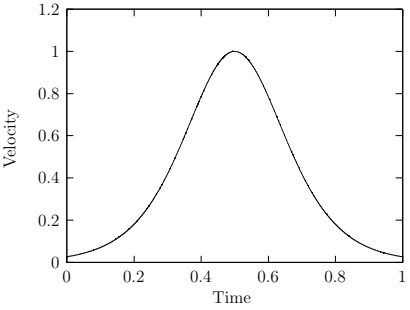

Figure 1.6. *Example 1.6.1. Transport velocity* $0.4\beta'(t)$.

Before starting our adaptive algorithm we first want to study the effectivity indices corresponding to the two time error indicators $\widehat{\eta}^T$ and $\widetilde{\eta}^T$ when using uniform time steps and mesh size. We have reported in Table 1.5 the results obtained when $h = 10\tau^2$ and $h = 160\tau^2$. We can observe that the error in the $L^2(0, T; H^1(\Omega))$ norm is $O(h+\tau^2)$, that the space error estimator and the two time error estimators are equivalent to the true error as their effectivity indices tend to a constant value and that the Zienkiewicz-Zhu error estimator is asymptotically exact. Moreover, when $h = 10\tau^2$ the time effectivity indices $\widetilde{ei}^T$ and $\widehat{ei}^T$ are similar to those of Table 1.1. On the other hand, when $h = 160\tau^2$ the error due to the time discretization is divided by 16, so as the time effectivity indices $\widetilde{ei}^T$ and $\widehat{ei}^T$. Moreover, we also report the effectivity index corresponding to time error estimator η^T defined by (1.31). As in Table 1.3, the same conclusion is drawn. This time error estimator is of suboptimal order with respect to time when considering the Crank-Nicolson method. In Figure 1.7 the value of w_h^n and $\partial_n^2 u_h$ are compared to $\partial^2 u/\partial t^2$ at time $t = 0.5$ along the axis $y = x$ and with $h = \tau = 0.00625$. We can observe that $\partial_n^2 u_h$ provides a smoother approximation of $\partial^2 u/\partial t^2$ than w_h^n. Indeed, we can notice slight oscillations when approaching $\partial^2 u/\partial t^2$ with w_h^n.

We now use the adaptive algorithm with first the three-point time error estimator (1.30) and the anisotropic space error estimator (1.28). We have reported in Table 1.6 some numerical results with several values of the tolerance TOL. We

h	τ	ϵ_{abs}	ei^{ZZ}	ei^{A}	$\widetilde{ei}^{T}$	$\widehat{ei}^{T}$	ei^{T}
0.025	0.05	0.22	0.99	2.50	17.51	14.32	3.93
0.00625	0.025	0.055	0.99	2.50	18.15	14.79	8.14
0.0015625	0.0125	0.014	1.00	2.52	18.28	14.93	16.42
0.025	0.0125	0.22	1.04	2.59	1.15	0.94	1.02
0.00625	0.00625	0.056	1.00	2.52	1.14	0.93	2.04
0.0015625	0.003125	0.014	1.00	2.52	1.14	0.93	4.10

Table 1.5. *Example 1.6.1. Convergence results using uniform isotropic meshes and constant time steps.*

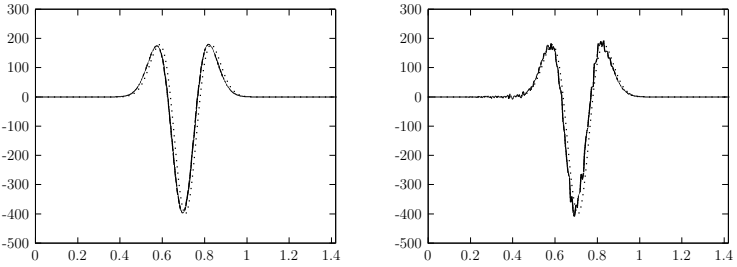

Figure 1.7. *Example 1.6.1.* $\partial_n^2 u_h$ *(solid line, left) and* w_h^n *(solid line, right) compared to* $\partial^2 u/\partial t^2$ *(dotted line) at time* $t = 0.5$ *and with* $h = \tau = 0.00625$.

observe that the error is divided by two each time the tolerance TOL is and that both the time error indicator $\widetilde{\eta}^T$ and the space error indicator η^A seem to be a good representation of the true error. Indeed, we note that the time error estimator $\widetilde{\eta}^T$ is of optimal order as the number of time steps, nb_τ, is approximatively multiplied by $\sqrt{2}$ when TOL is divided by two. The space error estimator η^A is also of optimal order as the number of nodes, nb_n, at final time is approximatively multiplied by four when TOL is divided by two. We can also note that both the space and time effectivity indices tend to a constant value which shows that η^A and $\widetilde{\eta}^T$ are equivalent to the true error.

TOL	ϵ_{rel}	ϵ_{abs}	ei^{ZZ}	ei^{A}	$\widetilde{ei}^{T}$	nb_n	nb_τ	nb_m	$\overline{ar}$	ar
0.25	0.085	0.15	0.88	2.11	2.07	854	48	18	2.41	8.34
0.125	0.043	0.76	0.88	2.12	2.02	3232	67	22	2.53	10.59
0.0625	0.022	0.038	0.88	2.11	2.02	12610	96	27	2.78	18.49
0.03125	0.011	0.019	0.87	2.09	1.95	46253	136	31	2.78	18.58

Table 1.6. *Example 1.6.1. True error and effectivity indices of the adapted solution at final time $T = 1$. The three-point time error estimator (1.30) is used.*

However, we remark that the Zienkiewicz-Zhu error estimator is not asymptotically exact. We have a value of ei^{ZZ} around 0.88 whereas we expect this value to be close to one. This discrepancy can be attributed to the interpolation error between two successive meshes that is not taken into account in our theoretical estimates. Therefore, in order to recover the asymptotical convergence of the Zienkiewicz-Zhu error estimator, we decide to replace $\nabla r_h^n(u_h^{n-1})$, in (1.39), by its Zienkiewicz-Zhu recovery, $\Pi_h^n\left(\nabla r_h^n(u_h^{n-1})\right)$. Thus, after each remeshing, we seek $u_h^n \in V_{h,n}^0$ such that $\forall v_h \in V_{h,n}^0$

$$\int_\Omega \frac{u_h^n - r_h^n(u_h^{n-1})}{\tau_n} v_h \, dx + \frac{1}{2}\int_\Omega \left(\nabla u_h^n + \Pi_h^n\left(\nabla r_h^n(u_h^{n-1})\right)\right)\cdot \nabla v_h \, dx = \frac{1}{2}\int_\Omega (f^n + f^{n-1}) v_h \, dx. \tag{1.45}$$

We have reported in Table 1.7 the corresponding results. We note a better behavior of the Zienkiewicz-Zhu error estimator since its effectivity index approaches one when the tolerance goes to zero. Moreover, all the previous observations remain unchanged, in particular, both the space and time error indicators are equivalent to the true error with the expected optimal order of convergence.

Now if $\mathcal{T}_h^{n-1}$ is identical to $\mathcal{T}_h^n$, we replace ∇u_h^{n-1}, in (1.3), by its Zienkiewicz-Zhu recovery, $\Pi_h^n\left(\nabla u_h^{n-1}\right)$, and if $\mathcal{T}_h^{n-1}$ is different from $\mathcal{T}_h^n$, we replace $\nabla r_h^n(u_h^{n-1})$, in (1.39), by its Zienkiewicz-Zhu recovery, $\Pi_h^n\left(\nabla r_h^n(u_h^{n-1})\right)$. Thus, we seek $u_h^n \in V_{h,n}^0$ such that $\forall v_h \in V_{h,n}^0$

$$\int_\Omega \frac{u_h^n - u_h^{n-1}}{\tau_n} v_h \, dx + \frac{1}{2}\int_\Omega \left(\nabla u_h^n + \Pi_h^n\left(\nabla u_h^{n-1}\right)\right)\cdot \nabla v_h \, dx = \frac{1}{2}\int_\Omega (f^n + f^{n-1}) v_h \, dx, \tag{1.46}$$

TOL	ϵ_{rel}	ϵ_{abs}	ei^{ZZ}	ei^{A}	$\widetilde{ei}^{T}$	nb_n	nb_τ	nb_m	$\overline{ar}$	ar
0.25	0.08	0.14	0.93	2.24	2.17	877	48	17	2.37	11.27
0.125	0.04	0.7	0.95	2.29	2.15	2902	67	22	2.59	12.06
0.0625	0.02	0.034	0.97	2.34	2.22	10794	95	27	2.76	13.34
0.03125	0.01	0.017	0.98	2.34	2.20	47386	136	30	2.89	16.42

Table 1.7. *Example 1.6.1. True error and effectivity indices of the adapted solution at final time $T = 1$ when solving (1.3) if $\mathcal{T}_h^{n-1} = \mathcal{T}_h^n$ and (1.45) if $\mathcal{T}_h^{n-1} \neq \mathcal{T}_h^n$. The three-point time error estimator (1.30) is used.*

TOL	ϵ_{rel}	ϵ_{abs}	ei^{ZZ}	ei^{A}	$\widetilde{ei}^{T}$	nb_n	nb_τ	nb_m	$\overline{ar}$	ar
0.25	0.078	0.134	0.99	2.37	2.30	853	48	18	2.42	9.84
0.125	0.039	0.066	0.99	2.38	2.28	3189	67	23	2.54	10.47
0.0625	0.02	0.034	1.00	2.38	2.23	11714	96	27	2.79	14.82
0.03125	0.01	0.017	1.00	2.38	2.24	48062	135	30	2.92	18.72

Table 1.8. *Example 1.6.1. True error and effectivity indices of the adapted solution at final time $T = 1$ when solving (1.46) if $\mathcal{T}_h^{n-1} = \mathcal{T}_h^n$ and (1.45) if $\mathcal{T}_h^{n-1} \neq \mathcal{T}_h^n$. The three-point time error estimator (1.30) is used.*

if $\mathcal{T}_h^{n-1}$ and $\mathcal{T}_h^n$ are identical and (1.45) if $\mathcal{T}_h^{n-1}$ and $\mathcal{T}_h^n$ are different. We have reported in Table 1.8 the corresponding results. We now observe that the Zienkiewicz-Zhu error estimator is asymptotically exact as its effectivity index is close to one. All the previous observations remain unchanged, especially the good behavior of both the space and time error indicators. We have reported in Figure 1.10 the corresponding numerical simulation when the tolerance TOL=0.125.

In Figure 1.8 we also plot the evolution of the number of nodes and time step size against time when the tolerance TOL=0.125. We observe that the number of nodes remains almost constant whereas the time step size decreases until $t = 0.5$ and increases until final time $T = 1$. The evolution of the time step size thus fits the transport velocity, see Figure 1.6. Thus, the three-point time error estimator $\widetilde{\eta}^T$ seems to be a good approximation of the true error. Finally, we plot in Figure 1.9 the value of $\partial_n^2 u_h$ when solving (1.3) if $\mathcal{T}_h^{n-1} = \mathcal{T}_h^n$ and (1.39) if $\mathcal{T}_h^{n-1} \neq \mathcal{T}_h^n$ and when solving (1.46) if $\mathcal{T}_h^{n-1} = \mathcal{T}_h^n$ and (1.45) if $\mathcal{T}_h^{n-1} \neq \mathcal{T}_h^n$ compared to $\partial^2 u/\partial t^2$

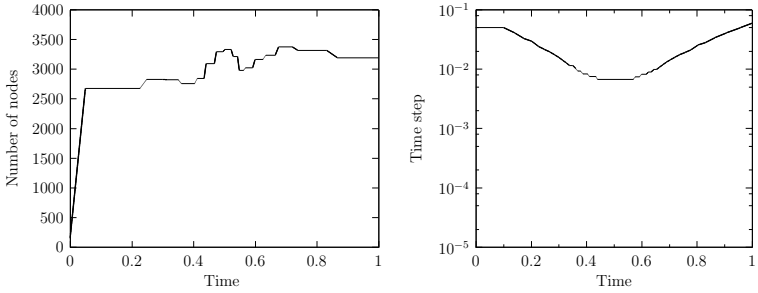

Figure 1.8. *Example 1.6.1. Number of nodes (left) and time step size (right) with respect to time t when solving (1.46) if* $\mathcal{T}_h^{n-1} = \mathcal{T}_h^n$ *and (1.45) if* $\mathcal{T}_h^{n-1} \neq \mathcal{T}_h^n$*. The time error estimator is given by (1.30) and TOL=0.125.*

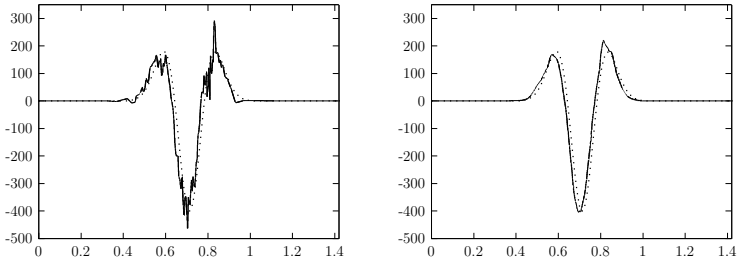

Figure 1.9. *Example 1.6.1.* $\partial_n^2 u_h$ *(solid line) compared to* $\partial^2 u/\partial t^2$ *(dotted line) at time* $t = 0.5$ *and when TOL=0.125. Left: we solve (1.3) if* $\mathcal{T}_h^{n-1} = \mathcal{T}_h^n$ *and (1.39) if* $\mathcal{T}_h^{n-1} \neq \mathcal{T}_h^n$*. Right: we solve (1.46) if* $\mathcal{T}_h^{n-1} = \mathcal{T}_h^n$ *and (1.45) if* $\mathcal{T}_h^{n-1} \neq \mathcal{T}_h^n$*.*

at time $t = 0.5$ along the axis $y = x$ and when TOL=0.125. We note a better approximation of $\partial^2 u/\partial t^2$ when solving (1.46) if $\mathcal{T}_h^{n-1} = \mathcal{T}_h^n$ and (1.45) if $\mathcal{T}_h^{n-1} \neq \mathcal{T}_h^n$.

We now use the time error estimator (1.29) instead of (1.30) in the adaptive algorithm and we have reported in Table 1.9 some numerical results with several values of tolerance TOL. The results obtained show that the good behavior observed in the case of constant space and time steps is not preserved when using our adaptive algorithm. Indeed, we can see that the time error indicator $\widehat{\eta}^T$ is

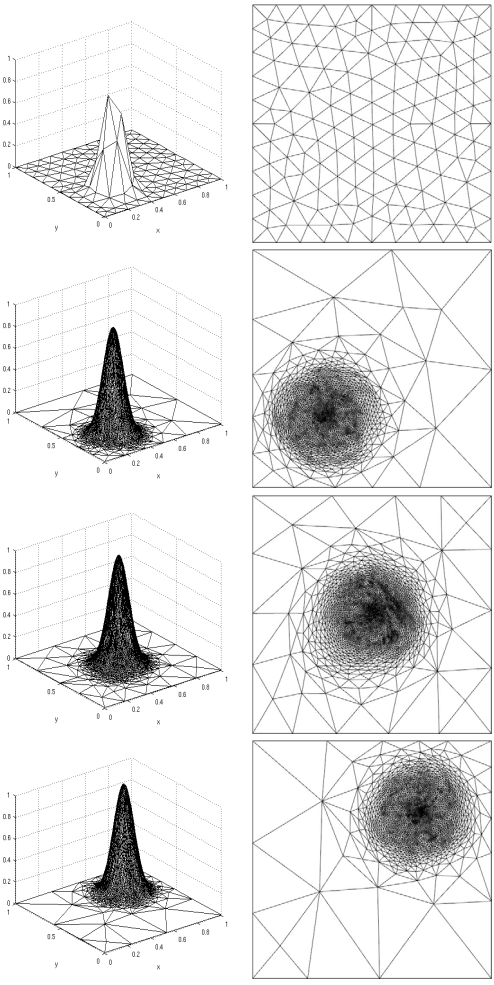

Figure 1.10. *Example 1.6.1. Adapted meshes and solutions obtained with the time error estimator (1.30) and TOL=0.125 when solving (1.46) if* $\mathcal{T}_h^{n-1} = \mathcal{T}_h^n$ *and (1.45) if* $\mathcal{T}_h^{n-1} \neq \mathcal{T}_h^n$*. From top to bottom: time t=0, 0.05, 0.5 and 1 (151, 2674, 3333 and 3189 nodes, respectively).*

TOL	ϵ_{rel}	ϵ_{abs}	ei^{ZZ}	ei^{A}	$\widehat{ei}^{T}$	nb_n	nb_τ	nb_m	$\overline{ar}$	ar
0.25	0.074	0.128	1.00	2.39	2.25	885	620	15	2.38	9.52
0.125	0.038	0.066	1.00	2.40	2.14	2871	1860	19	2.70	16.45
0.0625	0.019	0.033	1.00	2.40	2.20	11924	4882	22	2.71	12.68
0.03125	0.01	0.017	1.00	2.39	2.20	48038	23851	26	2.95	19.51

Table 1.9. *Example 1.6.1. True error and effectivity indices of the adapted solution at final time $T = 1$. The two-point time error estimator (1.29) is used.*

not of optimal order of convergence since the number of time steps, nb_τ, is not multiplied by $\sqrt{2}$ when we divide TOL by two. For a tolerance TOL=0.125, the number of time steps was of 67 when using the time error indicator $\widetilde{\eta}^T$ whereas it becomes 1860 for the time error indicator $\widehat{\eta}^T$. This significant difference shows that $\widehat{\eta}^T$ tends to dramatically over-predict the true error.

In Figure 1.11 we plot the evolution of the number of nodes and time step size against time when the tolerance TOL=0.125. We can see that the evolution of the number of nodes is similar to that presented in Figure 1.8. On the other hand, the time step evolution is completely different and shows an irregular progression with very small time steps around a value of 0.005. In order to reduce this over-prediction, we decide to solve (1.46) if $\mathcal{T}_h^{n-1} = \mathcal{T}_h^n$ and (1.45) if $\mathcal{T}_h^{n-1} \neq \mathcal{T}_h^n$. We plot in Figure 1.12 the corresponding evolution of the number of nodes and the time step size against time when the tolerance TOL=0.125. We can see that the evolution of the number of nodes still be similar to that presented in Figures 1.8 or 1.11. The time step evolution is more interesting. Indeed, the irregular profile is still here but the general aspect of the evolution of the time step seems to be closer to the one presented in Figure 1.8 than to that of Figure 1.11. Indeed, neglecting these oscillations we roughly have the same evolution as in Figure 1.8.

We suspect that this irregular profile is due to the interpolation error after each remeshing. Thus, we introduce the relative two-point time error estimator $\widehat{\eta}_{rel}^n$ defined by

$$\widehat{\eta}_{rel}^n = \frac{\displaystyle\sum_{K\in\mathcal{T}_h} \left(\widehat{\eta}_{K,n}^T(u_{h\tau})\right)^2}{\displaystyle\int_{t^{n-1}}^{t^n}\int_\Omega |\nabla u_{h\tau}|^2 \, dx \, dt} \tag{1.47}$$

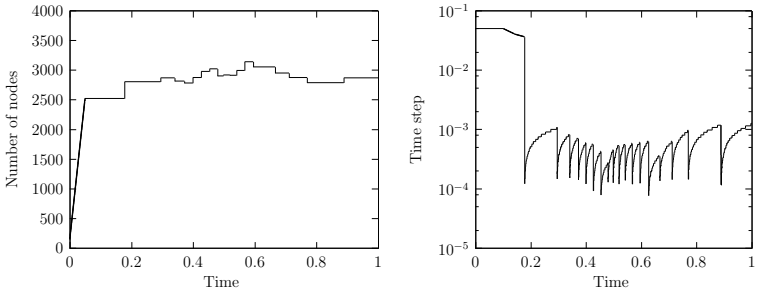

Figure 1.11. *Example 1.6.1. Number of nodes (left) and time step size (right) with respect to time t. The time error estimator is given by (1.29) and TOL=0.125.*

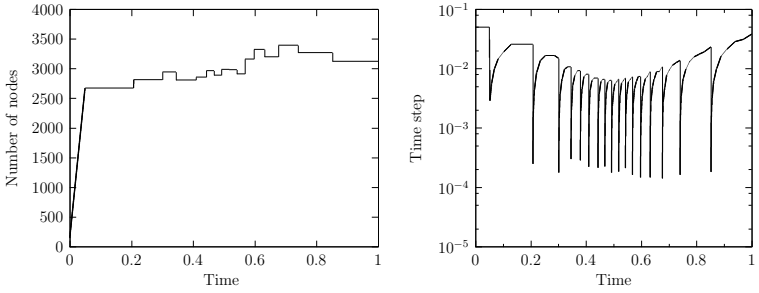

Figure 1.12. *Example 1.6.1. Number of nodes (left) and time step size (right) with respect to time t when solving (1.46) if $\mathcal{T}_h^{n-1} = \mathcal{T}_h^n$ and (1.45) if $\mathcal{T}_h^{n-1} \neq \mathcal{T}_h^n$. The time error estimator is given by (1.29) and TOL=0.125.*

and the relative error ϵ_{rel}^n defined by

$$\epsilon_{rel}^n = \frac{\displaystyle\int_{t^{n-1}}^{t^n} \int_\Omega |\nabla e|^2 \, dx \, dt}{\displaystyle\int_{t^{n-1}}^{t^n} \int_\Omega |\nabla u_{h\tau}|^2 \, dx \, dt}. \tag{1.48}$$

In Figure 1.13 the evolution of this two quantities is reported for a tolerance TOL=0.125 when solving (1.46) if $\mathcal{T}_h^{n-1} = \mathcal{T}_h^n$ and (1.45) if $\mathcal{T}_h^{n-1} \neq \mathcal{T}_h^n$. We can

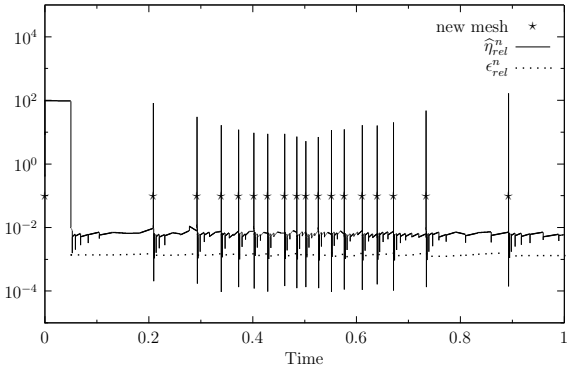

Figure 1.13. *Example 1.6.1. Evolution of $\widehat{\eta}^n_{rel}$ and ϵ^n_{rel} when solving (1.46) if $\mathcal{T}_h^{n-1} = \mathcal{T}_h^n$ and (1.45) if $\mathcal{T}_h^{n-1} \neq \mathcal{T}_h^n$. The time error estimator is given by (1.29) and TOL=0.125.*

TOL	ϵ_{rel}	ϵ_{abs}	ei^{ZZ}	ei^{A}	$\widehat{ei}^{T}$	nb_n	nb_τ	nb_m	$\overline{ar}$	ar
0.25	0.078	0.133	1.00	2.40	2.28	852	71	15	2.44	10.66
0.125	0.038	0.066	1.00	2.41	2.20	3125	127	18	2.67	12.53
0.0625	0.019	0.033	1.00	2.41	2.17	12347	260	23	2.89	16.86
0.03125	0.0096	0.0166	1.00	2.40	2.18	47513	1695	25	3.01	20.57

Table 1.10. *Example 1.6.1. True error and effectivity indices of the adapted solution at final time $T = 1$ when solving (1.46) if $\mathcal{T}_h^{n-1} = \mathcal{T}_h^n$ and (1.45) if $\mathcal{T}_h^{n-1} \neq \mathcal{T}_h^n$. The two-point time error estimator (1.29) is used.*

see that each remeshing results in a jump of the two-point time error estimator that causes the irregular evolution. In Table 1.10 we have reported the numerical results for several values of tolerance TOL when solving (1.46) if $\mathcal{T}_h^{n-1} = \mathcal{T}_h^n$ and (1.45) if $\mathcal{T}_h^{n-1} \neq \mathcal{T}_h^n$. We see that the number of time steps, nb_τ, is not multiplied by $\sqrt{2}$ when we divide TOL by two, so the optimal order of convergence is not recovered. Finally, in Figure 1.14 we plot the value of w_h^n compared to $\partial^2 u/\partial t^2$ at time $t = 0.5$ along the axis $y = x$ and when TOL=0.125. Two implementations of our adaptive algorithm are reported there: firstly when solving (1.3) if $\mathcal{T}_h^{n-1} = \mathcal{T}_h^n$ and (1.39) if $\mathcal{T}_h^{n-1} \neq \mathcal{T}_h^n$, and secondly when solving (1.46) if $\mathcal{T}_h^{n-1} = \mathcal{T}_h^n$ and

(1.45) if $\mathcal{T}_h^{n-1} \neq \mathcal{T}_h^n$. We can see that w_h^n does not at all approach $\partial^2 u/\partial t^2$ if the Zienkiewicz-Zhu recovery method is not used. The huge oscillations of w_h^n observed in this case can explain why the time error indicator $\widehat{\eta}^T$ extensively over-predicts the true error. A much better behavior of w_h^n is observed if we solve (1.46) when $\mathcal{T}_h^{n-1} = \mathcal{T}_h^n$ and (1.45) when $\mathcal{T}_h^{n-1} \neq \mathcal{T}_h^n$. However, this approximation also suffers from important spurious oscillations and it is still not good enough to recover the optimal order of convergence of the time error estimator $\widehat{\eta}^T$.

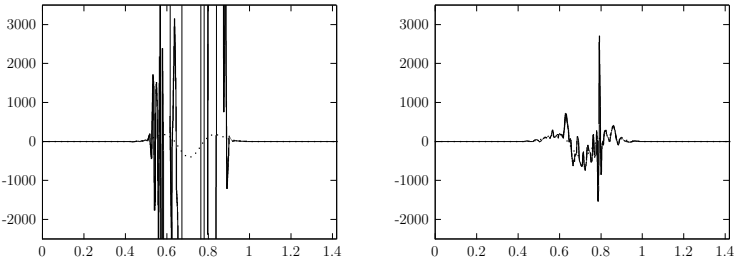

Figure 1.14. *Example 1.6.1.* w_h^n *(solid line) compared to* $\partial^2 u/\partial t^2$ *(dotted line) at time* $t = 0.5$ *and when TOL=0.125. Left: We solve (1.3) if* $\mathcal{T}_h^{n-1} = \mathcal{T}_h^n$ *and (1.39) if* $\mathcal{T}_h^{n-1} \neq \mathcal{T}_h^n$*. Right: We solve (1.46) if* $\mathcal{T}_h^{n-1} = \mathcal{T}_h^n$ *and (1.45) if* $\mathcal{T}_h^{n-1} \neq \mathcal{T}_h^n$*.*

We now consider another test case with more anisotropic finite elements. We do all the computations by replacing ∇u_h^{n-1} and $\nabla r_h^n(u_h^{n-1})$, respectively in (1.3) and in (1.39), by its Zienkiewicz-Zhu recovery, respectively $\Pi_h^n\left(\nabla u_h^{n-1}\right)$ and $\Pi_h^n\left(\nabla r_h^n(u_h^{n-1})\right)$.

Example 1.6.2 Set $\Omega = (0,1)\times(0,1)$ the unit square, $T = 1$ and choose u^0 and f so that the solution u of (1.1) is given by

$$u(x,y,t) = 0.5 - 0.5\ \tanh\left(\frac{r(x,y) - 0.15 - 0.2\ \beta_1(t)}{0.005}\right),$$

where

$$r(x,y) = \sqrt{(x-0.5)^2 + (y-0.5)^2}$$

and

$$\beta_1(t) = \begin{cases} 0.7t + 0.035\ \ln\left(\exp\left(\dfrac{t-0.2}{0.05}\right) + \exp\left(-\dfrac{t-0.2}{0.05}\right)\right) & \text{if } t \leq 0.5, \\ 0.42 + 0.7t - 0.035\ \ln\left(\exp\left(\dfrac{t-0.8}{0.05}\right) + \exp\left(-\dfrac{t-0.8}{0.05}\right)\right) & \text{if } t > 0.5. \end{cases}$$

Thus, u is smooth, varies from one to zero through a narrow region of width 0.005. This region moves with normal velocity $0.2\beta_1'(t)$, see Figure 1.15. We first use the adaptive algorithm with the three-point time error estimator $\widetilde{\eta}^T$. The numerical simulation is reported in Figure 1.17 when the tolerance TOL=0.25. We plot in Figure 1.16 the evolution of the number of nodes and the time step size against time. We observe that the number of nodes remains almost constant whereas the time step size decreases or increases according to the velocity. In Table 1.11 we have reported numerical results for several values of tolerance TOL. We observe that η^{ZZ} is asymptotically exact and both η^A and $\widetilde{\eta}^T$ are equivalent to the true error. We also note that the time error estimator $\widetilde{\eta}^T$ is of optimal order since the number of time steps is multiplied by $\sqrt{2}$ each time TOL is divided by two.

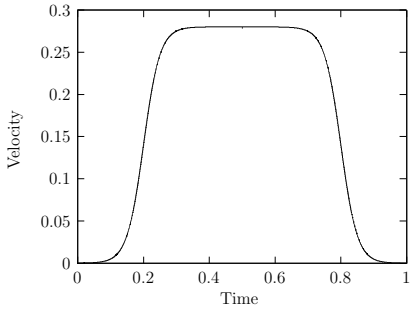

Figure 1.15. *Example 1.6.2. Normal velocity* $0.2\beta_1'(t)$.

TOL	ϵ_{rel}	ϵ_{abs}	ei^{ZZ}	ei^A	$\widetilde{ei}^T$	nb_n	nb_τ	nb_m	$\overline{ar}$	ar
0.25	0.074	0.78	1.00	2.87	2.87	5359	762	96	8.5	45.8
0.125	0.03	0.31	1.00	2.86	2.79	20079	1124	89	9.0	49.6
0.0625	0.016	0.16	1.00	2.88	2.78	84199	1569	91	9.7	73.6
0.03125	0.0077	0.081	1.00	2.87	2.83	362235	2175	92	9.8	149

Table 1.11. *Example 1.6.2. True error and effectivity indices of the adapted solution at final time* $T = 1$. *The three-point time error estimator (1.30) is used.*

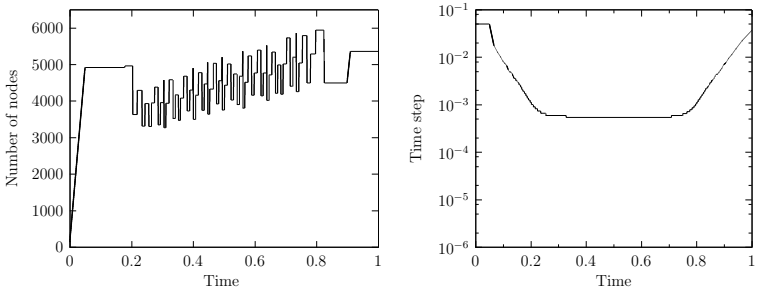

Figure 1.16. *Example 1.6.2. Number of nodes (left) and time step size (right) with respect to time t. The time error estimator is given by (1.30) and TOL=0.25.*

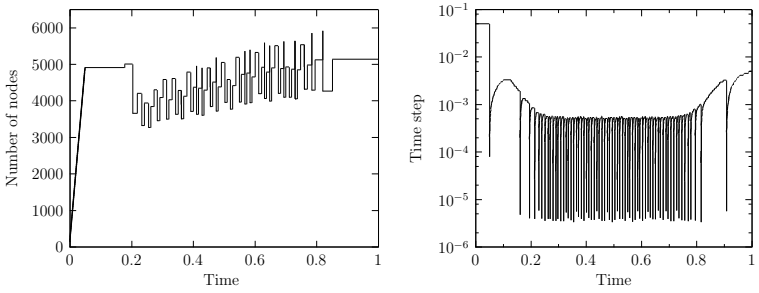

Figure 1.18. *Example 1.6.2. Number of nodes (left) and time step size (right) with respect to time t. The two-point time error estimator is given by (1.29) and TOL=0.25.*

We now use (1.29) instead of (1.30) in the adaptive algorithm. We do the same experiment as in Figures 1.17, 1.16 and plot in Figure 1.18 the number of nodes and the time step evolution. The evolution of the number of nodes is qualitatively the same as in the previous case whereas the time step evolution exhibits the same irregular evolution as in Figure 1.12. We have reported in Table 1.12 the numerical results for several values of tolerance TOL. We see that the number of time steps, nb_τ, is almost doubled when the tolerance TOL is divided by two so the optimality of the two-point time error estimator $\widehat{\eta}^T$ is not recovered. Moreover, we have reported in Figure 1.19 the evolution of the relative two-point time error

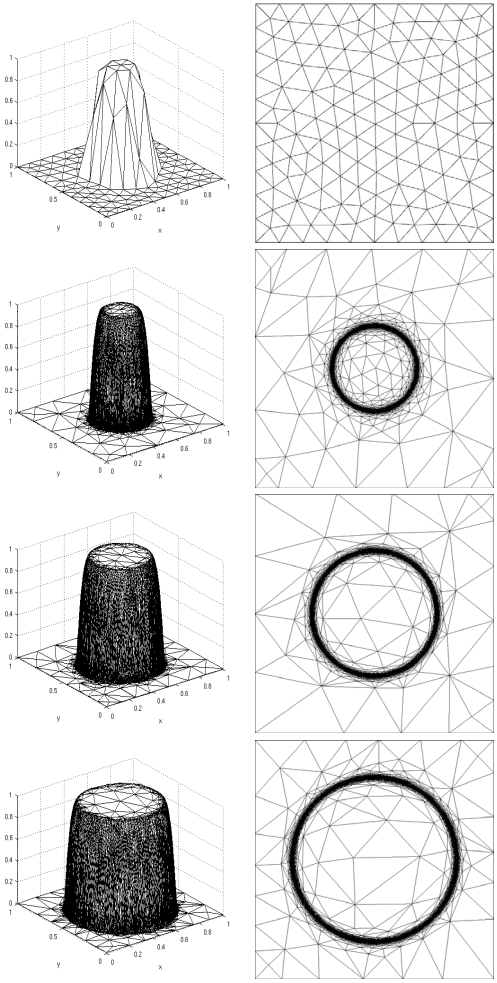

Figure 1.17. *Example 1.6.2. Adapted meshes and solutions obtained with the time error estimator (1.30) and the tolerance TOL=0.25. From top to bottom: time t=0, 0.05, 0.5 and 1 (151, 4917, 3757 and 5359 nodes, respectively).*

TOL	ϵ_{rel}	ϵ_{abs}	ei^{ZZ}	ei^{A}	$\widehat{ei}^{T}$	nb_n	nb_τ	nb_m	$\overline{ar}$	ar
0.25	0.06	0.64	1.01	2.86	2.75	5319	1088	100	8.68	39.10
0.125	0.03	0.32	1.00	2.87	2.72	17435	1734	91	9.14	46.36
0.0625	0.015	0.16	1.00	2.88	2.64	69224	4654	93	9.40	43.00

Table 1.12. *Example 1.6.2. True error and effectivity indices of the adapted solution at final time $T = 1$. The two-point time error estimator (1.29) is used.*

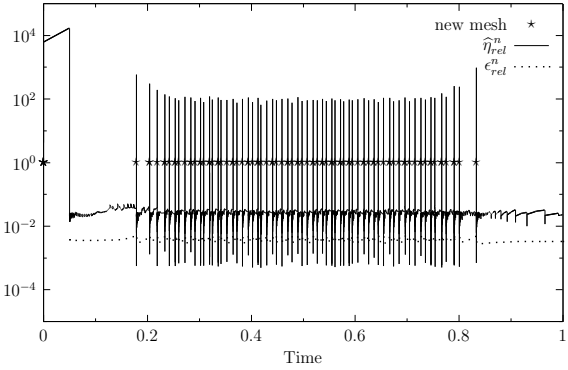

Figure 1.19. *Example 1.6.2. Evolution of $\widehat{\eta}^n_{rel}$ and ϵ^n_{rel}. The time error estimator is given by (1.29) and TOL=0.25.*

estimator (1.47) and the relative error (1.48). We can see the same phenomenon as in the previous example, that is to say an over estimation of the true error after each remeshing.

Our last test case illustrates the situation where the solution varies in only one direction and thus leads to very stretched meshes. We still do all the computations by replacing ∇u_h^{n-1} and $\nabla r_h^n(u_h^{n-1})$, respectively in (1.3) and in (1.39), by its Zienkiewicz-Zhu recovery, respectively $\Pi_h^n\left(\nabla u_h^{n-1}\right)$ and $\Pi_h^n\left(\nabla r_h^n(u_h^{n-1})\right)$.

Example 1.6.3 Set $\Omega = (0,1) \times (0,1)$ the unit square, $T = 1.5$ and choose u^0 and f so that the solution u of (1.1) is given by

$$u(x,y,t) = 0.5 + 0.5 \ \tanh\left(\frac{x - 0.2 - 0.3 \ \beta_2(t)}{0.05}\right),$$

where

$$\beta_2(t) = \begin{cases} 0.5 + 0.5 \ \tanh\left(\dfrac{t - 0.4}{0.05}\right) & \text{if } t \leq 0.75, \\ 1.5 + 0.5 \ \tanh\left(\dfrac{t - 1.1}{0.05}\right) & \text{if } t > 0.75. \end{cases}$$

Note that we consider here a problem with mixed Dirichlet-Neumann boundary condition. Indeed, we fixe $u = 0$ on $\{(x,y) \in \partial\Omega : x = 0\}$ and $u = 1$ on $\{(x,y) \in \partial\Omega : x = 1\}$ and impose homogeneous Neumann boundary condition on $\{(x,y) \in \partial\Omega : y = 0 \text{ or } y = 1\}$. Thus, the solution u exhibits an internal layer moving with a velocity $0.3\beta_2'(t)$ having sharp peaks centered at times $t = 0.4$ and $t = 1.1$, see Figure 1.20.

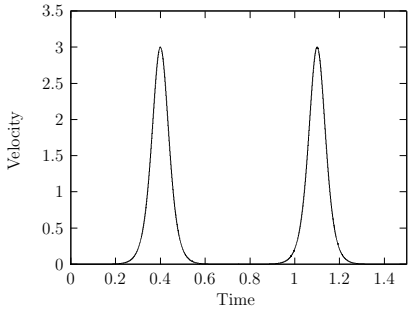

Figure 1.20. *Example 1.6.3. Transport velocity* $0.3\beta_2'(t)$.

We apply the adaptive algorithm with the three-point time error estimator $\widetilde{\eta}^T$. Adapted meshes are shown in Figure 1.21 when the tolerance TOL=0.03125. We plot in Figure 1.22 the evolution of the number of nodes and the time step size against time. We observe two slight variations of the number of nodes at $t = 0.4$ and $t = 1.1$ corresponding to the peaks of acceleration and deceleration of the velocity. The time step evolution is again as we expected and follows the

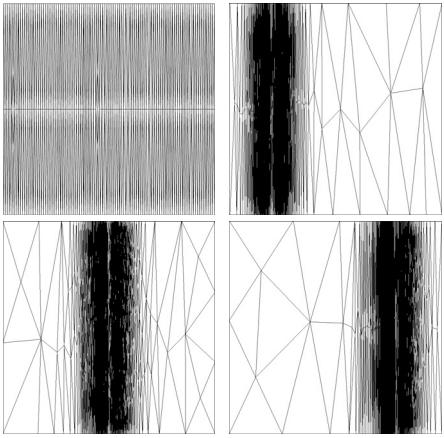

Figure 1.21. *Example 1.6.3. Adapted meshes obtained with the time error estimator (1.30) and the tolerance TOL=0.03125. From left to right, top to bottom: time t=0, 0.05, 1 and 1.5 (320, 1042, 1015 and 892 nodes, respectively).*

TOL	ϵ_{rel}	ϵ_{abs}	ei^{ZZ}	ei^{A}	$\widetilde{ei}^{T}$	nb_n	nb_τ	nb_m	$\overline{ar}$	ar
0.125	0.03	0.095	0.99	2.87	2.68	155	142	84	63	231
0.0625	0.015	0.046	0.99	2.89	2.91	348	201	52	108	519
0.03125	0.007	0.022	0.99	2.96	2.99	892	285	52	165	705
0.015625	0.004	0.012	1.00	2.88	2.71	4408	401	40	118	847

Table 1.13. *Example 1.6.3. True error and effectivity indices of the adapted solution at final time $T = 1.5$. The time error estimator (1.30) is used.*

velocity profile of the solution. Thus, for high velocity the adaptive algorithm chooses to use small time step and vice-versa. In Table 1.13 we have reported numerical experiments with several values of tolerance TOL. We observe that η^{ZZ} is asymptotically exact and that the space anisotropic error estimator η^A and the three-point time error estimator $\widetilde{\eta}^T$ are equivalent to the true error. The number of time steps is approximatively multiply by $\sqrt{2}$ when TOL is divided by two so that the optimal order is again recovered.

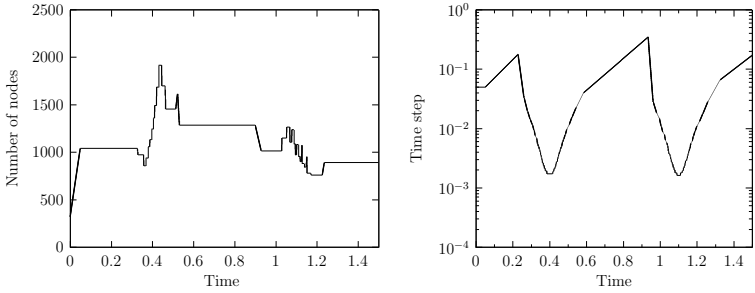

Figure 1.22. *Example 1.6.3. Number of nodes (left) and time step size (right) with respect to time t. The time error estimator is given by (1.30) and TOL=0.03125.*

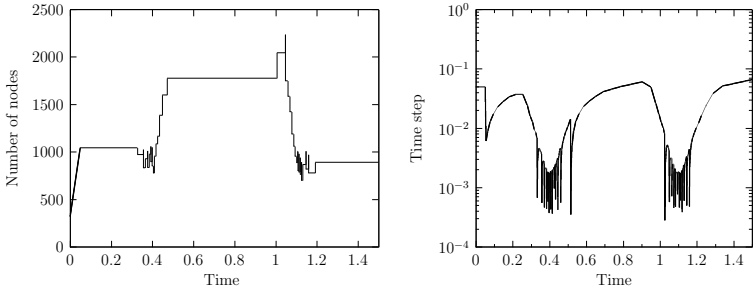

Figure 1.23. *Example 1.6.3. Number of nodes (left) and time step size (right) with respect to time t. The time error estimator is given by (1.29) and TOL=0.03125.*

We now use (1.29) instead of (1.30) in the adaptive algorithm. Since the Dirichlet boundary conditions are prescribed only on the part of the boundary in this example, the two-point time error estimator, namely the definition of w_h^n (1.12), should be changed. We require here w_h^n to vanish only on $\{(x, y) \in \partial\Omega : x = 0 \text{ or } x = 1\}$ and leave it free on $\{(x, y) \in \partial\Omega : y = 0 \text{ or } y = 1\}$. The evolution of the number of nodes and the time step size against time is reported in Figure 1.23 for the same simulation as in Figures 1.21, 1.22. We observe in Figure 1.23 that the number of nodes increases after the first peak, stays approximatively constant between the two peaks and finally decreases after the second peak. The time step

TOL	ϵ_{rel}	ϵ_{abs}	ei^{ZZ}	ei^{A}	$\widehat{ei}^{T}$	nb_n	nb_τ	nb_m	$\overline{ar}$	ar
0.125	0.03	0.09	1.01	2.93	2.85	163	187	81	69	305
0.0625	0.015	0.046	1.00	2.98	2.83	345	301	57	109	479
0.03125	0.0075	0.023	1.00	2.95	2.96	892	909	52	169	948
0.015625	0.0037	0.011	1.00	2.89	2.95	6054	10147	38	86	904

Table 1.14. *Example 1.6.3. True error and effectivity indices of the adapted solution at final time $T = 1.5$. The time error estimator (1.29) is used.*

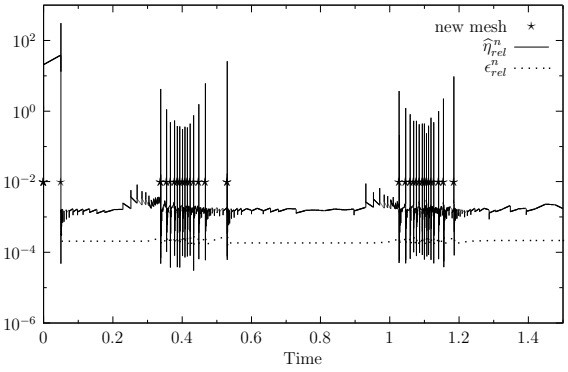

Figure 1.24. *Example 1.6.3. Evolution of $\widehat{\eta}^n_{rel}$ and ϵ^n_{rel}. The time error estimator is given by (1.29) and TOL=0.03125.*

evolution is more chaotic. Indeed, we observe many perturbations, which most important of them appear during the two peaks of acceleration and deceleration. We can also note that between the two peaks, when the velocity is very small, the time step stays approximatively constant around a value of 0.02 whereas we expect an increase. For solutions exhibiting high aspect ratio the behavior of the two-point time error estimator seems then not to be a really good representation of the error. In Table 1.14 we have reported some numerical results with several values of tolerance TOL. We see that the two-point time error estimator is not of optimal order as the number of time iteration grows when the tolerance is divided by two. Finally we reported in Figure 1.24 the evolution of the relative two-point

time error estimator (1.47) and the relative error (1.48). The same over estimation of the true error appears each time we build a new mesh.

1.7 Conclusion

All numerical experiments show that $\widetilde{\eta}^T$ provides a good representation of the true error even with solutions exhibiting high aspect ratio finite elements. Indeed, the expected second order of convergence with respect to time has been recovered for all the three test cases. However, for the time error estimator $\widehat{\eta}^T$, we did not manage to recover the optimal second order of convergence when using our adaptive algorithm. The difficulty in approximating ∇w_h^n involved in $\widehat{\eta}^T$ after each remeshing seems to be the major problem of this approach . We now looking forward to extend these results to a second model problem, the time-dependent convection-diffusion problem discretized in time using the Crank-Nicolson method. Finally, we report in Figure 1.25 the anisotropy corresponding to the three test cases reported in Figures 1.10, 1.17 and 1.21 with a zoom on the characteristic features of the meshes.

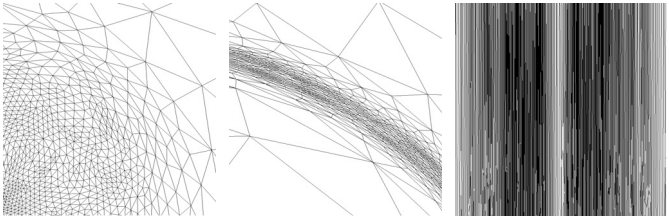

Figure 1.25. *Zoom on the three adapted meshes for the simulations reported in Figures 1.10, 1.17 and 1.21 at their respective final time.*

Chapter 2

A posteriori error estimator for the Crank-Nicolson scheme. Second model problem: The time dependent convection-diffusion equation

An a posteriori upper bound is derived for the time-dependent convection-diffusion problem using continuous, piecewise linear stabilized finite elements with large aspect ratio for the space discretization and the Crank-Nicolson scheme for the time discretization. It is based on the three-point quadratic time reconstruction $\widetilde{u}_{h\tau}$ defined by (1.13). A space and time adaptive algorithm is developed to ensure the control of the relative error in the $L^2(0,T;H^1(\Omega))$ norm. Numerical experiments illustrating the efficiency of this approach are reported. It is shown that the time error indicator is of optimal order with respect to both the mesh size and the time step, even in the convection dominated regime and in presence of boundary layers.

Contents

2.1 Situation

Deriving robust a posteriori error estimators for the stationary convection-diffusion problems with continuous, piecewise linear stabilized finite elements has generated a lot of papers, from both theoretical and experimental point of views, see for instance [14, 56, 57, 58, 59] for isotropic meshes and [60, 61, 30, 62] for anisotropic meshes. However, fewer papers are available for the nonstationary case, we refer for instance to [63] or [64, 65] for error estimates based on the discontinuous Galerkin method.

Concerning parabolic problems and the Crank-Nicolson scheme, it was observed in Section 2.1 of [32] that applying energy technique with a standard continuous piecewise linear approximation in time would yield to a suboptimal a posteriori error estimator for the time discretization. The so-called Crank-Nicolson reconstruction was then introduced in order to restore the appropriate rate of convergence in time. In this work, the authors derived optimal order a posteriori error estimators in the framework of a semi-discrete time discretization. In the previous Chapter, two quadratic time reconstructions were considered. Following [32], we introduce the two-point quadratic time reconstruction. This reconstruction allows us to derive optimal order a posteriori error estimators in the fully discrete situation. However, a jump of the corresponding time error estimator was observed after each remeshing when using our space and time adaptive algorithm disallowing the expected optimal order of convergence to be recovered.

An alternative piecewise quadratic time reconstruction was then proposed, the three-point reconstruction, based on a finite difference approximation of $\partial^2 u/\partial t^2$. A posteriori time error estimator was then derived and optimal order with respect to both the mesh size and the time step was obtained when using our adaptive algorithm. In this Chapter, we will extend this result, obtained for the heat equation, to the time-dependent convection-diffusion problem. An optimal order a posteriori upper bound based on the three-point quadratic time reconstruction will be derived. We will then test the quality of the derived error indicators in the convection dominated regime and in presence of boundary layers.

The Chapter is organized as follows. In Section 2.2 we introduce the model problem and its space and time discretization. Then, we derive in Section 2.3 an a posteriori upper bound for the error, the involved constant being independent of the time step, mesh size and aspect ratio. In Section 2.4, we recall briefly the space and time adaptive algorithm. Finally in Section 2.5, we present numerical experiments on several test cases and conclude with the numerical simulation of the transport of a sample concentration in a long rectangular channel.

2.2 The model problem and its discretization

Let Ω be a polygonal domain with boundary $\partial\Omega$, $T > 0$ the final time, $\epsilon > 0$ the diffusion coefficient, $a : \Omega \times (0,T) \to \mathbb{R}^2$ an incompressible velocity field, $f : \Omega \times (0,T) \to \mathbb{R}$ a source term, $u^0 : \Omega \to \mathbb{R}$ the initial condition. We consider the following problem. Find $u : \Omega \times (0,T) \to \mathbb{R}$ such that

$$\begin{cases} \dfrac{\partial u}{\partial t} - \epsilon\Delta u + a \cdot \nabla u = f & \text{in } \Omega \times (0,T), \\ u = 0 & \text{on } \partial\Omega \times (0,T), \\ u(\cdot,0) = u^0 & \text{in } \Omega. \end{cases} \tag{2.1}$$

The weak formulation corresponding to (2.1) is as follows, see for instance [48]. Recall that W is the functional space defined by

$$W = \{w \in L^2(0,T; H_0^1(\Omega)) \text{ and } \partial w/\partial t \in L^2(0,T; H^{-1}(\Omega))\}.$$

Given $a \in \mathcal{C}^1(\bar{\Omega}\times[0,T])$ such that div $a = 0$, $f \in L^2(0,T; H^{-1}(\Omega))$ and $u^0 \in L^2(\Omega)$, we seek for a solution $u \in W$ such that $u(\cdot,0) = u^0$ and $\forall v \in H_0^1(\Omega)$ and a.e. $t \in (0,T)$,

$$\left\langle \frac{\partial u}{\partial t}, v \right\rangle + \epsilon \int_\Omega \nabla u \cdot \nabla v \; dx + \int_\Omega (a \cdot \nabla u) v \; dx = \langle f, v \rangle \,, \tag{2.2}$$

where $< \cdot, \cdot >$ denotes the duality pairing between $H^{-1}(\Omega)$ and $H_0^1(\Omega)$.

It is well know that standard Galerkin space discretization of (2.2) leads to spurious oscillations in the convection dominated regime. A remedy is to use stabilized finite element method, see for instance [66, 67, 68] and references therein. Thus, in order to approximate the solution of the above problem, we consider the classical Galerkin Least Squares method (GLS) with a modified stabilization parameter due to the use of anisotropic finite elements, see [50] for a theoretical justification in the framework of stationary convection-diffusion. We keep the same notations as in the previous Chapter for the space and time discretization. Then assume that $f \in \mathcal{C}^0([0,T]; L^2(\Omega))$ and $u^0 \in \mathcal{C}^0(\bar{\Omega})$, set $f^n(\cdot) = f(\cdot, t^n)$ and $u_h^0 = r_h u^0$, the Crank-Nicolson scheme consists in seeking $u_h^n \in V_h^0$ such that for all $v_h \in V_h^0$ we have

$$\begin{aligned} &\int_\Omega \frac{u_h^n - u_h^{n-1}}{\tau_n} v_h \; dx + \frac{\epsilon}{2} \int_\Omega \nabla(u_h^n + u_h^{n-1}) \cdot \nabla v_h \; dx + \frac{1}{2} \int_\Omega a \cdot \nabla(u_h^n + u_h^{n-1}) v_h \; dx \\ &\quad + \sum_{K \in \mathcal{T}_h} \tau_K \int_K \left(\frac{u_h^n - u_h^{n-1}}{\tau_n} + \frac{1}{2} \, a \cdot \nabla(u_h^n + u_h^{n-1}) \right) (a \cdot \nabla v_h) \; dx \\ &\quad = \frac{1}{2} \int_\Omega (f^n + f^{n-1}) v_h \; dx + \sum_{K \in \mathcal{T}_h} \tau_K \int_K \frac{1}{2} (f^n + f^{n-1})(a \cdot \nabla v_h) \; dx, \end{aligned} \tag{2.3}$$

for all $n = 1, \ldots, N$. The stabilization parameter τ_K is defined by

$$\tau_K = \frac{\lambda_{2,K}}{2|a|_\infty} \xi(Pe_K),$$

where $|a|_\infty = \|a\|_{L^\infty(\bar{\Omega}\times[0,T])}$ and the function ξ is defined by

$$\xi(Pe_K) = \begin{cases} Pe_K & \text{if } 0 \le Pe_K \le 1, \\ 1 & \text{if } 1 \le Pe_K, \end{cases} \tag{2.4}$$

with Pe_K, the local Péclet number, defined by

$$Pe_K = \frac{\lambda_{2,K}|a|_\infty}{6\epsilon}.$$

Here $\lambda_{2,K}$ is the local mesh size in the direction of minimum stretching defined by (1.8). Using the notations (1.4) of the previous Chapter and introducing the continuous, piecewise linear approximation in time $u_{h\tau}$ defined for all $t \in I_n$ by (1.6), we can rewrite (2.3) as

$$\begin{aligned} &\int_\Omega \partial_n u_h \; v_h \; dx + \epsilon \int_\Omega \nabla u_{h\tau} \cdot \nabla v_h \; dx + \int_\Omega a \cdot \nabla u_{h\tau} \; v_h \; dx \\ &\quad + \sum_{K \in \mathcal{T}_h} \tau_K \int_K \left(\partial_n u_h + a \cdot \nabla u_h^{n-1/2} \right) (a \cdot \nabla v_h) \; dx \\ &= \epsilon \; (t - t^{n-1/2}) \int_\Omega (\nabla \partial_n u_h \cdot \nabla v_h \; dx + a \cdot \nabla \partial_n u_h \; v_h \; dx) \\ &\quad + \int_\Omega f^{n-1/2} v_h \; dx + \sum_{K \in \mathcal{T}_h} \tau_K \int_K f^{n-1/2} (a \cdot \nabla v_h) \; dx, \end{aligned} \tag{2.5}$$

for all $v_h \in V_h^0$.

2.3 An upper bound for the error

In order to derive an a posteriori error estimate involving the three-point reconstruction $\widetilde{u}_{h\tau}$ (1.13), we first need the following result.

Proposition 2.3.1. *Set for all $t \in I_n$, $2 \le n \le N$,*

$$\bar{f} = f^{n-1/2} + (t - t^{n-1/2}) \frac{f^n - f^{n-2}}{\tau_n + \tau_{n-1}} \quad \textit{and} \quad \bar{u}_{h\tau} = u_h^{n-1/2} + (t - t^{n-1/2}) \frac{u_h^n - u_h^{n-2}}{\tau_n + \tau_{n-1}}.$$

Let $\widetilde{u}_{h\tau}$ be defined by (1.13) then for all $v_h \in V_h^0$ and for all $t \in I_n$, $2 \leq n \leq N$, we have

$$\begin{aligned}
&\int_\Omega \frac{\partial \widetilde{u}_{h\tau}}{\partial t} v_h \, dx + \epsilon \int_\Omega \nabla u_{h\tau} \cdot \nabla v_h \, dx + \int_\Omega a \cdot \nabla u_{h\tau} \, v_h \, dx \\
&= \frac{\tau_{n-1}}{2}(t - t^{n-1/2}) \int_\Omega \left(\epsilon \nabla \partial_n^2 u_h \cdot \nabla v_h + a \cdot \nabla \partial_n^2 u_h \, v_h \right) dx \\
&+ \int_\Omega \bar{f} v_h \, dx + \sum_{K \in \mathcal{T}_h} \tau_K \int_K \left(\bar{f} - \frac{\partial \widetilde{u}_{h\tau}}{\partial t} - a \cdot \nabla \bar{u}_{h\tau} \right) (a \cdot \nabla v_h) \, dx.
\end{aligned}$$

Proof. Let $2 \leq n \leq N$ and $t \in I_n$. From (1.13), recall that

$$\frac{\partial \widetilde{u}_{h\tau}}{\partial t} = \partial_n u_h + (t - t^{n-1/2}) \partial_n^2 u_h.$$

Thus, using (2.5), we have for all $v_h \in V_h^0$

$$\begin{aligned}
&\int_\Omega \frac{\partial \widetilde{u}_{h\tau}}{\partial t} v_h \, dx + \epsilon \int_\Omega \nabla u_{h\tau} \cdot \nabla v_h \, dx + \int_\Omega a \cdot \nabla u_{h\tau} \, v_h \, dx \\
&+ \sum_{K \in \mathcal{T}_h} \tau_K \int_K \left(\partial_n u_h + a \cdot \nabla u_h^{n-1/2} - f^{n-1/2} \right) a \cdot \nabla v_h \, dx \\
&= (t - t^{n-1/2}) \int_\Omega \left\{ \partial_n^2 u_h \, v_h + \epsilon \nabla \partial_n u_h \cdot \nabla v_h + a \cdot \nabla \partial_n u_h \, v_h \right\} dx \\
&\qquad + \int_\Omega f^{n-1/2} v_h \, dx. \qquad (2.6)
\end{aligned}$$

We now search for an alternative expression of the first term in the right hand side of (2.6). We take the difference between equation (2.3) at time t^n and t^{n-1} to obtain

$$\begin{aligned}
&\int_\Omega \partial_n^2 u_h \, v_h \, dx + \epsilon \int_\Omega \nabla \left(\frac{u_h^n - u_h^{n-2}}{\tau_n + \tau_{n-1}} \right) \cdot \nabla v_h \, dx + \int_\Omega a \cdot \nabla \left(\frac{u_h^n - u_h^{n-2}}{\tau_n + \tau_{n-1}} \right) \, v_h \, dx \\
&+ \sum_{K \in \mathcal{T}_h} \tau_K \int_K \left(\partial_n^2 u_h + a \cdot \nabla \left(\frac{u_h^n - u_h^{n-2}}{\tau_n + \tau_{n-1}} \right) - \frac{f^n - f^{n-2}}{\tau_n + \tau_{n-1}} \right) (a \cdot \nabla v_h) \, dx \\
&= \int_\Omega \frac{f^n - f^{n-2}}{\tau_n + \tau_{n-1}} v_h \, dx.
\end{aligned}$$

Thus, as

$$\partial_n u_h - \frac{u_h^n - u_h^{n-2}}{\tau_n + \tau_{n-1}} = \frac{\tau_{n-1}}{2} \, \partial_n^2 u_h,$$

we have

$$\begin{aligned}
&\int_\Omega \left\{\partial_n^2 u_h\ v_h + \epsilon\nabla\partial_n u_h\cdot\nabla v_h + a\cdot\nabla\partial_n u_h\ v_h\right\}\ dx\\
&= \frac{\tau_{n-1}}{2}\int_\Omega \left(\epsilon\nabla\partial_n^2 u_h\cdot\nabla v_h + a\cdot\nabla\partial_n^2 u_h\ v_h\right)\ dx + \int_\Omega\left(\frac{f^n - f^{n-2}}{\tau_n+\tau_{n-1}}\right)v_h\ dx\\
&+\sum_{K\in\mathcal{T}_h}\tau_K\int_K\left(\left(\frac{f^n-f^{n-2}}{\tau_n+\tau_{n-1}}\right) - \partial_n^2 u_h - a\cdot\nabla\left(\frac{u_h^n - u_h^{n-2}}{\tau_n+\tau_{n-1}}\right)\right)\left(a\cdot\nabla v_h\right)\ dx.
\end{aligned} \tag{2.7}$$

It suffices now to insert (2.7) in (2.6) to obtain the desired result. □

The Theorem presented hereafter is the main theoretical result of this Chapter. In what follows we recall that $e = u - u_{h\tau}$ and $\widetilde{e} = u - \widetilde{u}_{h\tau}$.

Theorem 2.3.2. *Let $\bar{f}$ and $\bar{u}_{h\tau}$ be defined as in Proposition 2.3.1. Assume that the mesh is such that there exists c independent of the time step, mesh size, aspect ratio, ϵ, a, f and u^0 such that*

$$\lambda_{1,K}^2\left(r_{1,K}^T G_K(\widetilde{e}) r_{1,K}\right) \le c\lambda_{2,K}^2\left(r_{2,K}^T G_K(\widetilde{e}) r_{2,K}\right) \quad \forall K\in\mathcal{T}_h. \tag{2.8}$$

Then, there exists C independent of the time step, mesh size, aspect ratio, ϵ, a, f and u^0 such that

$$\begin{aligned}
&\int_{t^1}^T \|\nabla e\|_{L^2(\Omega)}^2\,dt + \frac{1}{\epsilon}\|e(\cdot,T)\|_{L^2(\Omega)}^2 \le \frac{1}{\epsilon}\left\|e(\cdot,t^1)\right\|_{L^2(\Omega)}^2 + \ C\sum_{n=2}^N\sum_{K\in\mathcal{T}_h}\Bigg\{\\
&\int_{t^{n-1}}^{t^n}\left(\left\|\frac{1}{\epsilon}\left(f - \frac{\partial\widetilde{u}_{h\tau}}{\partial t} - a\cdot\nabla u_{h\tau}\right) + \Delta u_{h\tau}\right\|_{L^2(K)} + \frac{1}{2\lambda_{2,K}^{1/2}}\left\|\left[\frac{\partial u_{h\tau}}{\partial\mathbf{n}}\right]\right\|_{L^2(\partial K)}\right)\\
&\qquad\times\left(\lambda_{1,K}^2\left(r_{1,K}^T G_K(\widetilde{e}) r_{1,K}\right) + \lambda_{2,K}^2\left(r_{2,K}^T G_K(\widetilde{e}) r_{2,K}\right)\right)^{1/2} dt\\
&+\left(\frac{\tau_{n-1}^2\tau_n^3}{48} + \frac{\tau_n^5}{120}\right)\left(\left\|\nabla\partial_n^2 u_h\right\|_{L^2(K)}^2 + \frac{|a|_\infty^2}{\epsilon^2}\left\|\partial_n^2 u_h\right\|_{L^2(K)}^2\right) + \int_{t^{n-1}}^{t^n}\left\|\frac{1}{\epsilon}\left(f-\bar{f}\right)\right\|_{L^2(K)}^2 dt\\
&\qquad+\frac{|a|_\infty^2\lambda_{2,K}^4}{\epsilon^2}\int_{t^{n-1}}^{t^n}\left\|\frac{1}{\epsilon}\left(\bar{f} - \frac{\partial\widetilde{u}_{h\tau}}{\partial t} - a\cdot\nabla\bar{u}_{h\tau}\right)\right\|_{L^2(K)}^2 dt\Bigg\}.
\end{aligned} \tag{2.9}$$

$[\cdot]$ denotes the jump of the bracketed quantity across an internal edge with the convention that $[\cdot] = 0$ for an edge on the boundary $\partial\Omega$, and $\mathbf{n}$ is the unit edge normal (in arbitrary direction).

Remark 2.3.3. *The estimate in Theorem 2.3.2 is not a usual a posteriori error estimation since $\widetilde{e} = u - \widetilde{u}_{h\tau}$, and hence the gradient of u, is still involved in the right-hand side of the estimate. An efficient manner to approximate this quantity was proposed in [30, 29] by introducing a Zienkiewicz-Zhu post-processing procedure. This was also been done to derive the a posteriori space error estimator in the previous Chapter, see Section 1.4.3.*

Remark 2.3.4. *Condition (2.8) with $c = 1$ will be enforced by our adaptive algorithm as in the previous Chapter, see Section 1.5.*

Remark 2.3.5. *In the case of isotropic meshes $\lambda_{1,K} \simeq \lambda_{2,K} \simeq h_K$, then the above a posteriori error estimate becomes*

$$\int_{t^1}^{T} \|\nabla e\|^2_{L^2(\Omega)}\, dt + \frac{1}{\epsilon}\|e(\cdot,T)\|^2_{L^2(\Omega)} \leq \frac{1}{\epsilon}\left\|e(\cdot,t^1)\right\|^2_{L^2(\Omega)} + \; C\sum_{n=2}^{N}\sum_{K\in\mathcal{T}_h}\Bigg\{$$

$$\int_{t^{n-1}}^{t^n}\left(h_K^2\left\|\frac{1}{\epsilon}\left(f - \frac{\partial\widetilde{u}_{h\tau}}{\partial t} - a\cdot\nabla u_{h\tau}\right) + \Delta u_{h\tau}\right\|^2_{L^2(K)} + h_K\left\|\left[\frac{\partial u_{h\tau}}{\partial \mathbf{n}}\right]\right\|^2_{L^2(\partial K)}\right) dt$$

$$+\left(\frac{\tau_{n-1}^2\tau_n^3}{48} + \frac{\tau_n^5}{120}\right)\left(\left\|\nabla\partial_n^2 u_h\right\|^2_{L^2(K)} + \frac{|a|^2_\infty}{\epsilon^2}\left\|\partial_n^2 u_h\right\|^2_{L^2(K)}\right) + \int_{t^{n-1}}^{t^n}\left\|\frac{1}{\epsilon}\left(f - \bar{f}\right)\right\|^2_{L^2(K)} dt$$

$$+\frac{|a|^2_\infty h_K^4}{\epsilon^2}\int_{t^{n-1}}^{t^n}\left\|\frac{1}{\epsilon}\left(\bar{f} - \frac{\partial\widetilde{u}_{h\tau}}{\partial t} - a\cdot\nabla\bar{u}_{h\tau}\right)\right\|^2_{L^2(K)} dt\Bigg\}$$

without having to assume (2.8) but with a constant C depending on the mesh aspect ratio.

Remark 2.3.6. *We will use the terms in the second and third lines of* (2.9) *in order to estimate the error due to space discretization and the terms in the fourth line of* (2.9) *in order to estimate the error due to time discretization. The term in the fifth line of* (2.9) *will be disregarded since it is of higher order.*

Proof. Let $2 \leq n \leq N$ and $t \in I_n$. Using (2.2), (1.13) and Proposition 2.3.1, we obtain for all $v \in H_0^1(\Omega)$ and all $v_h \in V_h^0$

$$
\begin{aligned}
&\frac{1}{\epsilon}\int_\Omega \frac{\partial \widetilde{e}}{\partial t} v \; dx + \int_\Omega \nabla e \cdot \nabla v \; dx + \frac{1}{\epsilon}\int_\Omega a \cdot \nabla \widetilde{e} \; v \; dx \\
&= \frac{1}{\epsilon}\int_\Omega \left(f - \frac{\partial \widetilde{u}_{h\tau}}{\partial t} \right) v \; dx - \int_\Omega \nabla u_{h\tau} \cdot \nabla v \; dx - \frac{1}{\epsilon}\int_\Omega a \cdot \nabla \widetilde{u}_{h\tau} \; v \; dx \\
&= \frac{1}{\epsilon}\int_\Omega \left(f - \frac{\partial \widetilde{u}_{h\tau}}{\partial t} \right) (v - v_h) \; dx - \int_\Omega \nabla u_{h\tau} \cdot \nabla (v - v_h) \; dx \\
&\quad - \frac{1}{\epsilon}\int_\Omega a \cdot \nabla u_{h\tau} \; (v - v_h) \; dx - \frac{1}{2\epsilon}(t - t^{n-1})(t - t^n) \int_\Omega a \cdot \nabla \partial_n^2 u_h \; v \; dx \\
&\quad - \frac{\tau_{n-1}}{2}(t - t^{n-1/2}) \int_\Omega \left(\nabla \partial_n^2 u_h \cdot \nabla v_h + \frac{1}{\epsilon} \; a \cdot \nabla \partial_n^2 u_h \; v_h \right) \; dx \\
&\quad + \frac{1}{\epsilon}\int_\Omega (f - \bar{f}) \; v_h \; dx - \frac{1}{\epsilon} \sum_{K \in \mathcal{T}_h} \tau_K \int_K \left(\bar{f} - \frac{\partial \widetilde{u}_{h\tau}}{\partial t} - a \cdot \nabla \bar{u}_{h\tau} \right) (a \cdot \nabla v_h) \; dx.
\end{aligned}
$$

Note that since a is an incompressible field, we have for all $v \in H_0^1(\Omega)$

$$\int_\Omega a \cdot \nabla v \; v \; dx = 0.$$

Then taking $v = \widetilde{e}$, $v_h = I_h \widetilde{e}$ and integrating by parts, we obtain

$$
\begin{aligned}
&\frac{1}{2\epsilon}\frac{d}{dt}\int_\Omega |\widetilde{e}|^2 \; dx + \int_\Omega \nabla e \cdot \nabla \widetilde{e} \; dx = \\
&\quad \sum_{K \in \mathcal{T}_h} \left\{ \int_K \left\{ \frac{1}{\epsilon} \left(f - \frac{\partial \widetilde{u}_{h\tau}}{\partial t} - a \cdot \nabla u_{h\tau} \right) + \Delta u_{h\tau} \right\} (\widetilde{e} - I_h \widetilde{e}) \; dx \right. \\
&\quad \left. + \frac{1}{2}\int_{\partial K} \left[\frac{\partial u_{h\tau}}{\partial \mathbf{n}} \right] (\widetilde{e} - I_h \widetilde{e}) \; dx \right\} + \frac{1}{2\epsilon}(t - t^{n-1})(t - t^n) \int_\Omega a \cdot \nabla \widetilde{e} \; \partial_n^2 u_h \; dx \\
&\quad - \frac{\tau_{n-1}}{2}(t - t^{n-1/2}) \int_\Omega \left(\nabla \partial_n^2 u_h \cdot \nabla I_h \widetilde{e} - \frac{1}{\epsilon} \; a \cdot \nabla I_h \widetilde{e} \; \partial_n^2 u_h \right) \; dx \\
&\quad + \int_\Omega \frac{1}{\epsilon} \left(f - \bar{f} \right) \; I_h \widetilde{e} \; dx - \sum_{K \in \mathcal{T}_h} \tau_K \int_K \frac{1}{\epsilon} \left(\bar{f} - \frac{\partial \widetilde{u}_{h\tau}}{\partial t} - a \cdot \nabla \bar{u}_{h\tau} \right) (a \cdot \nabla I_h \widetilde{e}) \; dx.
\end{aligned}
$$

Using the fact that $ab = \frac{1}{2}a^2 + \frac{1}{2}b^2 - \frac{1}{2}(a-b)^2$ and $ab \leq \frac{1}{2p}a^2 + \frac{p}{2}b^2 \ \forall p \in \mathbb{R}^+$, Proposition 1.3.1, the Cauchy-Schwarz and the Poincaré inequality, and recall that from (1.13) we have

$$\begin{aligned}\|\nabla(e-\widetilde{e})\|^2_{L^2(K)} &= \|\nabla(\widetilde{u}_{h\tau} - u_{h\tau})\|^2_{L^2(K)} \\ &= \frac{1}{4}(t-t^{n-1})^2(t-t^n)^2 \left\|\nabla\partial_n^2 u_h\right\|^2_{L^2(K)},\end{aligned}$$

then

$$\begin{aligned}&\frac{1}{2\epsilon}\frac{d}{dt}\int_\Omega |\widetilde{e}|^2\,dx + \frac{1}{2}\int_\Omega |\nabla e|^2\,dx + \frac{1}{2}\int_\Omega |\nabla\widetilde{e}|^2\,dx \ \leq \qquad (2.10)\\
&\sum_{K\in\mathcal{T}_h}\left\{C_1\left(\left\|\frac{1}{\epsilon}\left(f - \frac{\partial\widetilde{u}_{h\tau}}{\partial t} - a\cdot\nabla u_{h\tau}\right) + \Delta u_{h\tau}\right\|_{L^2(K)} + \frac{1}{2\lambda_{2,K}^{1/2}}\left\|\left[\frac{\partial u_{h\tau}}{\partial \mathbf{n}}\right]\right\|_{L^2(\partial K)}\right)\right.\\
&\quad\times\left(\lambda^2_{1,K}\left(r^T_{1,K}G_K(\widetilde{e})r_{1,K}\right) + \lambda^2_{2,K}\left(r^T_{2,K}G_K(\widetilde{e})r_{2,K}\right)\right)^{1/2}\\
&\quad+\left\{\frac{p\ \tau^2_{n-1}}{8}(t-t^{n-1/2})^2 + \frac{1}{8}(t-t^{n-1})^2(t-t^n)^2\right\}\left\|\nabla\partial_n^2 u_h\right\|^2_{L^2(K)}\\
&\quad+\frac{p\ |a|^2_\infty}{8\epsilon^2}\left\{(t-t^{n-1})^2(t-t^n)^2 + \tau^2_{n-1}(t-t^{n-1/2})^2\right\}\left\|\partial_n^2 u_h\right\|^2_{L^2(K)}\\
&\quad+\frac{p}{2}\left\|\frac{1}{\epsilon}\left(f-\bar{f}\right)\right\|^2_{L^2(K)} + \frac{p\ |a|^2_\infty\tau_K^2}{2}\left\|\frac{1}{\epsilon}\left(\bar{f} - \frac{\partial\widetilde{u}_{h\tau}}{\partial t} - a\cdot\nabla\bar{u}_{h\tau}\right)\right\|^2_{L^2(K)}\\
&\quad\left.+\frac{1}{2p}\left\|\nabla\widetilde{e}\right\|^2_{L^2(K)} + \frac{3+C_2^2}{2p}\left\|\nabla I_h\widetilde{e}\right\|^2_{L^2(K)}\right\},\end{aligned}$$

where C_1 is the constant of Proposition 1.3.1 and C_2 is the constant in the Poincaré inequality. Error equidistribution inequality (2.8) combined with Proposition 1.3.1 implies that

$$\omega_K(\widetilde{e}) \leq C_3\lambda_{2,K}\left\|\nabla\widetilde{e}\right\|_{L^2(K)} \quad \text{and thus} \quad \left\|\nabla I_h\widetilde{e}\right\|_{L^2(K)} \leq C_4\left\|\nabla\widetilde{e}\right\|_{L^2(K)}. \qquad (2.11)$$

Finally, use the second inequality of (2.11) in (2.10), the inequality $\tau_K \leq \frac{\lambda^2_{2,K}}{12\epsilon}$, choose $p = 1 + C_4^2(3+C_2^2)$ and integrate (2.10) between $t = t^{n-1}$ and $t = t^n$, to obtain

$$\int_{t^{n-1}}^{t^n} \|\nabla e\|^2_{L^2(\Omega)}\,dt + \frac{1}{\epsilon}\,\|\widetilde{e}(\cdot,t^n)\|^2_{L^2(\Omega)} \le \frac{1}{\epsilon}\,\|\widetilde{e}(\cdot,t^{n-1})\|^2_{L^2(\Omega)} + \; C\sum_{K\in\mathcal{T}_h}\Bigg\{$$

$$\int_{t^{n-1}}^{t^n}\left(\left\|\frac{1}{\epsilon}\left(f-\frac{\partial\widetilde{u}_{h\tau}}{\partial t}-a\cdot\nabla u_{h\tau}\right)+\Delta u_{h\tau}\right\|_{L^2(K)}+\frac{1}{2\lambda_{2,K}^{1/2}}\left\|\left[\frac{\partial u_{h\tau}}{\partial\mathbf{n}}\right]\right\|_{L^2(\partial K)}\right)$$

$$\times\left(\lambda_{1,K}^2\left(r_{1,K}^T G_K(\widetilde{e})r_{1,K}\right)+\lambda_{2,K}^2\left(r_{2,K}^T G_K(\widetilde{e})r_{2,K}\right)\right)^{1/2}dt$$

$$+\left(\frac{\tau_{n-1}^2\tau_n^3}{48}+\frac{\tau_n^5}{120}\right)\left(\left\|\nabla\partial_n^2 u_h\right\|^2_{L^2(K)}+\frac{|a|^2_\infty}{\epsilon^2}\left\|\partial_n^2 u_h\right\|^2_{L^2(K)}\right)+\int_{t^{n-1}}^{t^n}\left\|\frac{1}{\epsilon}\left(f-\bar{f}\right)\right\|^2_{L^2(K)}dt$$

$$+\frac{|a|^2_\infty\lambda_{2,K}^4}{\epsilon^2}\int_{t^{n-1}}^{t^n}\left\|\frac{1}{\epsilon}\left(\bar{f}-\frac{\partial\widetilde{u}_{h\tau}}{\partial t}-a\cdot\nabla\bar{u}_{h\tau}\right)\right\|^2_{L^2(K)}dt\Bigg\},$$

where $C=\max(1,2C_1,p)$. Summing up these inequalities on n and noting that $\widetilde{e}(t^n)=e(t^n)\ \forall n$, leads to the final result. □

2.3.1 An anisotropic error indicator

Since the a posteriori error estimate of Theorem 2.3.2 involves the exact solution u we proceed as in Section 1.4.3. Therefore, we introduce the Zienkiewicz-Zhu error estimator $\eta^{ZZ}(u_{h\tau})$ defined by (1.25). Our error indicator is then obtained by replacing $G_K(\widetilde{e})$ in $\omega_K(\widetilde{e})$ by $\check{G}_K(u_{h\tau})$ defined for any $v_h\in V_h$ by (1.27). Approximating in such a way $G_K(\widetilde{e})$ in Theorem 2.3.2 and considering Remark 2.3.6, we define the anisotropic space error estimator η^A as

$$\eta^A=\left(\sum_{n=1}^{N}\sum_{K\in\mathcal{T}_h}\left(\eta^A_{K,n}(u_{h\tau})\right)^2\right)^{1/2},$$

where the contributions $\eta^A_{K,n}$ are defined on each triangle K of $\mathcal{T}_h$ and each time interval I_n by

$$\left(\eta^A_{K,n}(u_{h\tau})\right)^2=$$

$$\int_{t^{n-1}}^{t^n}\left(\left\|\frac{1}{\epsilon}\left(f-\frac{\partial\widetilde{u}_{h\tau}}{\partial t}-a\cdot\nabla u_{h\tau}\right)+\Delta u_{h\tau}\right\|_{L^2(K)}+\frac{1}{2\lambda_{2,K}^{1/2}}\left\|\left[\frac{\partial u_{h\tau}}{\partial\mathbf{n}}\right]\right\|_{L^2(\partial K)}\right)$$

$$\times\left(\lambda_{1,K}^2\left(r_{1,K}^T\check{G}_K(u_{h\tau})r_{1,K}\right)+\lambda_{2,K}^2\left(r_{2,K}^T\check{G}_K(u_{h\tau})r_{2,K}\right)\right)^{1/2}dt,$$

and the time error estimator $\widetilde{\eta}^T$ as

$$\widetilde{\eta}^T = \left(\sum_{n=2}^{N} \sum_{K \in \mathcal{T}_h} \left(\widetilde{\eta}_{K,n}^T(u_{h\tau}) \right)^2 \right)^{1/2},$$

where the contributions $\widetilde{\eta}_{K,n}^T$ are computed on each triangle K of $\mathcal{T}_h$ and each time interval I_n by

$$\left(\widetilde{\eta}_{K,n}^T(u_{h\tau}) \right)^2 = \left(\frac{\tau_{n-1}^2 \tau_n^3}{48} + \frac{\tau_n^5}{120} \right) \left(\left\| \nabla \partial_n^2 u_h \right\|_{L^2(K)}^2 + \frac{|a|_\infty^2}{\epsilon^2} \left\| \partial_n^2 u_h \right\|_{L^2(K)}^2 \right) + \int_{t^{n-1}}^{t^n} \left\| \frac{1}{\epsilon} \left(f - \bar{f} \right) \right\|_{L^2(K)}^2 dt, \quad \text{for } n \geq 2. \tag{2.12}$$

Note that in our implementation, all the integrals between t^{n-1} and t^n are approximated by the midpoint rule. As in Section 1.4.3, we introduce the corresponding effectivity indices in space and time, ei^A and $\widetilde{ei}^T$, respectively defined by (1.32) and (1.33). We also check the behavior of the global Zienkiewicz-Zhu error estimator η^{ZZ} defined by (1.34) and recall that the corresponding effectivity index ei^{ZZ} is defined by (1.35).

2.4 Adaptive algorithm in space and time

The adaptive algorithm is similar to that presented in Section 1.5. The goal is to build successive anisotropic triangulations $\mathcal{T}_h^n$ and choose appropriate time steps τ_n so that the relative error estimated in space and time in the $L^2(0,T;H^1(\Omega))$ norm is close to a preset tolerance TOL. Here we suggest that

$$0.75 \text{ TOL} \leq \frac{\left((\eta^A)^2 + (\widetilde{\eta}^T)^2 \right)^{1/2}}{\left(\displaystyle\int_0^T \int_\Omega |\nabla u_{h\tau}|^2 \, dx \, dt \right)^{1/2}} \leq 1.25 \text{ TOL}.$$

Note that since the time error estimator (2.12) needs a solution u_h^{n-2}, we do not attempt to change the first time step. Thus, sufficient conditions to satisfy the

above inequality is that, for all $n \geq 1$, the error indicator in space is such that

$$\frac{3}{4}\, 0.75^2\ \mathrm{TOL}^2 \int_{t^{n-1}}^{t^n} \int_\Omega |\nabla u_{h\tau}|^2\ dx\ dt\ \leq \sum_{K \in \mathcal{T}_h} \left(\eta^A_{K,n}(u_{h\tau})\right)^2 \leq \frac{3}{4}\, 1.25^2\ \mathrm{TOL}^2 \int_{t^{n-1}}^{t^n} \int_\Omega |\nabla u_{h\tau}|^2\ dx\ dt, \tag{2.13}$$

and, for all $n \geq 2$, the error indicator in time is such that

$$\frac{1}{4}\, 0.75^2\ \mathrm{TOL}^2 \int_{t^{n-1}}^{t^n} \int_\Omega |\nabla u_{h\tau}|^2\ dx\ dt\ \leq \sum_{K \in \mathcal{T}_h} \left(\widetilde{\eta}^T_{K,n}(u_{h\tau})\right)^2 \leq \frac{1}{4}\, 1.25^2\ \mathrm{TOL}^2 \int_{t^{n-1}}^{t^n} \int_\Omega |\nabla u_{h\tau}|^2\ dx\ dt. \tag{2.14}$$

We refer to Section 1.5 for the adaptive procedure where conditions (1.37) and (1.38) must be replaced by the present conditions (2.13) and (2.14). Moreover, we decide not to make the space and time adaptation at the same time. We first carry out the space adaptation before the time adaptation if both conditions (2.13) and (2.14) are not satisfied.

Remark 2.4.1. *In conditions (1.37) and (1.38), we chose to put the same weight on the space and time error indicators in our adaptive algorithm. Here we decide to weight the space error condition (2.13) by 3/4 and the time error condition (2.14) by 1/4.*

Remark 2.4.2. *The two coefficients 0.75 and 1.25 define the interval of tolerance for which the relative error estimated is acceptable. Choosing these coefficients close to one would yield to error indicators close to TOL but conditions (2.13) and (2.14) would become more restrictive and would lead to many remeshings and time step modifications. In the case of the time-dependent convection-diffusion problem, we choose to enlarge this interval of tolerance.*

Remark 2.4.3. *Here we do not take into account the interpolation error between two successive meshes. We postulate that this interpolation error can be neglected provided the total number of remeshings does not depend on the prescribed tolerance TOL. This has been successfully satisfied in the previous Chapter and will be observed in the forthcoming numerical results.*

2.5 Numerical experiments

We apply here our adaptive algorithm to several test cases. We monitor at final time T, the absolute error ϵ_{abs} in $L^2(0,T;H^1(\Omega))$ norm defined by (1.41), the relative error ϵ_{rel} in the same norm defined by (1.42), the number of nodes nb_n, maximum and mean aspect ratio, ar and $\overline{ar}$, respectively defined by (1.43) and (1.44). We also report the number of time steps nb_τ required to reach the final time and the number of remeshings nb_m occurred. We follow Section 1.6 and do all the computations by replacing ∇u_h^{n-1} by its Zienkiewicz-Zhu recovery, $\Pi_h^n\left(\nabla u_h^{n-1}\right)$, when $\mathcal{T}_h^{n-1} = \mathcal{T}_h^n$ and ∇u_h^{n-1} by $\Pi_h^n\left(\nabla r_h^n(u_h^{n-1})\right)$ when $\mathcal{T}_h^{n-1} \neq \mathcal{T}_h^n$ where Π_h^n is an approximate $L^2(\Omega)$ projection onto V_h^n defined by (1.26). In the following, we study three examples, 2.5.1 and 2.5.2, taken from [69], and conclude with the numerical simulation of an electroosmotic flow in a long rectangular channel.

Example 2.5.1 We first consider a problem for which an analytical solution is known. Thus, we consider the convection-diffusion of a small source in a plane shear flow. We set $\Omega = (-4000, 26000) \times (-3400, 3400)$, $T = 9000$, $\epsilon = 50$, $f = 0$ and $a = (a_0 + \lambda y, 0)^T$ where $a_0 = 0.5$ and $\lambda = 1e-3$. The initial condition u_0 is a point source of mass m at $(x_0, y_0) = (7200, 0)$. Then the solution of (2.1) is given by

$$u(x,y,t) = \frac{m}{4\pi\epsilon t(1+\lambda^2 t^2/12)^{1/2}} \exp^{-\chi},$$

where

$$\chi = \frac{(x-\bar{x}-\lambda y t/2)^2}{4\epsilon t(1+\lambda^2 t^2/12)} + \frac{y^2}{4\epsilon t} \quad \text{and} \quad \bar{x} = x_0 + a_0 t.$$

To allow the numerical solution of this problem to begin with a finite source size, the computation is started at a time $t = t_0 = 2400$ with

$$m = 4\pi\epsilon t_0(1+\lambda^2 t_0^2/12)^{1/2}.$$

We present in Figure 2.1 the adapted meshes for a tolerance TOL=0.0625. In Figure 2.2 we present a history of the number of nodes and of the time step size against time. We see that the number of nodes is quite constant whereas the time step increases as the solution getting more diffused.

To investigate the efficiency of our adaptive algorithm, we provide in Table 2.1 (top) numerical experiments with several values of tolerance TOL. The result show that ei^{ZZ} gets close to one when TOL tends to zero and that the space and time error estimator are equivalent to the true error as their effectivity indices tend to a constant value. We note that the error is divided by two each time the

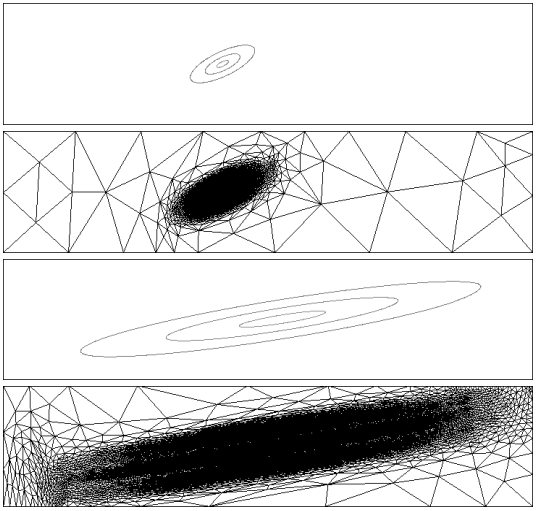

Figure 2.1. *Example 2.5.1. Adapted meshes and isovalues obtained with a tolerance TOL=0.0625. Top: time t=2450, isovalues 0.1, 0.5, 0.9, with 6421 nodes. Bottom: final time* $T = 9000$*, isovalues 0.01, 0.05, 0.1, with 8884 nodes.*

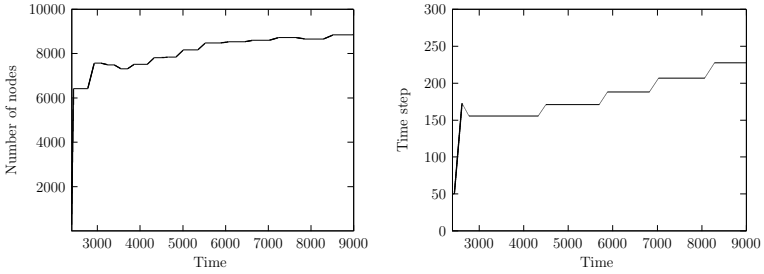

Figure 2.2. *Example 2.5.1. Number of nodes (left) and time step size (right) with respect to time t with a tolerance TOL=0.0625.*

TOL	ϵ_{rel}	ϵ_{abs}	ei^{ZZ}	ei^{A}	$\widetilde{ei}^{T}$	nb_n	nb_τ	nb_m	$\overline{ar}$	ar
0.25	0.110	9.750	0.762	2.131	1.162	1134	22	20	5.2	27.8
0.125	0.0504	4.475	0.882	2.451	1.072	2714	27	21	7.3	48.7
0.0625	0.0250	2.218	0.903	2.469	1.154	8884	37	26	9.5	69.4
0.03125	0.0121	1.073	0.915	2.482	1.137	32664	52	29	10.1	88.4
0.25	0.116	10.092	0.574	1.93	0.939	1679	159	44	6.6	48.5
0.125	0.0551	4.856	0.689	2.082	0.978	3728	206	48	9.7	48.6
0.0625	0.0265	2.344	0.767	2.193	1.082	11990	281	55	9.9	93.2
0.03125	0.0129	1.144	0.837	2.279	1.163	40525	400	59	10.6	74.2

Table 2.1. *Example 2.5.1. True error and effectivity indices of the adapted solution at final time $T = 9000$. Top: $\epsilon = 50$. Bottom: $\epsilon = 1$.*

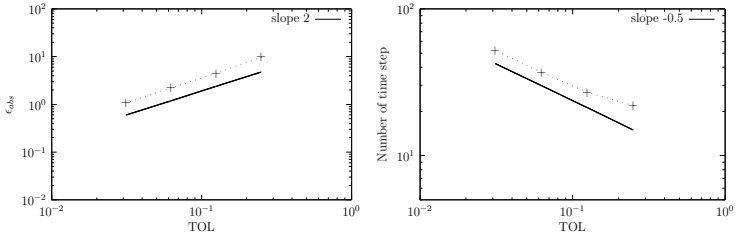

Figure 2.3. *Example 2.5.1. True error (left) and total number of time steps (right) at final time $T = 9000$ with respect to the tolerance TOL ($\epsilon = 50$).*

tolerance is and that the optimal second order of convergence with respect to time is achieved as the number of time steps is multiplied by $\sqrt{2}$ when TOL is divided by two, see also Figure 2.3. We study now the behavior of the same quantities for a smaller diffusion coefficient. We have reported the results in Table 2.1 (bottom) with a diffusion coefficient $\epsilon = 1$. We can observe that the error is still divided by two each time the tolerance is and that the optimal rate of convergence with respect to time is also recovered. The differences concern the Zienkiewicz-Zhu error estimator and the number of nodes and time steps. Indeed, we observe that when the diffusion coefficient gets smaller ei^{ZZ} is not close to one anymore when TOL tends to zero. Regarding the number of nodes and time steps it increase as ϵ decreases which is not surprising according to our space and time indicators.

Example 2.5.2 In this example we consider a more anisotropic finite elements test case exhibiting both internal and boundary layers. We set $\Omega = (0,1)^2$, $f = 0$, $T = 0.6$, $\epsilon = 1e-3$, $a = (2,1)^T$, $\delta = 7.8125e-3$. The initial condition $u^0 = 0$ except on $\partial\Omega$ where u^0 is defined by

$$u^0(x,y) = \begin{cases} 1 & \text{if } x = 0, 0 \le y \le 1, \\ 1 & \text{if } 0 \le x \le 1, y = 1, \\ (\delta - x)/\delta & \text{if } x \le \delta, y = 0, \\ 0 & \text{if } x > \delta, y = 0, \\ (y - 1 + \delta)/\delta & \text{if } x = 1, y \ge 1 - \delta, \\ 0 & \text{if } x = 1, y \le 1 - \delta, \end{cases}$$

see also Figure 2.4. Note that we keep the same boundary conditions for the computation of the numerical solution.

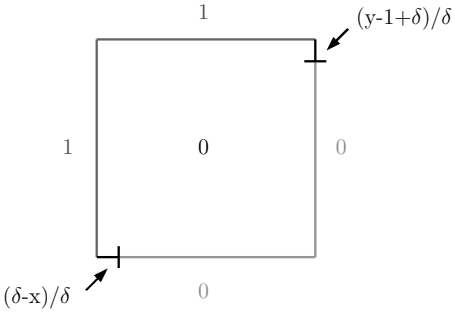

Figure 2.4. *Example 2.5.2. Initial condition* u^0.

Thus, this problem exhibits boundary layers along $x = 0$ and $y = 1$ at initial time. The boundary layer at $x = 0$ propagates into the domain and creates an internal boundary layer which finally reaches the boundary at $x = 1$ and creates a new boundary layer because of the imposed $u = 0$ boundary condition. The boundary layer at $y = 1$ reduces progressively as the solution gets the value of one on the top of the domain. Thus this problem exhibits both internal and boundary layers which make it a very challenging problem. Adapted meshes are presented in Figure 2.6 for a tolerance TOL=0.0625. In Figure 2.5 we present a history of the number of nodes and of the time step size against time. We see that the number of nodes, initially large due to the discontinuous boundary condition, decreases as

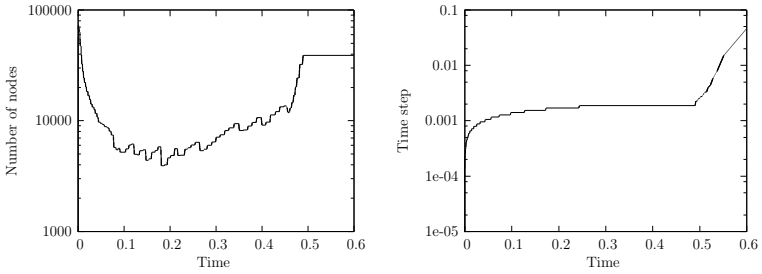

Figure 2.5. *Example 2.5.2. Number of nodes (left) and time step size (right) with respect to time t with a tolerance TOL=0.0625.*

the internal layer propagates into the domain and then increases with the development of a new boundary layer at the external boundary until finally becoming constant. For the time step size, we see that it was initially very small in order to capture the very large gradient of the solution. Then, progressively it increases as the solution gets more diffused. Moreover, we observe that near the time $t = 0.5$ the solution reaches its stationary point. At this moment, the number of nodes stays constant and the time step increases quickly.

We have reported in Table 2.2 the total number of time steps required to reach the final time for several values of tolerance TOL. We observe that the optimal second order of convergence with respect to time is recovered as the number of time steps is multiplied by $\sqrt{2}$ when TOL is divided by two, see also Figure 2.7. Finally, in Figures 2.8 and 2.9 we present several zooms of the meshes of the numerical simulation reported in Figure 2.6. In Figure 2.8 we zoom on the left bottom corner and the right top corner of the domain respectively at the time $t = 0.25$ (left pictures) and at final time $T = 0.6$ (right pictures). In Figure 2.9 we present a progressive zoom of the external boundary layer created by the discontinuity of the solution due to the imposed zero value condition on this part of the boundary at final time $T = 0.6$.

Example 2.5.3 In this example we study the dynamics of a solute carried by an electroosmotic flow within a rectangular microchannel. All the parameters are given in the international unit system. The solute is initially modelled by a rectangular unit pulse. Thus, we set $\Omega = (0, 6e-4) \times (0, 5e-5)$, $\epsilon = 1e-10$,

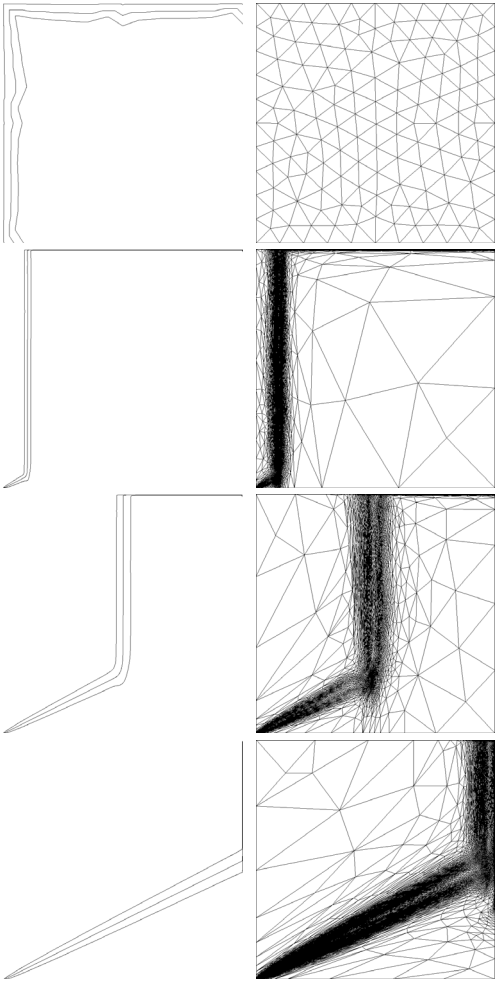

Figure 2.6. *Example 2.5.2. Adapted meshes (right) and isovalues 0.1, 0.5, 0.9 (left) obtained with a tolerance TOL=0.0625. From top to bottom: time t=0, 0.05, 0.25 and 0.6 (151, 9464, 6050 and 38874 nodes, respectively).*

TOL	nb_n	nb_τ	nb_m	$\overline{ar}$	ar
0.25	3987	163	93	15.0	190.9
0.125	12222	247	103	17.9	769.7
0.0625	38874	353	109	21.6	2553.8
0.03125	140057	502	130	27.9	9092.1

Table 2.2. *Example 2.5.2. Number of nodes and time steps of the adapted solution at final time $T = 0.6$.*

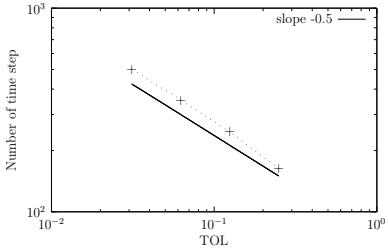

Figure 2.7. *Example 2.5.2. Total number of time steps at final time $T = 0.6$ with respect to the tolerance TOL.*

$f = 0$, $T = 0.1$. The initial condition u^0 is defined by

$$u^0(x,y) = \begin{cases} 0.5 + 0.5\tanh\left(\dfrac{x - 1e-4}{1e-6}\right) & \text{if } x < 1.5e-4, \\ 0.5 - 0.5\tanh\left(\dfrac{x - 2e-4}{1e-6}\right) & \text{if } x > 1.5e-4. \end{cases}$$

Note that we consider here a mixed Dirichlet-Neumann boundary condition problem. Indeed, we impose $u = 0$ along the left and right sides and homogeneous Neumann boundary condition on the top and bottom sides. In the case of a narrow rectangular microchannel with uniformly charged walls and an imposed constant electric field E along the x-direction such as $E = (E_x, 0)^T$, the velocity field is horizontal and can be approximated, if the zeta potential at the walls is

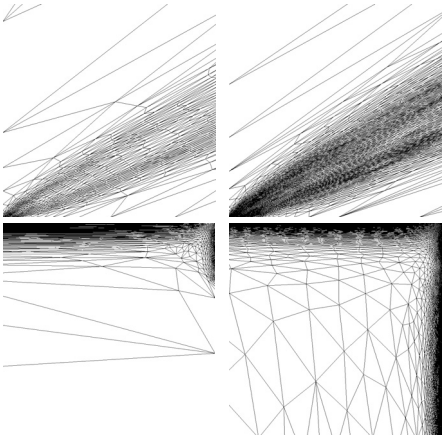

Figure 2.8. *Example 2.5.2. Zoom on adapted meshes of the left bottom corner and the right top corner of the domain respectively at the time* $t = 0.25$ *(left pictures) and at final time* $T = 0.6$ *(right pictures).*

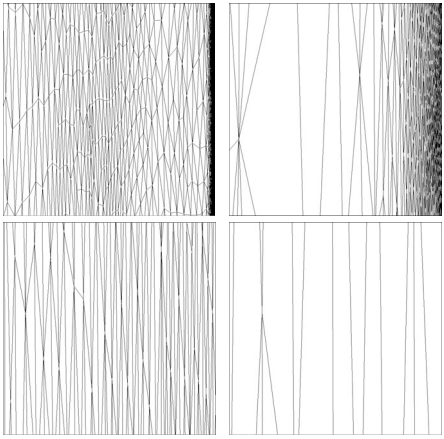

Figure 2.9. *Example 2.5.2. From left to right, top to bottom: zoom of size 1e-1, 1e-2, 1e-3 and 1e-4 of the external boundary layer at x=1 at final time* $T = 0.6$.

such that $|\zeta| < 0.25$ [8], by

$$a(x,y) = \begin{pmatrix} -\dfrac{\bar{\epsilon}\zeta E_x}{4\pi\mu}(1-\exp(-\kappa g(y))) \\ 0 \end{pmatrix},$$

where $\bar{\epsilon} = 6.95e-10$ is the electrical permittivity of the solution, $\zeta = -0.1$, $\mu = 1e-3$ is the viscosity, $g(y)$ is the normal distance of the wall, $E_x = 5e5$ and κ^{-1} is called the Debye length and it corresponds to the thickness of the Debye layer. Thus the velocity profile is horizontal, equal to zero on the top and bottom sides of the domain, constant in the whole domain except in the Debye layer region very close to the wall. In Figure 2.10 we plot the velocity profile against the normal distance to the wall for various values of κ^{-1}. Note that the Debye thickness (κ^{-1}) is usually of the order 10^{-9}, which will be the value that we will use in our numerical simulations. We can refer to [70, 71] for the all set of equations describing the electroosmotic flow in the general case and [8, 72] in the case of rectangular microchannels. The numerical simulations are presented in Figure 2.11 for a tolerance TOL=0.0625.

In Figure 2.12 we present the evolution of the number of nodes and of the time step size against time. Here again, the time step size increases with the diffusion of the solution. The number of nodes increases too as the solution gets diffused.

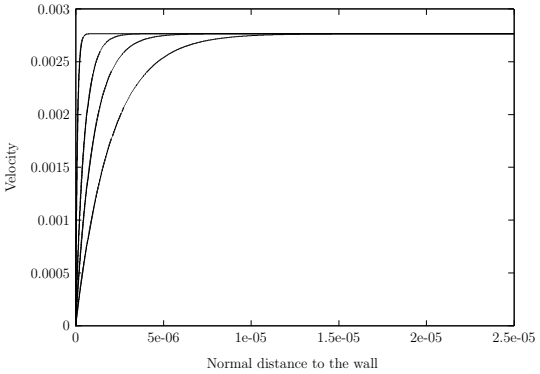

Figure 2.10. *Example 2.5.3. Velocity profiles for various values of* κ^{-1}*. From left to right:* $\kappa^{-1} = 1e-7, 5e-7, 1e-6, 2e-6$.

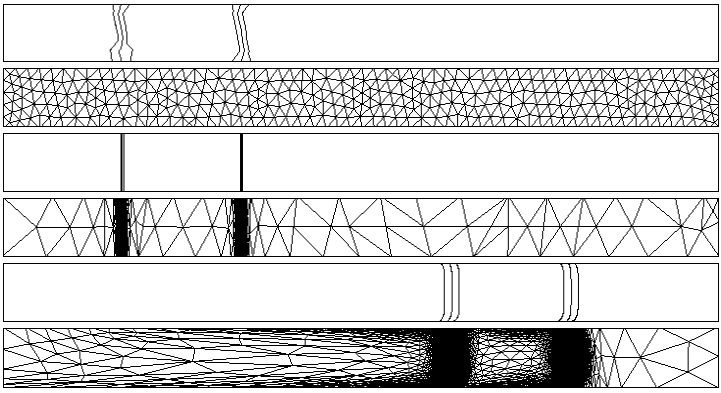

Figure 2.11. *Example 2.5.3. Adapted meshes and isovalues 0.1, 0.5 and 0.9 obtained with a tolerance TOL=0.0625. From top to bottom: time t=0, 0.0001, and 0.1 (401, 10663 and 34443 nodes, respectively).*

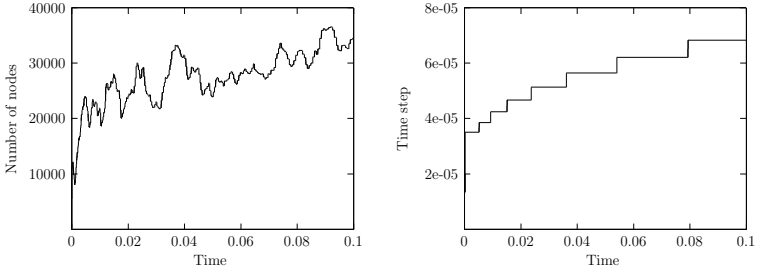

Figure 2.12. *Example 2.5.3. Number of nodes (left) and time step size (right) with respect to time t with a tolerance TOL=0.0625.*

In Table 2.3 we have reported the total number of time steps required to reach the final time for several values of tolerance TOL. We still observe the optimal second order of convergence with respect to the time step, see also Figure 2.13. Finally, in Figure 2.14, we zoom on the solute at final time $T = 0.1$ for all the four tolerances of Table 2.3.

TOL	nb_n	nb_τ	nb_m	$\overline{ar}$	ar
0.25	10700	864	173	4.5	62.1
0.125	16201	1272	240	5.3	49.7
0.0625	34443	1842	290	5.4	63.2
0.03125	60059	2626	316	5.9	78.3

Table 2.3. *Example 2.5.3. Number of nodes and time steps of the adapted solution at final time* $T = 0.1$.

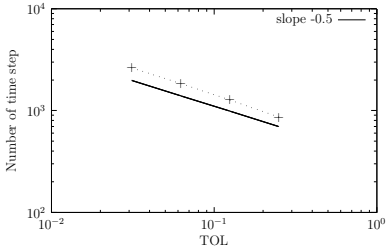

Figure 2.13. *Example 2.5.3. Total number of time steps at final time* $T = 0.1$ *with respect to the tolerance TOL.*

2.6 Conclusion

An anisotropic error estimator for the time-dependent convection-diffusion problem using the second order Crank-Nicolson scheme has been derived. The corresponding space and time error estimators have been successfully used in a space and time adaptive algorithm. All the numerical experiments show optimal order with respect to both the mesh size and time step and demonstrate that these indicators provide an efficient tool for the computation of unsteady convection-diffusion problem exhibiting sharp boundary layers. Based on these error indicators, we now focus on the numerical simulation of EOF and mass transport of a sample concentration within a network of microchannels.

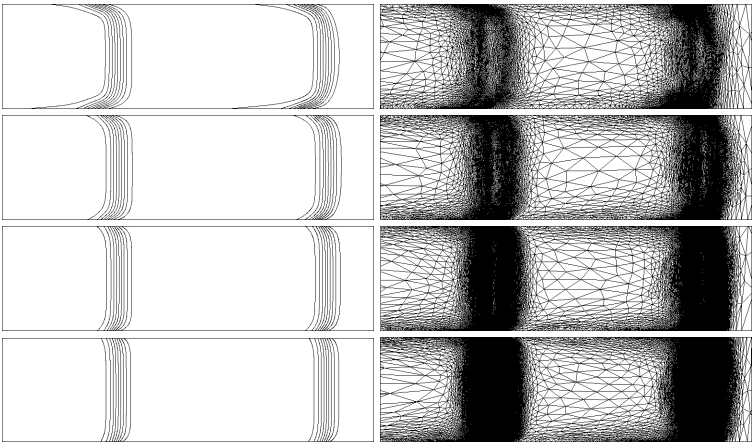

Figure 2.14. *Example 2.5.3. Adapted meshes and isovalues 0.1 to 0.9 at final time* $T = 0.1$. *From top to bottom: tolerance TOL=0.25, 0.125, 0.0625, 0.03125 (10700, 16201, 34443, 60059 nodes, respectively).*

Chapter 3

Adaptive finite elements with large aspect ratio for electroosmosis and pressure-driven microflows

A space and time adaptive method with possibly finite elements having large aspect ratio are presented for the numerical simulation of mixed electroosmotic and pressure-driven microflows in two space dimensions. The method allows the electroosmotic flow to be solved accurately, despite the presence of strong boundary layers. The unknowns are the external electric potential, the electrical double layer potential, the velocity field and the sample concentration. Continuous piecewise linear stabilized finite elements with large aspect ratio and the Crank-Nicolson scheme are used for the space and time discretization of the concentration equation. Numerical results are presented showing the efficiency of this approach, first in a straight channel, then in a crossing, double and multiple T-form configuration channel.

Contents

3.1 Situation

Due to the recent development of various micro-system devices for fluid handling and analysis, EOF has received much attention over the last decade. It has been widely investigated as well experimentally, theoretically or numerically [8, 73, 6]. Patankar and Hu [70] carried out three-dimensional numerical simulations of EOF in a cross-channel device using a finite volume method. Bianchi et al. [74] studied EOF in T-junctions and the influence of the ζ-potential distribution and the Reynolds number on the flow distribution using a finite element formulation. Numerical simulations of microfluidics injection have been done by Ren et al. [75] who used artificial boundary conditions in order to truncate the physical domain to a smaller one. Ermakov et al. [76, 77] investigated mass transport and EOF in two-dimensional channels. Injection techniques were also simulated. Electrokinetic injection techniques within complex geometries have been also widely studied by Fu et al. [78, 79] who made simulations in a cross-shaped, double-T and triple-T shaped configuration system. Mixed electroosmotic and pressure-driven flows in straight channel and T-shaped junction have been studied by Dutta et al. [80] using a spectral element method. Dutta and Beskok also presented in [81] analytical results of combined electroosmotic and pressure-driven flows in a two-dimensional straight channel. Optimization of the design of microchannel turns to minimize electrokinetic dispersion of analyte bands is carried out in [82, 83] using adaptive finite elements.

The aim of the Chapter is to simulate the behavior of EOF and mass transport in complex geometries. The key issue is to compute accurately and efficiently the electric potential near the walls. As the thickness of the EDL is very thin ($\sim$ nm) compared to the capillary diameter ($\sim \mu$m), the estimation of this potential is a challenging task when considering its numerical simulation. A novel approach will be used. An adaptive finite element method will be considered. This method will allow to automatically refine the mesh grid in the EDL region and thus capture accurately and efficiently the variation of the electric wall potential. Instead of assuming a slip electroosmotic condition at the walls, avoiding the computation of the EDL potential, we will be able to fully solve the EDL near the capillary walls. Moreover this approach will allow to follow accurately the transport of a sample solution through the capillary channels. The use of finite elements with large aspect ratio is then well suited to the strong boundary layers which are present in such problem. Thus based on error estimators developed in the previous Chapter for the time-dependent convection-diffusion problem, a space and time adaptive algorithm with large aspect ratio finite elements will be used to study the mass transport of a sample solution. The refinement/coarsening criterion will also be based on error estimators already presented for parabolic problems [29] and the

Stokes problem [33].

The outline is the following. Section 3.2 covers the model consisting of the two electric potentials, the EOF and the sample concentration. The numerical method is described in Section 3.3. It is based on a finite element method and a posteriori error estimators presented in [33, 29, 35]. In Section 3.4 the numerical validation of the EOF in a straight channel is presented. Finally in Section 3.5, we present numerical simulations of injection and separation in a crossing, double and multiple T-form configuration channel.

3.2 The model

Numerical simulations of EOF in a slit microchannel require a thorough understanding of microscale electrokinetic phenomena. One of the most important appears at the solid-liquid interface. Because most channel walls have an electrostatic charge, in contact with an ionic solution, an electric field is created near the walls. This plays an important role in microchannel transport processes and is at the base of EOF. In the following, we present the mathematical model describing the EOF and the mass transport of a sample solution in a rectangular domain $\Omega = (0, L) \times (0, H) \in \mathbb{R}^2$ with boundary $\partial\Omega = \Gamma_{\text{in}} \cup \Gamma_{\text{out}} \cup \Gamma_{\text{wall}}$, see Figure 3.1. However, the model can be extended to any geometry Ω, see the results of Section 3.5. The mathematical model considered here is taken from [8, 80]. For the sake of clarity, we briefly summarize the set of equations describing the EOF.

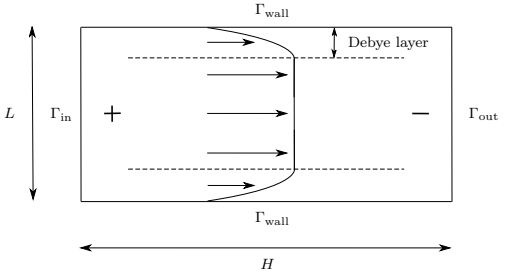

Figure 3.1. *Schematic representation of EOF in a straight channel in the situation of negatively charged walls.*

3.2.1 External electric potential and electrical double layer potential

The distribution of the overall electric potential can be divided into two potentials. One due to the EDL at the channel surface, and the other due to the external applied electric field. In contact with an ionic solution, the channel walls acquire a certain potential due to the wall charge. This potential is called the ζ-potential. When the thickness of the EDL is small and the ζ-potential is not large, the distribution of the charge species near the walls is mainly governed by the ζ-potential and is not affected by the external electric potential [84, 73]. Thus these two potentials can be determined independently and the distribution of the overall electric potential can be decomposed into the potential ϕ due to the external electric field and the potential ψ due to the charge of the wall. The potential ϕ satisfies,

$$\begin{cases} \Delta\phi &= 0 & \text{in } \Omega, \\ \phi &= \phi_{\text{in}} & \text{on } \Gamma_{\text{in}}, \\ \phi &= \phi_{\text{out}} & \text{on } \Gamma_{\text{out}}, \\ \partial_{\mathbf{n}}\phi &= 0 & \text{on } \Gamma_{\text{wall}}, \end{cases} \tag{3.1}$$

where $\phi_{\text{in}}, \phi_{\text{out}} \in \mathbb{R}$ are constant potentials with the choice that $\phi_{\text{in}} > \phi_{\text{out}}$. According to electrostatic theory, the relationship between the electric potential, ψ, and the net charge density per unit volume, ρ_e, is described by the Poisson equation,

$$\Delta\psi = -\frac{\rho_e}{\epsilon_r \epsilon_0}, \tag{3.2}$$

where ϵ_r is the dielectric constant of the solution, ϵ_0 is the permittivity of the vacuum and ρ_e is given by

$$\rho_e = -2n_0 ze \sinh\left(\frac{ze\psi}{\kappa_b T_a}\right), \tag{3.3}$$

where n_0 is the bulk ionic concentration, z is the ion valence, e is the elementary charge, T_a is the absolute temperature and κ_b is the Boltzmann constant. Substituting (3.3) in (3.2) leads to the well-known Poisson-Boltzmann equation,

$$\begin{cases} \Delta\psi &= \dfrac{2n_0 ze}{\epsilon_r \epsilon_0} \sinh\left(\dfrac{ze\psi}{\kappa_b T_a}\right) & \text{in } \Omega, \\ \psi &= \zeta & \text{on } \Gamma_{\text{wall}}, \\ \partial_{\mathbf{n}}\psi &= 0 & \text{on } \Gamma_{\text{in}} \cup \Gamma_{\text{out}}, \end{cases} \tag{3.4}$$

where $\zeta \in \mathbb{R}$ is the wall potential.

3.2.2 Electroosmotic flow and sample concentration

A characteristic of microfluidics is the laminar nature of the flow. Due to the small dimensions of the microchannels, the Reynolds number is usually less than 1 and the flow is laminar, no turbulence occurs. Thus the EOF is governed by the Stokes equation with a body force term including the effect between the excess ions of the EDL and the external electric field. Thus the fluid flow can be considered as a steady state problem and the velocity and pressure field satisfy

$$\begin{cases} -\mu\Delta u + \nabla p &= \rho_e E \quad \text{in } \Omega, \\ \text{div } u &= 0 \quad \text{in } \Omega, \end{cases} \tag{3.5}$$

where u is the velocity vector, p the pressure, μ the viscosity and E is the external electric field related to the external electric potential ϕ such that

$$E = -\nabla\phi. \tag{3.6}$$

Substituting (3.3) and (3.6) in (3.5) leads to the electroosmotic flow problem

$$\begin{cases} -\mu\Delta u + \nabla p &= 2n_0 ze \sinh\left(\dfrac{ze\psi}{\kappa_b T_a}\right)\nabla\phi \quad \text{in } \Omega, \\ \text{div } u &= 0 \quad \text{in } \Omega, \\ u &= 0 \quad \text{on } \Gamma_{\text{wall}}, \\ -p + \mu\partial_{\mathbf{n}} u \cdot \mathbf{n} &= 0 \quad \text{on } \Gamma_{\text{in}} \cup \Gamma_{\text{out}}, \\ u \cdot t &= 0 \quad \text{on } \Gamma_{\text{in}} \cup \Gamma_{\text{out}}, \end{cases} \tag{3.7}$$

where t is a unit tangential vector normal to n. Given a final time $T > 0$, the mass transport equation for the study of the sample concentration solution is the classical convection-diffusion equation,

$$\begin{cases} \dfrac{\partial c}{\partial t} - \epsilon\Delta c + u \cdot \nabla c &= 0 \quad \text{in } \Omega \times (0,T), \\ \partial_{\mathbf{n}} c &= 0 \quad \text{on } \partial\Omega \times (0,T), \\ c(\cdot,0) &= c^0 \quad \text{in } \Omega, \end{cases} \tag{3.8}$$

where c is the sample concentration, c^0 is the concentration initial condition, u is given by (3.7) and ϵ is the diffusion coefficient.

3.2.3 Summary of the model

To solve the electroosmotic transport of a sample concentration field within a microchannel, we first have to determine the EOF. For this purpose, the two electric

potentials ϕ and ψ have to be computed by solving problems (3.1) and (3.4). These two potentials are then used in the right hand side of the Stokes problem (3.7) to solve the electroosmotic velocity, u, and pressure, p. The concentration field c is finally given by (3.8) with the electroosmotic velocity field given by (3.7). Please note that only c depends on time, thus ϕ, ψ, u and p could be in principle computed once for all before computing the evolution of c. However, since adapted meshes will be generated in order to compute the concentration field c with precision, ϕ, ψ, u and p have to be recomputed each time remeshing occurs.

3.3 Numerical method

The sample concentration problem is discretized in time using a Crank-Nicolson scheme. Space discretization is based on continuous piecewise linear finite elements. Stabilization terms have to be added to the weak formulations, see for instance [85] for the Stokes problem and [66] for the convection-diffusion problem. Moreover, note that problem (3.4) exhibits a nonlinear term. In order to treat this nonlinearity, a Newton iteration strategy will be used to solve the EDL potential ψ. Since boundary layers are expected, an adaptive finite element method with triangles having large aspect ratio will be used. The refinement/coarsening criterion is based on a posteriori error estimates already presented in the previous Chapter and in [33, 29, 35].

3.3.1 The finite element method

The finite element is now described for a fixed mesh. Since the formulation of the two electric potentials is quite standard, we can refer to classical finite element textbooks, see for instance [86, 87, 88]. For the sake of clarity, we briefly present their weak formulations.

The discretized problem (3.1) consists in finding $\phi_h \in V_h$ such that $\phi_h = r_h\phi_{\text{in}}$ on Γ_{in}, $\phi_h = r_h\phi_{\text{out}}$ on Γ_{out} and

$$\int_\Omega \nabla\phi_h \cdot \nabla v_h \, dx = 0 \quad \forall v_h \in V_h.$$

As the problem (3.4) presents a nonlinear term, the EDL potential ψ is solved using a Newton algorithm which takes the following form:

$$\Delta\psi^{k+1} - \kappa^2 \cosh\left(\omega\psi^k\right)\psi^{k+1} = \beta \sinh\left(\omega\psi^k\right) - \kappa^2 \cosh\left(\omega\psi^k\right)\psi^k,$$

where k is the iteration number, the two constants β and ω are respectively defined by

$$\beta = \frac{2zen_0}{\epsilon_r\epsilon_0} \quad \text{and} \quad \omega = \frac{ze}{\kappa_b T_a}, \tag{3.9}$$

and κ^{-1} is called the Debye length and corresponds to the thickness of the EDL such that

$$\kappa = \sqrt{\frac{2z^2e^2n_0}{\epsilon_r\epsilon_0\kappa_b T_a}}. \tag{3.10}$$

Thus, the corresponding finite element method consists in seeking $\psi_h^{k+1} \in V_h$ such that $\psi_h^{k+1} = r_h\zeta$ on Γ_{wall} and

$$\int_\Omega \nabla\psi_h^{k+1}\cdot\nabla v_h\ dx + \int_\Omega \kappa^2\cosh\left(\omega\psi_h^k\right)\psi_h^{k+1}v_h\ dx = \int_\Omega \kappa^2\cosh\left(\omega\psi_h^k\right)\psi_h^k\ v_h\ dx - \int_\Omega \beta\sinh\left(\omega\psi_h^k\right)v_h\ dx \quad \forall v_h \in V_h.$$

The latter equation is then solved until the discrepancy $\|\psi_h^{k+1}-\psi_h^k\|^2_{L^2(\Omega)}$ is smaller than a preset tolerance (typically 10^{-9}).

Then let ϕ_h and ψ_h be respectively the finite element solutions belonging to V_h of the two electric potential problems (3.1) and (3.4). We are now looking for the solution of the steady Stokes problem (3.7). Referring to [50, 33], the stabilized finite element method for the Stokes problem consists in finding the velocity $u_h \in V_h \times V_h$ and the pressure $p_h \in V_h$ such that $u_h = 0$ on Γ_{wall}, $u_h\cdot t = 0$ on $\Gamma_{\text{in}}\cup\Gamma_{\text{out}}$ and such that

$$\begin{aligned}\int_\Omega \mu\nabla u_h\cdot\nabla v_h\ dx - \int_\Omega p_h\ \text{div}(v_h)\ dx - \int_\Omega \text{div}(u_h)\ q_h\ dx \\ - \sum_{K\in\mathcal{T}_h}\frac{\alpha\lambda_{2,K}^2}{\mu}\int_K \nabla p_h\cdot\nabla q_h\ dx = \int_\Omega 2n_0ze\sinh\left(\frac{ze\psi_h}{\kappa_b T_a}\right)\nabla\phi_h\ v_h\ dx \\ - \sum_{K\in\mathcal{T}_h}\alpha\lambda_{2,K}^2\int_K 2n_0ze\sinh\left(\frac{ze\psi_h}{\kappa_b T_a}\right)\nabla\phi_h\cdot\nabla q_h\ dx,\end{aligned} \tag{3.11}$$

for all test functions $v_h \in V_h \times V_h$ and $q_h \in V_h$ such that $v_h = 0$ on Γ_{wall} and $v_h\cdot t = 0$ on $\Gamma_{\text{in}}\cup\Gamma_{\text{out}}$. Here $\alpha > 0$ is a dimensionless stabilization parameter to be suitably chosen and $\lambda_{2,K}$ is the local mesh size in the direction of minimum stretching defined by (1.8).

For the sake of clarity we briefly recall the discretization of the time-dependent convection-diffusion problem (3.8). We keep the same notations as in Section 2.2.

Then, considering the Crank-Nicolson time discretization scheme, the stabilized finite element method for the sample concentration problem consists in finding $c_h^n \in V_h$ such that $\forall v_h \in V_h$,

$$\int_\Omega \frac{c_h^n - c_h^{n-1}}{\tau_n} v_h \, dx + \frac{\epsilon}{2} \int_\Omega \nabla(c_h^n + c_h^{n-1}) \cdot \nabla v_h \, dx + \frac{1}{2} \int_\Omega u_h \cdot \nabla(c_h^n + c_h^{n-1}) v_h \, dx + \sum_{K \in \mathcal{T}_h} \tau_K \int_K \left(\frac{c_h^n - c_h^{n-1}}{\tau_n} + \frac{1}{2} \, u_h \cdot \nabla(c_h^n + c_h^{n-1}) \right) (u_h \cdot \nabla v_h) \, dx = 0,$$

where the stabilization parameter τ_K is defined by

$$\tau_K = \frac{\lambda_{2,K}}{2|u_h|_\infty} \xi(Pe_K),$$

where $|u_h|_\infty = \|u_h\|_{L^\infty(K)}$, the function ξ is defined by (2.4) and Pe_K, the local Péclet number, is defined by

$$Pe_K = \frac{\lambda_{2,K}|u_h|_\infty}{6\epsilon}.$$

3.3.2 A posteriori error estimators

A space and time adaptive algorithm will be presented to compute the sample concentration field c. Since the EOF is considered at a stationary state, ϕ_h, ψ_h, u_h and p_h could be computed only once and interpolated from mesh to mesh, each time a new mesh is generated. However, the interpolated error would be too large and the accuracy would not be guaranteed. Thus, each time a new mesh is built, ϕ_h, ψ_h, u_h and p_h have to be recomputed on this new mesh. Moreover, to ensure optimal accuracy of the electroosmotic velocity field, the error estimator used in the space adaptive algorithm has to take into account not only the concentration field but also the velocity and potential fields. Thus, the space adaptive algorithm will couple three error estimators derived from the EDL potential problem (3.4), the Stokes problem (3.7) and the convection-diffusion problem (3.8). The mesh grid will then be refined near the walls where the EDL potential ψ drops from the ζ-potential at the capillary walls to zero through the Debye Layer. Despite the very thin thickness of the Debye Layer, the adapted mesh will then enable us to capture the strong variation of the EDL potential and thus provide an optimal accuracy of the EOF. The error estimators have been already justified theoretically in the previous Chapter for the time-dependent convection-diffusion problem, for parabolic problems in [29, 35] and for the Stokes problem in [33].

Considering the convection-diffusion problem, we now introduce the continuous, piecewise linear approximation in time $c_{h\tau}$ defined for all $t \in I_n$ by

$$c_{h\tau}(x,t) = \frac{t-t^{n-1}}{\tau_n} c_h^n + \frac{t^n - t}{\tau_n} c_h^{n-1},$$

and $\widetilde{c}_{h\tau}$ the three-point quadratic time reconstruction defined for all $t \in I_n$, $2 \leq n \leq N$, by

$$\widetilde{c}_{h\tau}(x,t) = c_{h\tau}(x,t) + \frac{1}{2}(t-t^{n-1})(t-t^n)\partial_n^2 c_h,$$

where

$$\partial_n^2 c_h = \frac{\dfrac{c_h^n - c_h^{n-1}}{\tau_n} - \dfrac{c_h^{n-1} - c_h^{n-2}}{\tau_{n-1}}}{(\tau_n + \tau_{n-1})/2}.$$

Then, following the previous Chapter and [33, 29, 35], we introduce the anisotropic concentration space error estimator $\eta^{A,c}$, the anisotropic Stokes space error estimator, $\eta^{A,u}$, and the anisotropic EDL space error estimator, $\eta^{A,\psi}$, respectively defined by

$$\begin{aligned}
\eta^{A,c} &= \left(\sum_{n=1}^{N} \sum_{K \in \mathcal{T}_h} \left(\eta_{K,n}^{A,c}(c_{h\tau}) \right)^2 \right)^{1/2}, \\
\eta^{A,u} &= \left(\sum_{K \in \mathcal{T}_h} \left(\eta_{K}^{A,u}(u_h) \right)^2 \right)^{1/2}, \\
\eta^{A,\psi} &= \left(\sum_{K \in \mathcal{T}_h} \left(\eta_{K}^{A,\psi}(\psi_h) \right)^2 \right)^{1/2},
\end{aligned}$$

where the contributions $\eta_{K,n}^{A,c}$ are defined on each triangle K of $\mathcal{T}_h$ and each time interval I_n by

$$\begin{aligned}
\left(\eta_{K,n}^{A,c}(c_{h\tau}) \right)^2 = \int_{t^{n-1}}^{t^n} \left(\left\| \frac{1}{\epsilon} \left(\frac{\partial \widetilde{c}_{h\tau}}{\partial t} + u_h \cdot \nabla c_{h\tau} \right) \right\|_{L^2(K)} + \frac{1}{2\lambda_{2,K}^{1/2}} \left\| \left[\frac{\partial c_{h\tau}}{\partial \mathbf{n}} \right] \right\|_{L^2(\partial K)} \right) \\
\times \left(\lambda_{1,K}^2 \left(r_{1,K}^T \breve{G}_K(c_{h\tau}) r_{1,K} \right) + \lambda_{2,K}^2 \left(r_{2,K}^T \breve{G}_K(c_{h\tau}) r_{2,K} \right) \right)^{1/2} dt,
\end{aligned}$$

the contributions $\eta_K^{A,u}$ are defined on each triangle K of $\mathcal{T}_h$ by

$$\left(\eta_K^{A,u}(u_h)\right)^2 = \|\text{div } u_h\|_{L^2(K)}^2 + \left(\left\|\frac{1}{\mu}\left(\rho_e E - \nabla p_h\right)\right\|_{L^2(K)} + \frac{1}{2\lambda_{2,K}^{1/2}}\left\|\left[\frac{\partial u_h}{\partial \mathbf{n}}\right]\right\|_{L^2(\partial K)}\right) \times \left(\lambda_{1,K}^2\left(r_{1,K}^T \breve{G}_K(u_h) r_{1,K}\right) + \lambda_{2,K}^2\left(r_{2,K}^T \breve{G}_K(u_h) r_{2,K}\right)\right)^{1/2},$$

and the contributions $\eta_K^{A,\psi}$ are defined on each triangle K of $\mathcal{T}_h$ by

$$\left(\eta_K^{A,\psi}(\psi_h)\right)^2 = \left(\frac{1}{2\lambda_{2,K}^{1/2}}\left\|\left[\frac{\partial \psi_h}{\partial \mathbf{n}}\right]\right\|_{L^2(\partial K)}\right) \times \left(\lambda_{1,K}^2\left(r_{1,K}^T \breve{G}_K(\psi_h) r_{1,K}\right) + \lambda_{2,K}^2\left(r_{2,K}^T \breve{G}_K(\psi_h) r_{2,K}\right)\right)^{1/2}.$$

In all these contributions, $[\cdot]$ denotes the jump of the bracketed quantity across an internal edge with the convention $[\cdot] = 0$ for an edge on the boundary $\partial\Omega$, $\mathbf{n}$ is the unit edge normal (in arbitrary direction) and the matrix $\breve{G}_K$ is defined for any $v_h \in V_h$ by (1.27). Finally, as regards the time error estimator, it is only based on the concentration field. Thus we introduce the time error estimator $\widetilde{\eta}^{T,c}$ defined by

$$\widetilde{\eta}^{T,c} = \left(\sum_{n=2}^{N}\sum_{K\in\mathcal{T}_h}\left(\widetilde{\eta}_{K,n}^{T,c}(c_{h\tau})\right)^2\right)^{1/2},$$

where the contributions $\widetilde{\eta}_{K,n}^{T,c}$, for all $n \geq 2$, are computed on each triangle K of $\mathcal{T}_h$ and each time interval I_n by

$$\left(\widetilde{\eta}_{K,n}^{T,c}(c_{h\tau})\right)^2 = \left(\frac{\tau_{n-1}^2\tau_n^3}{48} + \frac{\tau_n^5}{120}\right)\left(\left\|\nabla\partial_n^2 c_h\right\|_{L^2(K)}^2 + \frac{|u_h|_\infty^2}{\epsilon^2}\left\|\partial_n^2 c_h\right\|_{L^2(K)}^2\right). \quad (3.12)$$

3.3.3 Adaptive algorithm

We now propose a space and time adaptive algorithm. The space adaptive algorithm will couple three anisotropic space error estimators, $\eta^{A,c}$, $\eta^{A,u}$, $\eta^{A,\psi}$ and the time adaptive algorithm is only based on the concentration time error estimator $\widetilde{\eta}^{T,c}$. This algorithm is similar to those presented in Sections 1.5 or 2.4. The goal is to build successive triangulations $\mathcal{T}_h^n$ with possibly large aspect ratio elements and choose appropriate time steps τ_n such that the concentration relative estimated error in space and time in the $L^2(0,T;H^1(\Omega))$ norm is close to a preset tolerance

TOL,

$$0.75\ \mathrm{TOL}\ \leq \frac{\left((\eta^{A,c})^2+(\widetilde{\eta}^{T,c})^2\right)^{1/2}}{\left(\displaystyle\int_0^T\int_\Omega |\nabla c_{h\tau}|^2\ dx\ dt\right)^{1/2}} \leq 1.25\ \mathrm{TOL}.$$

We also require that the Stokes and the EDL relative estimated errors in space in the $L^2(H^1(\Omega))$ norm are close to another preset tolerance $\overline{\mathrm{TOL}}$,

$$0.75\ \overline{\mathrm{TOL}}\ \leq \frac{\eta^{A,u}}{\left(\displaystyle\int_\Omega |\nabla u_h|^2\ dx\right)^{1/2}} \leq 1.25\ \overline{\mathrm{TOL}},$$

and

$$0.75\ \overline{\mathrm{TOL}}\ \leq \frac{\eta^{A,\psi}}{\left(\displaystyle\int_\Omega |\nabla \psi_h|^2\ dx\right)^{1/2}} \leq 1.25\ \overline{\mathrm{TOL}}.$$

Note that since the time error estimator (3.12) needs a solution c_h^{n-2}, we do not attempt to change the first time step. Thus, sufficient conditions to satisfy the above inequality is that, for all $n \geq 1$, the concentration error indicator in space is such that

$$\begin{aligned}\frac{3}{4}\ 0.75^2\ \mathrm{TOL}^2 \int_{t^{n-1}}^{t^n}\int_\Omega |\nabla c_{h\tau}|^2\ dx\ dt\ \leq\ & \\ \sum_{K\in\mathcal{T}_h}\left(\eta_{K,n}^{A,c}(c_{h\tau})\right)^2 & \\ \leq \frac{3}{4}\ 1.25^2\ \mathrm{TOL}^2 \int_{t^{n-1}}^{t^n}\int_\Omega |\nabla c_{h\tau}|^2\ dx\ dt, &\end{aligned} \tag{3.13}$$

for all $n \geq 2$, the concentration error indicator in time is such that

$$\begin{aligned}\frac{1}{4}\ 0.75^2\ \mathrm{TOL}^2 \int_{t^{n-1}}^{t^n}\int_\Omega |\nabla c_{h\tau}|^2\ dx\ dt\ \leq\ & \\ \sum_{K\in\mathcal{T}_h}\left(\widetilde{\eta}_{K,n}^{T,c}(c_{h\tau})\right)^2 & \\ \leq \frac{1}{4}\ 1.25^2\ \mathrm{TOL}^2 \int_{t^{n-1}}^{t^n}\int_\Omega |\nabla c_{h\tau}|^2\ dx\ dt, &\end{aligned} \tag{3.14}$$

and that the Stokes space error indicator and the EDL space error indicator satisfy respectively

$$0.75^2\ \overline{\mathrm{TOL}}^2 \int_\Omega |\nabla u_h|^2\ dx\ \leq\ \sum_{K\in\mathcal{T}_h}\left(\eta_K^{A,u}(u_h)\right)^2\ \leq\ 1.25^2\ \overline{\mathrm{TOL}}^2 \int_\Omega |\nabla u_h|^2\ dx, \tag{3.15}$$

and

$$0.75^2\ \overline{\mathrm{TOL}}^2 \int_\Omega |\nabla\psi_h|^2\ dx\ \leq\ \sum_{K\in\mathcal{T}_h} \left(\eta_K^{A,\psi}(\psi_h)\right)^2\ \leq\ 1.25^2\ \overline{\mathrm{TOL}}^2 \int_\Omega |\nabla\psi_h|^2\ dx. \tag{3.16}$$

We then proceed as Section 1.5 and build anisotropic meshes using the BL2D mesh generator software [49] considering the three conditions (3.13), (3.15) and (3.16). Thus, at each vertex, the estimated error of the concentration, Stokes and EDL are equidistributed in the two directions of maximum and minimum stretching, which yields to new appropriate values of stretching in the maximum and minimum stretching directions. Then, the desired directions of anisotropy are aligned with the direction of the eigenvectors of a matrix which takes into account the matrices of the estimated gradient error of the three above mentioned problem, which are respectively $\breve{G}_K(c_{h\tau})$, $\breve{G}_K(u_h)$ and $\breve{G}_K(\psi_h)$. Moreover, as in Section 2.4 we decide not to make the space and time adaptation at the same time. We first carry out the space adaptation before the time adaptation if conditions (3.13)-(3.16) are not satisfied. Interpolation of the concentration field between two successive meshes are carried out by the BL2D mesh generator. Here we do not take into account the interpolation error between two successive meshes provided the total number of remeshings does not depend on the prescribed tolerances TOL and $\overline{\mathrm{TOL}}$. This has been successfully satisfied in the previous Chapters and will be observed in the forthcoming numerical results.

3.4 Numerical validation of the EOF in a straight channel

In this Section, we consider the case of a straight microchannel and focus on the numerical validation of our method to solve the EOF. We derive an analytical solution for a mixed electroosmotic and pressure-driven flow in a straight channel and then study the efficiency of our adaptive algorithm taken into account only conditions (3.15) and (3.16).

3.4.1 Analytical solution in a straight channel

Let us consider a channel formed with two parallel plates. Assume that the length, L, of the channel is much larger than its height, H, then both the EDL field and the flow field can be considered as one-dimensional and thus vary only in the channel height direction, that is the y-axis. We assume that the ζ-potential is known and remains constant along the channel walls. Then the EDL potential, ψ, has an

analytical solution (see [8, 6]) given by

$$\psi = \frac{4}{\omega}\text{argth}\left[\tanh\left(\frac{\omega\zeta}{4}\right)\exp\left(-\kappa g(y)\right)\right], \tag{3.17}$$

where $g(y)$ is the normal distance to the wall and ω and κ^{-1} are respectively defined by (3.9) and (3.10). Moreover, consider a one-dimensional fully developed, steady-state flow with no-slip boundary conditions on Γ_{wall}, then the momentum equation of problem (3.5) becomes

$$-\mu\frac{\partial^2 u_x}{\partial y^2} + \frac{\partial p}{\partial x} = \rho_e E_x,$$

where u_x is the flow velocity in the x-direction and E_x is the electrokinetic potential gradient in the x-direction. Using (3.2) we obtain

$$-\mu\frac{\partial^2 u_x}{\partial y^2} + \frac{\partial p}{\partial x} + \epsilon_r\epsilon_0 E_x\frac{\partial^2\psi}{\partial y^2} = 0. \tag{3.18}$$

Then integrating (3.18) twice and using the boundary conditions for the flow field and the EDL field, we end with an analytical solution for a mixed electroosmotic and pressure-driven flow in straight microchannels, given by

$$\begin{cases} u_x(x,y) &= \dfrac{\epsilon_r\epsilon_0 E_x}{\mu}(\psi-\zeta) - \dfrac{\partial p}{\partial x}\dfrac{y}{2\mu}(H-y) & \text{in } \Omega, \\ u_y(x,y) &= 0 & \text{in } \Omega, \end{cases}$$

where ψ is given by (3.17), ζ is the known ζ-potential at the capillary walls, E_x is given by

$$E_x = \frac{\phi_{\text{in}} - \phi_{\text{out}}}{L},$$

and $\dfrac{\partial p}{\partial x}$ is the pressure gradient given by

$$\frac{\partial p}{\partial x} = -\frac{\Delta p}{L},$$

where Δp is a known pressure difference. The velocity profile in a straight channel is thus a combination of a flat profile, expressed by the term including the electrokinetic potential gradient, and a parabolic profile, the well-known Poiseuille flow, expressed by the term including the pressure gradient.

3.4.2 Numerical validation

The computational domain Ω is a rectangle $(0, 5e-4) \times (0, 5e-5)$. In order to measure the quality of the Stokes and EDL error estimators, the estimated error is compared to the true error introducing the so-called effectivity index. Thus, we define the following Stokes and EDL effectivity indices in space

$$ei^{A,u} = \frac{\eta^{A,u}}{\left(\int_\Omega |\nabla(u-u_h)|^2 \, dx\right)^{1/2}}$$

and

$$ei^{A,\psi} = \frac{\eta^{A,\psi}}{\left(\int_\Omega |\nabla(\psi-\psi_h)|^2 \, dx\right)^{1/2}}.$$

We will also check the behavior of the Zienkiewicz-Zhu error estimators corresponding to the Stokes and EDL problems. We thus introduce the corresponding error estimators and effectivity indices respectively for the Stokes and EDL problems

$$\eta^{ZZ,u} = \left(\sum_{K\in\mathcal{T}_h} \int_K |\eta^{ZZ}(u_h)|^2 \, dx\right)^{1/2}, \quad ei^{ZZ,u} = \frac{\eta^{ZZ,u}}{\left(\int_\Omega |\nabla(u-u_h)|^2 \, dx\right)^{1/2}},$$

and

$$\eta^{ZZ,\psi} = \left(\sum_{K\in\mathcal{T}_h} \int_K |\eta^{ZZ}(\psi_h)|^2 \, dx\right)^{1/2}, \quad ei^{ZZ,\psi} = \frac{\eta^{ZZ,\psi}}{\left(\int_\Omega |\nabla(\psi-\psi_h)|^2 \, dx\right)^{1/2}}.$$

Following [33, 35], we have implemented an adaptive algorithm and generate successive triangulations so that conditions (3.15) and (3.16) are satisfied. For the first numerical experiment, we decide to set the pressure difference $\Delta p = 0$ Pa, the inflow and the outflow external potential, $\phi_{\text{in}} = 5$ V and $\phi_{\text{out}} = 0$ V, and the potential at the walls $\zeta = -15$ mV. As the bulk ionic concentration n_0 is expressed in terms of the molarity M and the avogadro number N_a such that $n_0 = 1000\, N_a\, M$, we choose a molarity constant, $M = 10^{-6}$, which corresponds to a Debye thickness (see equation (3.10)) $\kappa^{-1} = 3.04 \times 10^{-7}$. Some values of κ^{-1} are reported in Table 3.1 when varying M. We assume that the buffer solution has similar properties as water and give all values of the physical parameters used in the numerical simulations in the international system of units. We reported in Table 3.2 these values.

M	κ^{-1}
10^{-8}	3.04×10^{-6}
10^{-7}	9.62×10^{-7}
10^{-6}	3.04×10^{-7}
10^{-5}	9.62×10^{-8}

Table 3.1. *Values of the Debye length when varying the molarity M of the ionic concentration.*

ϵ_0	e	k_b	n_0	N_a	T_a	ϵ_r	z	μ
8.85×10^{-12}	1.602×10^{-19}	1.381×10^{-23}	1000 N_a M	6.022×10^{23}	298	78.5	1	1e-3

Table 3.2. *Values of the physical parameters used in the numerical simulations.*

$\overline{\text{TOL}}$	ϵ^u_{rel}	ϵ^u_{abs}	$ei^{ZZ,u}$	$ei^{A,u}$	ϵ^ψ_{rel}	ϵ^ψ_{abs}	$ei^{ZZ,\psi}$	$ei^{A,\psi}$	nb_n	$\overline{ar}$	ar
0.25	0.115	5e-4	0.98	1.57	0.115	0.07	0.98	1.57	48	1887	13477
0.125	0.059	2.5e-4	0.97	1.64	0.059	0.036	0.97	1.59	79	4054	27042
0.0625	0.033	1.3e-4	0.99	1.75	0.032	0.02	0.99	1.75	128	6782	59001
0.03125	0.015	6.6e-5	0.99	1.78	0.0155	0.01	0.99	1.77	305	10935	140386

Table 3.3. *True error and effectivity indices for various values of the preset tolerance $\overline{TOL}$ of the EOF problem in a straight channel when Δp=0 Pa.*

The number of generated triangulations is 50. The numerical simulation is presented in Figure 3.2 and the numerical results are presented in Table 3.3 where we have compared the effectivity indices $ei^{A,u}$ and $ei^{ZZ,u}$ for the Stokes problem and $ei^{A,\psi}$ and $ei^{ZZ,\psi}$ for the EDL problem when varying $\overline{\text{TOL}}$. We also monitor the absolute error ϵ_{abs} in $L^2(H^1(\Omega))$ and the relative error ϵ_{rel} in the same norm for both problems with a exponent u for the Stokes problem and ψ for the EDL problem, the number of nodes nb_n, maximum and mean aspect ratio respectively defined by (1.43) and (1.44). From Table 3.3 we can observe that, first, both the Stokes and EDL errors are divided by two each time the tolerance $\overline{\text{TOL}}$ is. Second, both error estimators behave as the true error as the Stokes and EDL anisotropic effectivity indices, respectively $ei^{A,u}$ and $ei^{A,\psi}$, tend to a constant value when the mesh size tends to zero. Third, both Zienkiewicz-Zhu error estimators, respectively

$\eta^{ZZ,u}$ and $\eta^{ZZ,\psi}$, are asymptotically exact as their effectivity indices, respectively $ei^{ZZ,u}$ and $ei^{ZZ,\psi}$, tend to one when the mesh size tends to zero. These observations correspond to those reported in [33] for the Stokes problem and [29] for the Laplace problem. Thus the expected good behavior of both anisotropic error estimators $\eta^{A,u}$ and $\eta^{A,\psi}$ are verified. The adaptive algorithm used to compute the EOF provides a good agreement and can enable us to solve accurately the EDL problem and so consequently the EOF which will transport the sample solution through the capillary channels.

In Figure 3.2, we can observe that the final adapted mesh, generated after 50 iterations, is extremely refined in the EDL near the walls. This final mesh is strongly anisotropic with a mean aspect ratio of order 10^5 and only 305 nodes. A closer look on the mesh refinement is proposed in Figure 3.3 with a progressive zoom on the EDL near the bottom wall boundary of the channel. In Figure 3.4, we plot the EDL potential profile and the velocity profile against the normal distance to the wall for various values of molarity M and so consequently for various Debye lengths κ^{-1}. The velocity profile is horizontal, equal to zero at the top and bottom sides of the domain, constant in the whole domain except in the Debye layer region where the velocity drops from a constant value to zero exponentially. As expected, the EDL region gets thinner for smaller values of the Debye length.

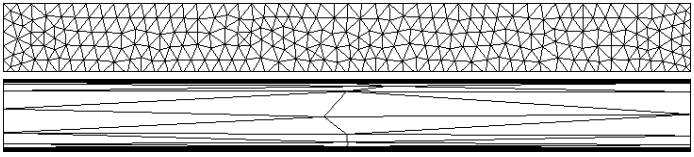

Figure 3.2. *Initial (330 nodes) and final adapted meshes (305 nodes) of the EOF problem in a straight channel ($\overline{TOL}$=0.03125, 50 mesh generations, Δp=0 Pa).*

We now impose a pressure difference Δp. The pressure value at the boundary Γ_{out} is then set to zero and we impose an inlet pressure p_{in} at Γ_{in}. This corresponds to adding an extra term to the right hand side of the finite element formulation (3.11). Numerical results of the velocity profile are presented in Figure 3.5 for different values of pressure difference. We can observe that for a positive pressure difference, the velocity profile is, as expected, a typical Poiseuille flow velocity profile. The resulting velocity is a combination of a parabolic velocity profile and a classical EOF with an uniform velocity in the bulk region, which corresponds to the case $\Delta p = 0$ Pa. For negative pressure difference, the velocity profile is a combination of a classical EOF and a reverse flow in the middle of the microchannel

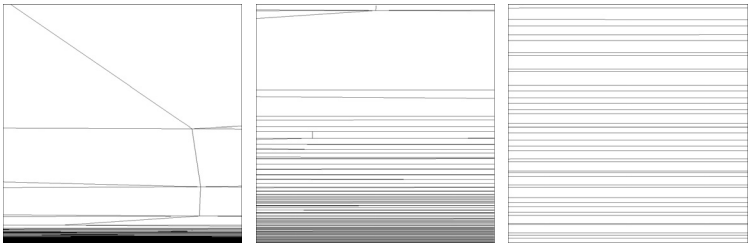

Figure 3.3. *From left to right: zoom of size 2.5e-5, 2.5e-6 and 2.5e-7 of the final mesh of the EDL near the bottom wall boundary of the channel of the EOF problem in a straight channel ($\overline{TOL}$=0.03125, 50 mesh generations, Δp=0 Pa, 305 nodes).*

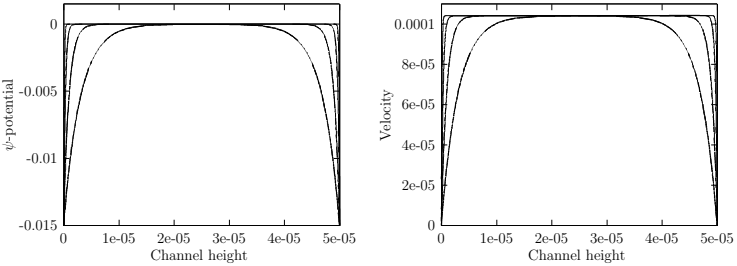

Figure 3.4. *EDL potential and velocity profiles for various values of molarity M of the EOF problem in a straight channel ($\overline{TOL}$=0.03125, 50 mesh generations, Δp=0 Pa). From the nearest to farther to the wall: $M = 10^{-5}$, 10^{-6}, 10^{-7} and 10^{-8}.*

due to the adverse applied pressure gradient. In the case of small negative pressure difference, as presented in Figure 3.5, the flow direction is still driven by the EOF but with a reduced flow rate velocity. When considering higher negative pressure difference the resulting velocity would be obviously in the opposite direction of the EOF.

We finally reproduced the same experiment as presented in Figure 3.2 but with a negative pressure difference, $\Delta p = -0.1$ Pa, and reported the numerical results in Table 3.4. We observe here again an excellent behavior of both Stokes and EDL error estimators with an asymptotical convergence of both Zienkiewicz-Zhu error estimators and the equivalence of both anisotropic error estimators with the true

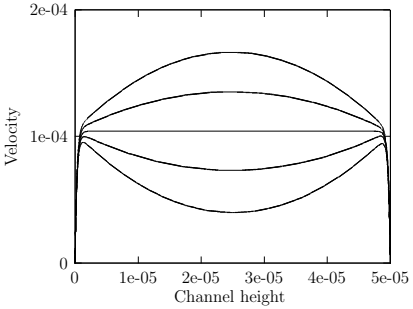

Figure 3.5. *Velocity profiles for various values of pressure difference Δp of the EOF problem in a straight channel. From bottom to top: Δp=-0.1, -0.05, 0, 0.05 and 0.1 Pa ($\overline{TOL}$=0.03125, 50 mesh generations).*

$\overline{\text{TOL}}$	ϵ^u_{rel}	ϵ^u_{abs}	$ei^{ZZ,u}$	$ei^{A,u}$	ϵ^ψ_{rel}	ϵ^ψ_{abs}	$ei^{ZZ,\psi}$	$ei^{A,\psi}$	nb_n	$\overline{ar}$	ar
0.25	0.116	4.8e-4	1.01	1.69	0.11	0.068	1.00	1.61	46	2123	16454
0.125	0.057	2.4e-4	1.00	1.73	0.054	0.033	1.00	1.63	90	3808	30483
0.0625	0.029	1.2e-4	1.00	1.87	0.027	0.016	1.00	1.76	170	6568	37498
0.03125	0.015	6.6e-5	1.00	1.88	0.014	0.0085	1.00	1.79	388	9428	100180

Table 3.4. *True error and effectivity indices for various values of the preset tolerance $\overline{TOL}$ of the EOF problem in a straight channel when Δp=-0.1 Pa.*

error. The error is still divided by two each time $\overline{\text{TOL}}$ is and the accuracy of our method is preserved, enable us to get an optimal solution with fewer triangles.

3.5 Numerical results

We now focus on injection and separation processes. In the first experiment we consider electrokinetic injection in a crossing microchannel and reproduce the numerical simulations taken from [76]. We apply our adaptive algorithm using conditions (3.13)-(3.16) and solve the numerical mass transport concentration problem driven by an EOF. Then we focus on a complete simulation of injection and separation technique in a more complex geometry that is to say in a multiple T-form channel, see [78] for similar numerical results and for experimental results. Finally,

the last numerical experiment concerns pressure-driven flow. We consider a double T-shape channel. The sample concentration is transported by a standard EOF and then a short sample plug is injected in the separation channel by a pressure pulse, see [89] for experimental results. As previously, we assume that the buffer solution has similar properties as water. All the parameters used in the following numerical simulations are reported in Table 3.2.

3.5.1 Electrokinetic injection in a crossing microchannel

We are interested now in the numerical simulation of the injection process in a crossing microchannel. We reproduce here the numerical simulation of electrokinetic sample focusing taken from [76]. Thus we consider a 2D crossing microchannel of width 24 μm and four channels of length $2e - 4$ m, as shown in Figure 3.6. There are four reservoirs, Sample, Waste, Analyze, Buffer, connected to the four ends of the microchannel. At time $t = 0$, the sample solution is filled in the Sample reservoir S. Then under an applied electric field the sample solution will be driven toward the Waste reservoir W passing through the cross section of the microchannel. This is the loading step. (the separation step will be considered in the next Subsections).

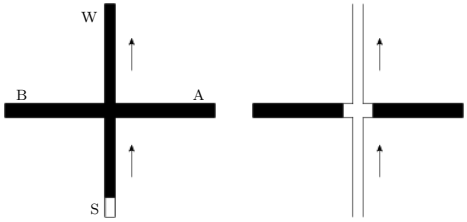

Figure 3.6. *Schematic representation of a loading process in a crossing microchannel.*

Reservoir (Volt)	case a	case b	case c
Waste	0	0	0
Sample	79.3	65.2	51.1
Buffer and Analyze	73.8	73.2	72.2

Table 3.6. *Applied potential to the four reservoirs during the injection process in a crossing microchannel.*

Channel (KV/cm)	case a	case b	case c
Waste	2.82	2.63	2.43
Sample	1.12	0.61	0.11
Buffer and Analyze	0.85	1.01	1.16

Table 3.5. *Electric field strength in the four channels during the injection process in a crossing microchannel.*

We consider the three different injection experiments presented in Figure 2 of [76] and take the same electric fields strength, see Table 3.5 for the electric fields strength and Table 3.6 for the corresponding applied potentials to the four ends of the microchannel. These potentials are computed by a simple calculus. First, we have to find the potential ϕ_c at the center of the crossing microchannel. For example, consider case a of Table 3.5. As the electric field strength gradient is linear from the Waste reservoir to the center of the crossing microchannel, ϕ_c satisfies

$$\frac{\phi_c - 0}{2.012e-4} = 2.82e5,$$

where we have imposed a zero value potential to the Waste reservoir and recall that the channel length and width are respectively $2e-4$ m and 24 μm. Then we find that $\phi_c = 56.7$ V and find the three others potentials, Sample, Buffer and Analyze, using ϕ_c and the corresponding channel electric field strength. Thus, we set the diffusion coefficient $\epsilon = 3e-10$, the potential at the walls $\zeta = -15$ mV, the molarity $M = 10^{-6}$, the final time $T = 1$ and assume that the pressure is constant in the whole domain. The initial condition c^0 for the convection-diffusion problem (3.8) is given by

$$c^0(x,y) = 0.5 - 0.5\tanh\left(\frac{y + 1.7e-4}{1e-6}\right).$$

We apply our space and time adaptive algorithm and build successive triangulations and choose appropriate time step such as conditions (3.13)-(3.16) are satisfied at each time t^n. For all the numerical simulations we set $\overline{\text{TOL}} = 0.25$ and we are only going to study the numerical simulations when varying TOL. The injection process corresponding to case a is reported in Figure 3.7 with a tolerance TOL=0.125. So at initial time, the concentration is filled in the Sample reservoir and moves into the injection channel toward the Waste reservoir. A zoom of the crossing channel is presented in Figure 3.8 at final time $T = 1$, where we have reported the adapted mesh, the streamline velocity field and the concentration field. We can observe that the mesh is refined near the channel walls and that

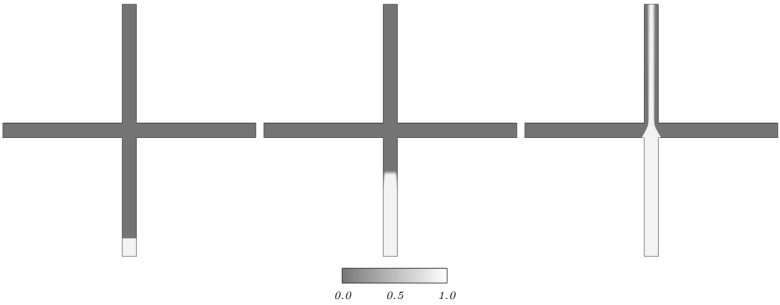

Figure 3.7. *From left to right: concentration at times t=0, 0.01, 1 during the injection process in a crossing microchannel with the electric field strength corresponding to case a and a tolerance TOL=0.125.*

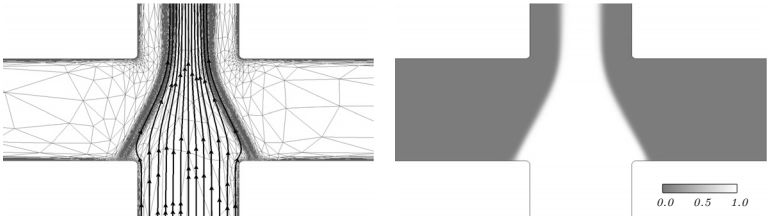

Figure 3.8. *Zoom on the adapted mesh, the streamline velocity field and concentration field at final time T=1 of the injection process in a crossing microchannel with the electric field strength corresponding to the case a and a tolerance TOL=0.125.*

it follows accurately the concentration field. Our adaptive algorithm allows us to solve efficiently the EDL problem and consequently the EOF without assuming a slip velocity condition along the channel walls as considered in [76]. In Figure 3.9, we present the evolution of the number of nodes and the time step size against time. We see that the number of nodes is quite constant during the injection process whereas the time step size can be decomposed into two phases. The first one consists in the injection process where the time step size slowly increases with the slight diffusion of the concentration field. This part is approximatively between times t=0 and t=0.25. The second one is between times t=0.25 and the final time $T = 1$ when the concentration field reaches the Waste reservoir. At time t=0.25, the concentration field completely pass through the injection channel and the time step size strongly increases until the end of the simulation time. We have reported in Table 3.7 the total number of time steps required to reach the final time for

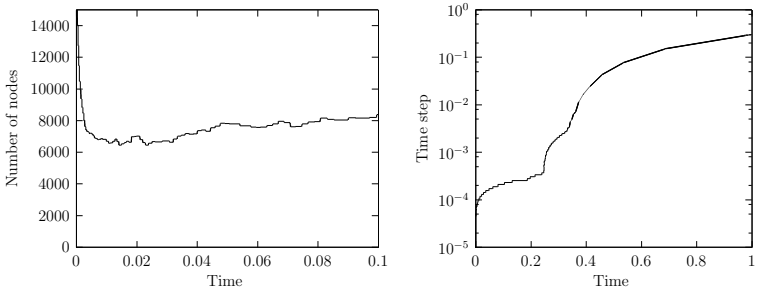

Figure 3.9. *Number of nodes (left) and time step size (right) with respect to time t of the injection process in a crossing microchannel with the electric field strength corresponding to case a and a tolerance TOL=0.125.*

TOL	nb_n	nb_τ	nb_m	$\overline{ar}$	ar
0.5	1305	690	79	208	6288
0.25	3979	932	102	127	7068
0.125	8063	1304	139	111	9305
0.0625	20896	1827	181	87	14504

Table 3.7. *Total number of nodes and time steps of the adapted solution at final time T=1 of the injection process in a crossing microchannel with the electric field strength corresponding to case a.*

several values of TOL. We observe that the optimal second order of convergence with respect to the time step is achieved as the number of time steps is multiplied by $\sqrt{2}$ when TOL is divided by two, see also Figure 3.10. Finally, in Figures 3.11 and 3.12 we present the numerical simulations at final time $T = 1$ of the three experiments taken from [76]. The corresponding results give a good agreement with the numerical simulations presented in Figure 2 of [76] and confirm the accuracy of our method based on a space and time adaptive finite element method.

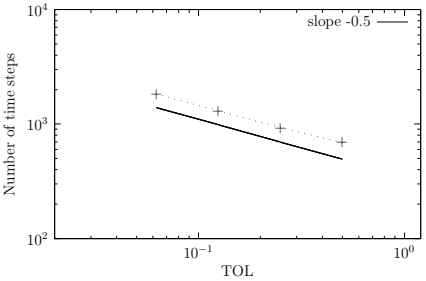

Figure 3.10. *Total number of time steps required to reach the final time T=1 with respect to the tolerance TOL of the injection process in a crossing microchannel with the electric field strength corresponding to case a.*

Reservoir	R_1	R_2	R_3	R_4	R_5	R_6
Injection (Volt)	42	120	42	0	0	0
Separation (Volt)	140	75	0	61	75	89
Channel width (μm)	100	100	100	80	100	80

Table 3.8. *Applied potentials to the six reservoirs during the injection and separation processes in a multiple T-form channel.*

3.5.2 Electrokinetic injection and separation in a multiple T-form channel

We now consider the injection and separation processes in a multiple T-form channel as shown in Figure 3.13 where $L = 7e-4$ m, $L_1 = 1e-4$ m and $H = 5e-4$ m. There are six reservoirs, R_1-R_6, connected to the six ends of the microchannel. During the injection process, the sample concentration moves from reservoir R2 to reservoirs R4, R5 and R6, passing through the triple cross section area. Then during the separation process, the part of the sample loaded in the triple cross section will be driven through the separation channel, towards the reservoir R3, see Figure 3.13. In Table 3.8, we have reported the values of the electric potentials applied to the six reservoirs during the loading and dispensing step and the diameters of the different channels of the microchannel.

We set the diffusion coefficient $\epsilon = 6.9e-11$, the potential at the walls

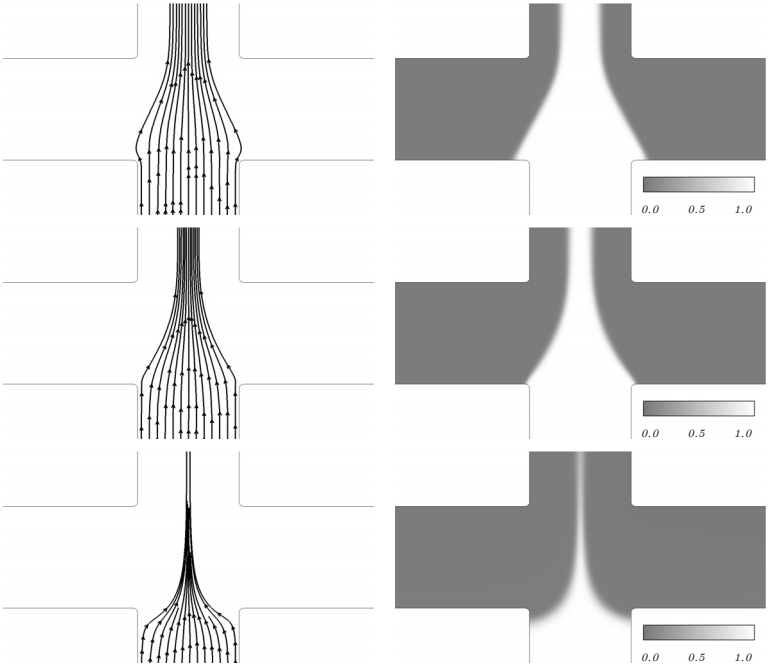

Figure 3.11. *Velocity streamlines and concentration fields of the injection process in a crossing microchannel at final time T=1 obtained with a tolerance TOL=0.125. From top to bottom: case a, b, c.*

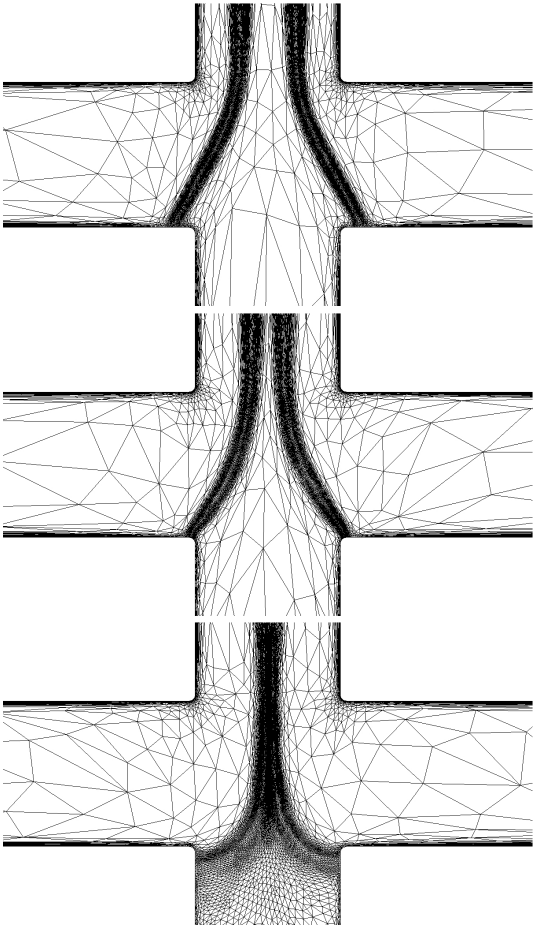

Figure 3.12. *Adapted meshes of the injection process in a crossing microchannel at final time T=1 obtained with a tolerance TOL=0.125. From top to bottom: case a, b, c with respectively 7141, 5743 and 8236 nodes.*

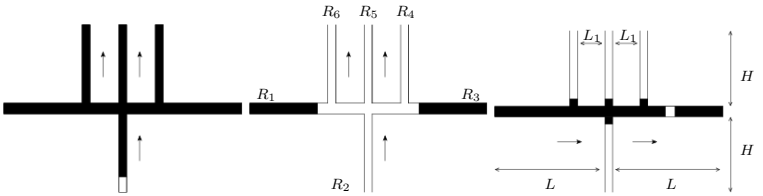

Figure 3.13. *Schematic representation of a loading and separation processes in a multiple T-form channel.*

$\zeta = -75$ mV, the molarity $M = 10^{-8}$, the final time $T = 0.6$ and assume that the pressure is constant in the whole domain. The initial condition c^0 for the convection-diffusion problem (3.8) is given by

$$c^0(x, y) = 0.5 - 0.5 \tanh\left(\frac{y + 4.4e - 4}{1e - 6}\right).$$

We apply our space and time adaptive algorithm and build successive triangulations and choose appropriate time step such as conditions (3.13)-(3.16) are satisfied at each time t^n. The numerical simulation is reported in Figure 3.14 with $\overline{\text{TOL}} = \text{TOL} = 0.25$. So at initial time, the sample concentration is filled in the reservoir R2 and then moves towards the three reservoirs R4, R5 and R6, passing through the triple cross section of the microchannel. This corresponds to the injection process and is reported on the three first pictures of Figure 3.14. The first picture is the initial time. In the second picture, the sample separates in three. The sample starts to join the channels corresponding to the reservoirs R4 and R6. It has already joined that of corresponding to the reservoir R5. Finally, the third picture is the stationary state of the injection process. Then at time t=0.3, all the potentials applied to the six reservoirs change and the sample concentration is injected in the separation channel, towards the reservoir R3. This is reported on the three last pictures of Figure 3.14. In the first of the three last pictures, the sample plug starts to move in the separation channel. In the second picture, this plug is now injected and its front almost reaches the reservoir R3. Finally in the third picture, the plug completely pass through the reservoir R3 and leaves the computation domain.

In Figure 3.15, we present the evolution of the number of nodes and the time step size against time. We see that the number of nodes is quite constant in the beginning when the sample concentration moves to the triple cross section area. Then it increases as the sample concentration separates in three, stays approximatively constant until the solution completely pass through the three reservoirs R4,

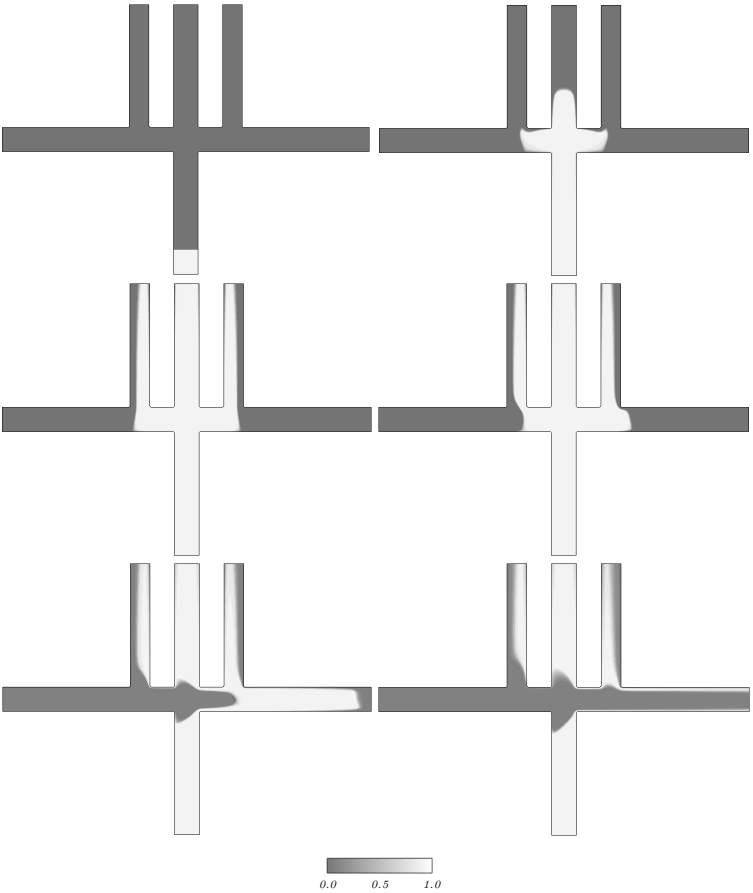

Figure 3.14. *From top to bottom, left to right: solutions at times t=0, 0.11, 0.3, 0.31, 0.4, 0.6 of the injection and separation processes in a multiple T-form channel with* $\overline{TOL}$*=TOL=0.25.*

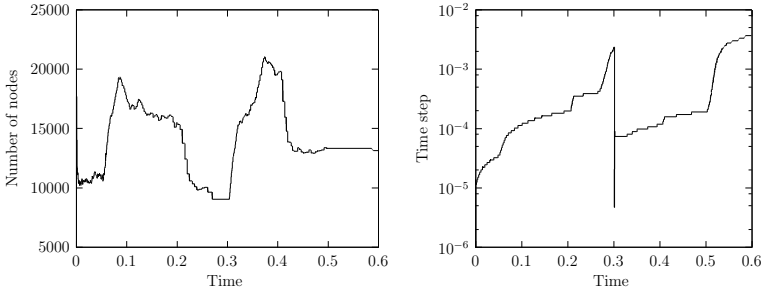

Figure 3.15. *Number of nodes (left) and time step size (right) with respect to time t of the injection and separation processes in a multiple T-form channel with* $\overline{TOL}$*=TOL=0.25.*

R5 and R6. At that time the solution reaches the stationary state of the injection process and the number of nodes decreases. Then the potentials change and the separation process begins. The number of nodes then increases until the front of the injected plug concentration reaches the reservoir R3. At that moment the number of nodes starts to decrease. As regards the time step evolution, it can be decomposed into two parts, the injection process and the separation process. During the injection process, we can distinguish three steps. The first one concerns the time when the sample concentration moves towards the triple cross section area. The second one is the transport of the sample concentration in the direction of the three reservoirs, R4, R5 and R6, passing through the triple cross section area. Finally the third one corresponds to the time when the solution reaches the stationary state of the injection process. During these three steps the time step size increases gradually. At time t=0.3, the potentials change and the separation process begins. At that time, the time step size drops significantly. Then it increases until the time t=0.5 corresponding to the time when the sample plug leaves the computation domain. Finally, in Figures 3.16 and 3.17 we reported the adapted mesh, the velocity streamlines and the concentration field corresponding to the times t=0.11 and t=0.31 of the numerical simulation presented in Figure 3.14.

3.5.3 Pressure pulse injection

We end with a numerical experiment of injection and separation processes when the sample concentration is transported by a standard EOF and injected in the separation channel by a pressure pulse, see Figure 3.18. We consider a double

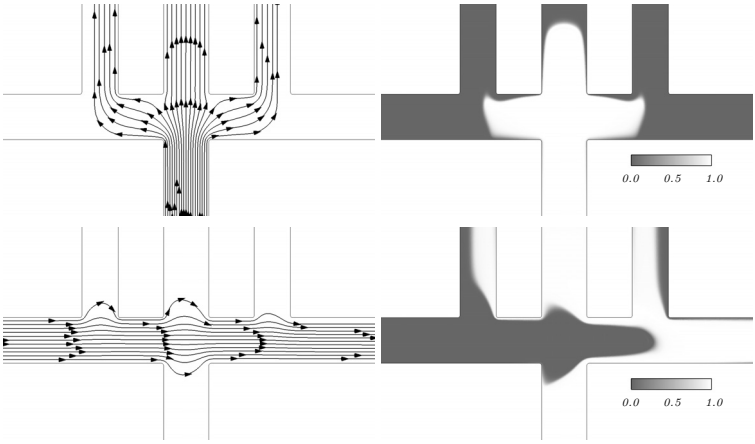

Figure 3.16. *Velocity streamlines and concentration fields at times t=0.11 (top) and t=0.31 (bottom) of the injection and separation processes in a multiple T-form channel with $\overline{TOL}$=TOL=0.25.*

T-form channel as shown in Figure 3.18. There are four reservoirs S, B, A, W, connected to the four ends of the microchannel. At initial time, the sample concentration is filled in the reservoir S. Then under an applied electric field, it moves towards the reservoir W. Note that because of the set of electric potentials applied to the four reservoirs, the sample concentration does not move to the others reservoirs. During the pressure pulse period, we impose a constant positive pressure value at the boundary corresponding to the entrance reservoir S and set the three other reservoirs boundaries to zero. This corresponds to adding an extra term to the right hand side of the finite element formulation (3.11). In Table 3.9, we have reported the potential value at the four reservoirs, the imposed pressure value at each reservoir during the pressure pulse period and the diameter of the different channels of the microchannel. We set the diffusion coefficient $\epsilon = 6.9e-11$, the potential at the walls $\zeta = -75$ mV, the molarity $M = 10^{-7}$, the final time $T = 1.5$ and we assume that the pressure is constant in the whole domain except during the pressure pulse period. The initial condition c^0 for the convection-diffusion problem (3.8) is given by

$$c^0(x,y) = 0.5 - 0.5\tanh\left(\frac{x-2e-4}{1e-6}\right).$$

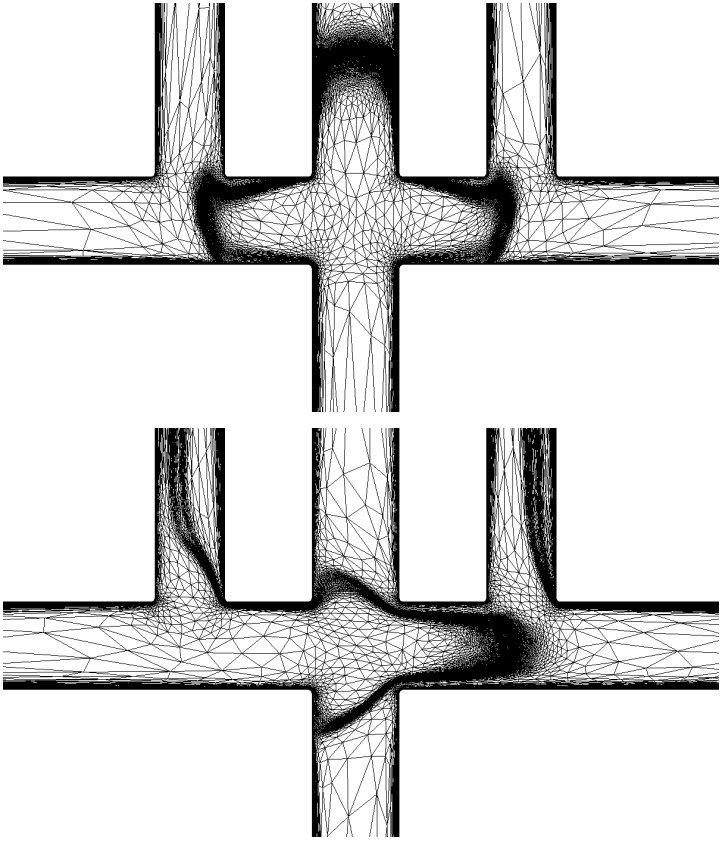

Figure 3.17. *Adapted meshes at times t=0.11 (top, 16941 nodes) and t=0.31 (bottom, 19921 nodes) of the injection and separation processes in a multiple T-form channel with* $\overline{TOL}$*=TOL=0.25.*

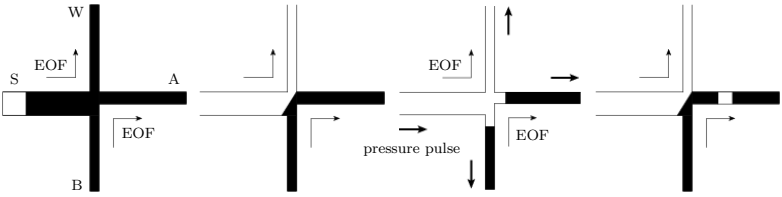

Figure 3.18. *Schematic representation of a loading and separation processes when the sample is transported by a standard EOF and separated by a pressure pulse.*

Reservoir	S	B	A	W
Potential (Volt)	200	270	0	0
Pressure (Pa)	20	0	0	0
Channel length (m)	1e-3	9e-4	1e-3	1e-3
Channel width (μm)	200	100	100	100

Table 3.9. *Applied potential to the four reservoirs and imposed pressure value during the pressure pulse period when the sample is transported by a standard EOF and separated by a pressure pulse.*

We apply our space and time adaptive algorithm and build successive triangulations and choose appropriate time step such as conditions (3.13)-(3.16) are satisfied at each time t^n. The numerical simulation is reported in Figure 3.19 with $\overline{\text{TOL}} = \text{TOL} = 0.25$. So at initial time, the concentration is filled in the reservoir S and moves towards the reservoir W (top pictures of Figure 3.19). After time t=0.8, when the solution reaches the stationary state of the injection process, we applied a pressure pulse of 20 Pa at the reservoir S during a period of 20 ms. Thus, the sample concentration moves towards the three reservoirs B, A, W (first bottom picture of Figure 3.19). After this period, the pressure becomes again constant in the whole domain and the sample injected in the separation channel moves towards the reservoir A (second and third bottom pictures of Figure 3.19).

In Figure 3.20, we have reported the evolution of the number of nodes and time step size against time. We can see that the number of nodes suffers of many oscillations except when the solution is at a stationary state which corresponds to a constant number of nodes. A important increase is observed when the pressure pulse is applied. The time step size can be decomposed into three phases. The first

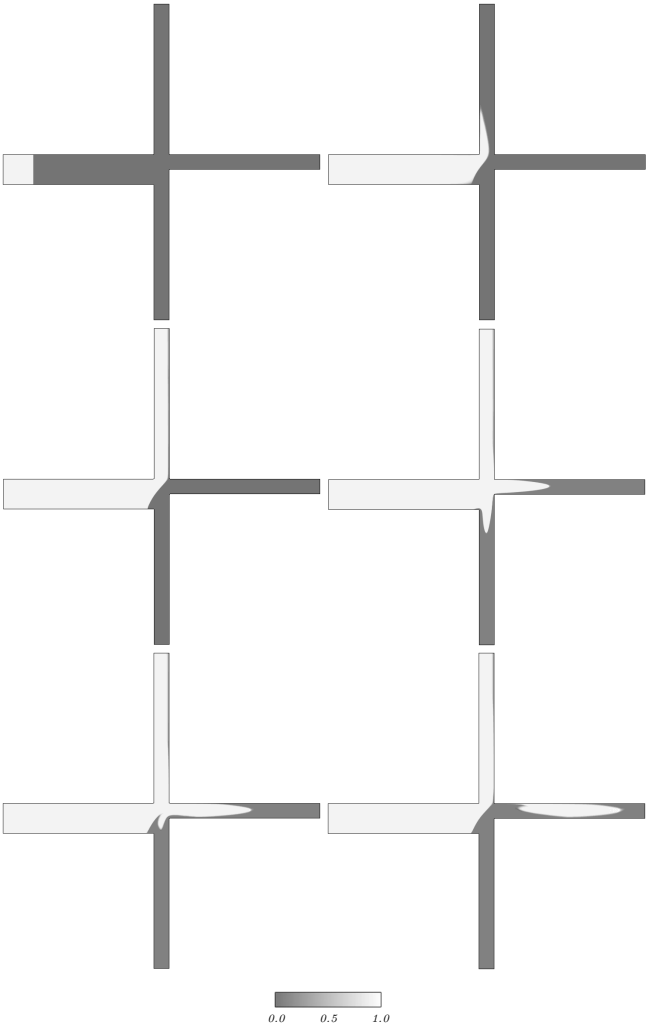

Figure 3.19. *From top to bottom, left to right: solutions at times t=0, 0.28, 0.85, 0.87, 0.90, 1.5 of a loading and separation processes when the sample is transported by a standard EOF and separated by a pressure pulse with* $\overline{TOL}$*=TOL=0.25.*

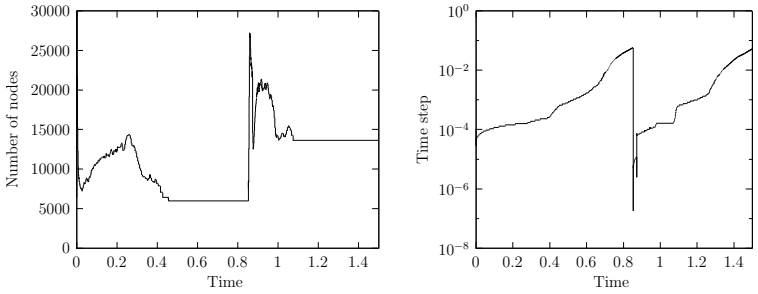

Figure 3.20. *Number of nodes (left) and time step size (right) with respect to time t of a loading and separation processes when the sample is transported by a standard EOF and separated by a pressure with $\overline{TOL}$=TOL=0.25.*

one is the injection process when the sample concentration moves from reservoir S to W. The time step size increases gradually at this moment with a stronger increase when the solution reaches the stationary state of the injection process. The second phase concerns the applied pressure pulse. At that time, the time step size drops significantly then stays approximatively constant during the applied pressure pulse period. At the end of this period, the time step size drops again and then increases. This is the third step where the sample plug injected in the separation channel moves towards the reservoir A. Around time t=1, the sample plug leaves the computation domain and the time step size increases strongly until the end of the simulation time.

Finally, we reported in Figures 3.21 and 3.22, the velocity streamlines, the concentration field and the adapted mesh corresponding to the times t=0.85 and t=0.87 of the numerical simulation presented in Figure 3.19.

3.6 Conclusion

We have applied an adaptive finite element method to solve the electroosmotic transport of a sample concentration through a network of microchannels. This method enables us to fully solve the EDL potential near the walls of the microchannel required to solve the fluid flow velocity. In the numerical simulations considered in this Chapter, the ratio between the channel height and the Debye layer is about 100. Solving accurately the electric wall potential problem with a

standard finite element method would lead to an enormous number of nodes. The use of an adaptive method reduces drastically this number and allows to compute accurately this potential. Moreover, the adaptive algorithm coupled a space adaptation with a time adaptation. It becomes very useful for instance when the solution reaches the stationary state of the injection process. During that time, higher time step are used, and when the separation process begins, the time step size automatically reduces in order to compute an accurate solution. The results obtained prove that the method is efficient and robust and provides a useful tool to compute electroosmotic sample transport processes in complex microfluidic chips. All the numerical experiments are done in two-dimensional space. We are looking forward to extend these results to the three-dimensional case using the MeshAdapt software [90], especially for the numerical simulation of the pressure pulse injection where the depth of the microchannels can have a significant impact on the velocity field rate.

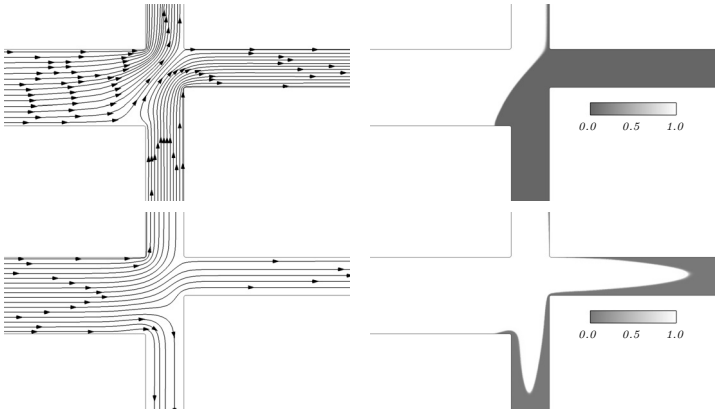

Figure 3.21. *Velocity streamlines and concentration fields at times t=0.85 (top) and t=0.87 (bottom) of a loading and separation processes when the sample is transported by a standard EOF and separated by a pressure pulse with* $\overline{TOL}$*=TOL=0.25.*

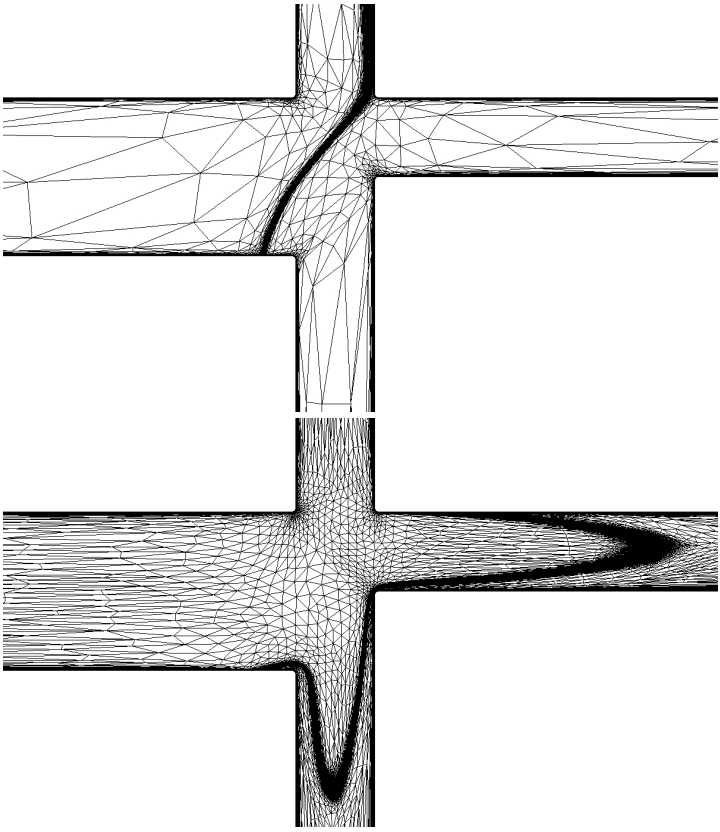

Figure 3.22. *Adapted meshes at times t=0.85 (top, 5987 nodes) and t=0.87 (bottom, 21722 nodes) of a loading and separation processes when the sample is transported by a standard EOF and separated by a pressure pulse with* $\overline{TOL}$*=TOL=0.25.*

Conclusion

A space and time adaptive method for the numerical simulation of electroosmotic transport of a sample concentration within a network of microchannels is implemented.

The main difficulty in such problem is the computation of the electric double layer potential which drops rapidly across the Debye layer from a constant value at the microchannel walls, to zero in a bulk region. As the ratio between the microchannel diameter and the Debye layer length can be up to 10^4, specific numerical method has to be used to compute accurately the electroosmotic flow with a reasonable computation cost. This has been successfully addressed using an adaptive finite element method with large aspect ratio. Thus, on one hand, the electroosmotic flow has been solved accurately, despite the presence of strong boundary layers, and on the other hand, this approach allowed to follow with precision the transport of a sample concentration through complex geometries of microchannels. Obtained results show that this method is efficient and robust and give good agreement with works of other authors.

Another important feature of this work is the use of an adaptive time step method. Usually, adaptive method only focus on space adaptation. Of course, generating meshes that fit ideally to the finite element solution is an efficient manner to improve its quality. However, if the adaptive method can couple a time adaptive procedure to the one in space, the numerical solution would obviously be even more accurate. For this purpose, time error estimators have first been derived for two model problems, that is to say the linear heat equation and the time-dependent convection-diffusion problem, both discretized in time with the Crank-Nicolson scheme. Optimality of both time error estimators have been obtained using a continuous piecewise quadratic time reconstruction and numerical results reported show that these estimators provide an efficient tool to improve the accuracy of a finite element solution. Nevertheless, for a complete theoretical study of these error estimators, the derivation of lower bounds such as the one presented in [29] in the case of anisotropic meshes is still needed.

Bibliography

[1] B. Zhang, H. Liu, B. L. Karger, and F. Foret. Microfabricated devices for capillary electrophoresis-electrospray mass spectrometry. *Anal. Chem.*, 71:3258–3264, 1999.

[2] S. Liu, Y. Shi, W. W. Ja, and R. A. Mathies. Optimization of high-speed dna sequencing on microfabricated capillary electrophoresis channels. *Anal. Chem.*, 71:566–573, 1999.

[3] R. A. Mathies and X. C. Huang. Capillary array electrophoresis: an approach to high-speed, high-throughput dna sequencing. *Nature*, 359:167–169, 1992.

[4] A. T. Woolley and R. A. Mathies. Ultra-high-speed dna sequencing using capillary electrophoresis chips. *Anal. Chem.*, 67:3676–3680, 1995.

[5] N. J. Munro, Z. Huang, D. N. Finegold, and J. P. Landers. Indirect fluorescence detection of amino acids on electrophoretic microchips. *Anal. Chem.*, 72:2765–2773, 2000.

[6] R. J. Hunter. *Zeta Potential in Colloid Science: Principles and Applications*. Academic Press, London, 1988.

[7] R. F. Probstein. *Physicochemical Hydrodynamics : An Introduction*. Wiley-Interscience, New York, 1994.

[8] D. Li. *Electrokinetics in Microfluidics*. Academic Press, New York, USA, 2004.

[9] I. Babuška and W. C. Rheinboldt. Error estimates for adaptive finite element computations. *SIAM J. Numer. Anal.*, 15(4):736–754, 1978.

[10] I. Babuška and W. C. Rheinboldt. A posteriori error estimators in the finite element method. *Internat. J. Numer. Meth. Engrg.*, 12:1597–1615, 1978.

[11] M. Ainsworth and J. T. Oden. *A posteriori error estimation in finite element analysis*. Pure and Applied Mathematics (New York). Wiley-Interscience [John Wiley & Sons], New York, 2000.

[12] R. Verfürth. A Review of A Posteriori Error Estimation and Adaptive Mesh-Refinement Techniques. *Wiley-Teubner*, 1996.

[13] W. Bangerth and R. Rannacher. *Adaptive finite element methods for differential equations*. Lectures in Mathematics ETH Zürich. Birkhäuser Verlag, Basel, 2003.

[14] C. Johnson. Adaptive finite element methods for conservation laws. In *Advanced numerical approximation of nonlinear hyperbolic equations (Cetraro, 1997)*, volume 1697 of *Lecture Notes in Math.*, pages 269–323. Springer, Berlin, 1998.

[15] G. Kunert. An a posteriori residual error estimator for the finite element method on anisotropic tetrahedral meshes. *Numer. Math.*, 86(3):471–490, 2000.

[16] G. Kunert. Toward anisotropic mesh construction and error estimation in the finite element method. *Numer. Methods Partial Differential Equations*, 18(5):625–648, 2002.

[17] G. Kunert and S. Nicaise. Zienkiewicz-Zhu error estimators on anisotropic tetrahedral and triangular finite element meshes. *M2AN Math. Model. Numer. Anal.*, 37(6):1013–1043, 2003.

[18] G. Kunert and R. Verfürth. Edge residuals dominate a posteriori error estimates for linear finite element methods on anisotropic triangular and tetrahedral meshes. *Numer. Math.*, 86(2):283–303, 2000.

[19] T. Apel and G. Lube. Anisotropic mesh refinement in stabilized Galerkin methods. *Numer. Math.*, 74(3):261–282, 1996.

[20] T. Apel. *Anisotropic finite elements: local estimates and applications*. Advances in Numerical Mathematics. B. G. Teubner, Stuttgart, 1999.

[21] K. G. Siebert. An a posteriori error estimator for anisotropic refinement. *Numer. Math.*, 73(3):373–398, 1996.

[22] E. Burman, A. Jacot, and M. Picasso. Adaptive finite elements with high aspect ratio for the computation of coalescence using a phase-field model. *J. Comput. Phys.*, 195(1):153–174, 2004.

[23] L. Formaggia and S. Perotto. Anisotropic error estimates for elliptic problems. *Numer. Math.*, 94(1):67–92, 2003.

[24] L. Formaggia and S. Perotto. New anisotropic a priori error estimates. *Numer. Math.*, 89(4):641–667, 2001.

[25] W. G. Habashi, M. Fortin, J. Dompierre, M. G. Vallet, and Y. Bourgault. Anisotropic mesh adaptation: a step towards a mesh-independent and user-independent CFD. In *Barriers and challenges in computational fluid dynamics (Hampton, VA, 1996)*, volume 6 of *ICASE/LaRC Interdiscip. Ser. Sci. Eng.*, pages 99–117. Kluwer Acad. Publ., Dordrecht, 1998.

[26] F. Alauzet, P. L. George, B. Mohammadi, P. Frey, and H. Borouchaki. Transient fixed point-based unstructured mesh adaptation. *Internat. J. Numer. Methods Fluids*, 43(6-7):729–745, 2003. ECCOMAS Computational Fluid Dynamics Conference, Part II (Swansea, 2001).

[27] J.-F. Remacle, X. Li, M. S. Shephard, and J. E. Flaherty. Anisotropic adaptive simulation of transient flows using discontinuous Galerkin methods. *Internat. J. Numer. Methods Engrg.*, 62(7):899–923, 2005.

[28] M. Picasso. Numerical study of the effectivity index for an anisotropic error indicator based on Zienkiewicz-Zhu error estimator. *Comm. Numer. Methods Engrg.*, 19(1):13–23, 2003.

[29] M. Picasso. Adaptive finite elements with large aspect ratio based on an anisotropic error estimator involving first order derivatives. *Comput. Methods Appl. Mech. Engrg.*, 196(1-3):14–23, 2006.

[30] M. Picasso. An anisotropic error indicator based on Zienkiewicz-Zhu error estimator: application to elliptic and parabolic problems. *SIAM J. Sci. Comput.*, 24(4):1328–1355 (electronic), 2003.

[31] E. Burman and M. Picasso. Anisotropic, adaptive finite elements for the computation of a solutal dendrite. *Interfaces Free Bound.*, 5(2):103–127, 2003.

[32] G. Akrivis, C. Makridakis, and R. H. Nochetto. A posteriori error estimates for the Crank-Nicolson method for parabolic equations. *Math. Comp.*, 75(254):511–531 (electronic), 2006.

[33] M. Picasso. An adaptive algorithm for the Stokes problem using continuous, piecewise linear stabilized finite elements and meshes with high aspect ratio. *Appl. Numer. Math.*, 54(3-4):470–490, 2005.

[34] A. Lozinski, M. Picasso, and V. Prachittham. An anisotropic error estimator for the Crank-Nicolson method: Application to a parabolic problem. *Preprint*, 2008.

[35] M. Picasso and V. Prachittham. An adaptive algorithm for the Crank-Nicolson scheme applied to a time-dependent convection-diffusion problem. *Preprint*, 2008.

[36] V. Prachittham, M. Picasso, and M. A. M. Gijs. Adaptive finite elements with large aspect ratio for electroosmosis and pressure-driven microflows. *Preprint*, 2008.

[37] M. Ainsworth and J. T. Oden. A unified approach to a posteriori error estimation using element residual methods. *Numer. Math.*, 65(1):23–50, 1993.

[38] T. Apel and S. Nicaise. The finite element method with anisotropic mesh grading for elliptic problems in domains with corners and edges. *Math. Methods Appl. Sci.*, 21(6):519–549, 1998.

[39] R. Verfürth. A posteriori error estimates for nonlinear problems. Finite element discretizations of elliptic equations. *Math. Comp.*, 62(206):445–475, 1994.

[40] C. Bernardi and R. Verfürth. Adaptive finite element methods for elliptic equations with non-smooth coefficients. *Numer. Math.*, 85(4):579–608, 2000.

[41] M. Picasso. Adaptive finite elements for a linear parabolic problem. *Comput. Methods Appl. Mech. Engrg.*, 167(3-4):223–237, 1998.

[42] A. Bergam, C. Bernardi, and Z. Mghazli. A posteriori analysis of the finite element discretization of some parabolic equations. *Math. Comp.*, 74(251):1117–1138 (electronic), 2005.

[43] Z. Chen and J. Feng. An adaptive finite element algorithm with reliable and efficient error control for linear parabolic problems. *Math. Comp.*, 73(247):1167–1193 (electronic), 2004.

[44] K. Eriksson and C. Johnson. Adaptive finite element methods for parabolic problems. I. A linear model problem. *SIAM J. Numer. Anal.*, 28(1):43–77, 1991.

[45] K. Eriksson and C. Johnson. Adaptive finite element methods for parabolic problems. IV. Nonlinear problems. *SIAM J. Numer. Anal.*, 32(6):1729–1749, 1995.

[46] R. Verfürth. A posteriori error estimates for finite element discretizations of the heat equation. *Calcolo*, 40(3):195–212, 2003.

[47] G. Akrivis, C. Makridakis, and R. H. Nochetto. Optimal order a posteriori error estimates for a class of runge-kutta and galerkin methods. *In preparation*, 2007.

[48] R. Dautray and J.-L. Lions. *Mathematical analysis and numerical methods for science and technology. Vol. 5.* Springer-Verlag, Berlin, 1992. Evolution problems. I, With the collaboration of Michel Artola, Michel Cessenat and Hélène Lanchon, Translated from the French by Alan Craig.

[49] H. Borouchaki and G. Laug. The BL2D Mesh Generator : Beginner's Guide, User's and Programmer's Manual. *Technical report RT-0194, Institut National de Recherche en Informatique et Automatique (INRIA), Rocquencourt, 78153 Le Chesnay, France*, 1996.

[50] S. Micheletti, S. Perotto, and M. Picasso. Stabilized finite elements on anisotropic meshes: a priori error estimates for the advection-diffusion and the Stokes problems. *SIAM J. Numer. Anal.*, 41(3):1131–1162 (electronic), 2003.

[51] Ph. Clément. Approximation by finite element functions using local regularization. *Rev. Française Automat. Informat. Recherche Opérationnelle Sér. RAIRO Analyse Numérique*, 9(R-2):77–84, 1975.

[52] O. C. Zienkiewicz and J. Z. Zhu. A simple error estimator and adaptive procedure for practical engineering analysis. *Internat. J. Numer. Methods Engrg.*, 24(2):337–357, 1987.

[53] O. C. Zienkiewicz and J. Z. Zhu. The superconvergent patch recovery and a posteriori error estimates. I. The recovery technique. *Internat. J. Numer. Methods Engrg.*, 33(7):1331–1364, 1992.

[54] A. Naga and Z. Zhang. A posteriori error estimates based on the polynomial preserving recovery. *SIAM J. Numer. Anal.*, 42(4):1780–1800 (electronic), 2004.

[55] Z. Zhang and A. Naga. A new finite element gradient recovery method: superconvergence property. *SIAM J. Sci. Comput.*, 26(4):1192–1213 (electronic), 2005.

[56] P. Houston, R. Rannacher, and E. Süli. A posteriori error analysis for stabilised finite element approximations of transport problems. *Comput. Methods Appl. Mech. Engrg.*, 190(11-12):1483–1508, 2000.

[57] A. Papastavrou and R. Verfürth. A posteriori error estimators for stationary convection-diffusion problems: a computational comparison. *Comput. Methods Appl. Mech. Engrg.*, 189(2):449–462, 2000.

[58] R. Verfürth. Robust a posteriori error estimates for stationary convection-diffusion equations. *SIAM J. Numer. Anal.*, 43(4):1766–1782 (electronic), 2005.

[59] G. Sangalli. Robust a-posteriori estimator for advection-diffusion-reaction problems. *Math. Comp.*, 77(261):41–70 (electronic), 2008.

[60] L. Formaggia, S. Micheletti, and S. Perotto. Anisotropic mesh adaptation in computational fluid dynamics: application to the advection-diffusion-reaction and the Stokes problems. *Appl. Numer. Math.*, 51(4):511–533, 2004.

[61] L. Formaggia, S. Perotto, and P. Zunino. An anisotropic a-posteriori error estimate for a convection-diffusion problem. *Comput. Vis. Sci.*, 4(2):99–104, 2001. Second AMIF International Conference (Il Ciocco, 2000).

[62] T. Apel and S. Nicaise. A posteriori error estimations of a SUPG method for anisotropic diffusion-convection-reaction problems. *C. R. Math. Acad. Sci. Paris*, 345(11):657–662, 2007.

[63] R. Verfürth. Robust a posteriori error estimates for nonstationary convection-diffusion equations. *SIAM J. Numer. Anal.*, 43(4):1783–1802 (electronic), 2005.

[64] A. Ern and J. Proft. A posteriori discontinuous Galerkin error estimates for transient convection-diffusion equations. *Appl. Math. Lett.*, 18(7):833–841, 2005.

[65] V. Dolejší and M. Feistauer. Error estimates of the discontinuous Galerkin method for nonlinear nonstationary convection-diffusion problems. *Numer. Funct. Anal. Optim.*, 26(3):349–383, 2005.

[66] L. P. Franca, S. L. Frey, and T. J. R. Hughes. Stabilized finite element methods. I. Application to the advective-diffusive model. *Comput. Methods Appl. Mech. Engrg.*, 95(2):253–276, 1992.

[67] R. Codina. Comparison of some finite element methods for solving the diffusion-convection-reaction equation. *Comput. Methods Appl. Mech. Engrg.*, 156(1-4):185–210, 1998.

[68] H.-G. Roos, M. Stynes, and L. Tobiska. *Numerical methods for singularly perturbed differential equations*, volume 24 of *Springer Series in Computational Mathematics*. Springer-Verlag, Berlin, 1996. Convection-diffusion and flow problems.

[69] P. Houston and E. Süli. Adaptive Lagrange-Galerkin methods for unsteady convection-diffusion problems. *Math. Comp.*, 70(233):77–106, 2001.

[70] N. A. Patankar and H. H. Hu. Numerical simulation of electroosmotic flow. *Analytical Chemistry*, 70(9):1870–1881, 1998.

[71] I. Meisel and P. Ehrhard. Electrically-excited (electroosmotic) flows in microchannels for mixing applications. *European Journal of Mechanics*, 25(4):491–504, 2006.

[72] S. Ghosal. Electrokinetic flow and dispersion in capillary electrophoresis. *Annual Review of Fluid Mechanics*, 38(1):309–338, 2006.

[73] P. D. Grossman and J. C. Colburn. *Capillary Electrophoresis: Theory and Practice*. Paul D. Grossman and Joel C. Colburn (Eds.) Academic Press, San Diego, California, USA, 1992.

[74] F. Bianchi, R. Ferrigno, and H. H. Girault. Finite element simulation of an electroosmotic-driven flow division at a t-junction of microscale dimensions. *Anal. Chem.*, 72:1987–1993, 2000.

[75] L. Ren, D. Sinton, and D. Li. Numerical simulation of microfluidic injection processes in crossing microchannels. *J. Micromech. Microeng.*, 13:739–747, 2003.

[76] S. V. Ermakov, S. C. Jacobson, and J. M. Ramsey. Computer simulations of electrokinetic transport in microfabricated channel structures. *Anal. chem.*, 70:4494–4504, 1998.

[77] S. V. Ermakov, S. C. Jacobson, and J. M. Ramsey. Computer simulations of electrokinetic injection techniques in microfluidic devices. *Anal. chem.*, 72:3512–3517, 2000.

[78] L. M. Fu, R. J. Yang, G. B. Lee, and H. H. Liu. Electrokinetic injection techniques in microfluidic chips. *Anal. chem.*, 74:5084–5091, 2002.

[79] C. H. Tsai, R. J. Yang, C. H. Tai, and L. M. Fu. Numerical simulation of electrokinetic injection techniques in capillary electrophoresis microchips. *Electrophoresis*, 26:674–686, 2005.

[80] P. Dutta, A. Beskok, and T. C. Warburton. Numerical simulation of mixed electroosmotic/pressure driven microflows. *Numerical Heat Transfer, Part A*, 41:131–148, 2002.

[81] P. Dutta and A. Beskok. Analytical solution of combined electroosmotic/pressure driven flows in two-dimensional straight channels: Finite debye layer effects. *Electrophoresis*, 73:1979–1986, 2001.

[82] J. I. Molho, A. E. Herr, B. P. Mosier, J. G. Santiago, T. W. Kenny, R. A. Brennen, G. B. Gordon, and B. Mohammadi. Optimization of turn geometries for microchip electrophoresis. *Anal. chem.*, 73:1350–1360, 2001.

[83] B. Mohammadi and J. G. Santiago. Simulation and design of extraction and separation fluidic devices. *M2AN Math. Model. Numer. Anal.*, 35(3):513–523, 2001.

[84] D. A. Saville. Electrokinetic effects with small particles. *Annu. Rev. Fluid Mech.*, 9:321–337, 1977.

[85] T. J. R. Hughes, L. P. Franca, and M. Balestra. A new finite element formulation for computational fluid dynamics. V. Circumventing the Babuška-Brezzi condition: a stable Petrov-Galerkin formulation of the Stokes problem accommodating equal-order interpolations. *Comput. Methods Appl. Mech. Engrg.*, 59(1):85–99, 1986.

[86] T. J. R. Hughes. *The finite element method*. Prentice Hall Inc., Englewood Cliffs, NJ, 1987. Linear static and dynamic finite element analysis, With the collaboration of Robert M. Ferencz and Arthur M. Raefsky.

[87] A. Quarteroni and A. Valli. *Numerical approximation of partial differential equations*, volume 23 of *Springer Series in Computational Mathematics*. Springer-Verlag, Berlin, 1994.

[88] A. Ern and J.-L. Guermond. *Theory and practice of finite elements*, volume 159 of *Applied Mathematical Sciences*. Springer-Verlag, New York, 2004.

[89] F. Lacharme and M. A. M. Gijs. Pressure injection in continuous sample flow electrophoresis microchips. *Sensors and Actuators B: Chemical*, 117:384–390, 2006.

[90] Distene S.A.S., Pôle Teratec - BARD-1, Domaine du Grand Rué, 91680 Bruyères-le-Chatel, France. *MeshAdapt : A mesh adaptation tool, User's manual Version 3.0*, 2003.

Curriculum Vitæ

I was born on July 17th, 1980 in Salins-les-Bains, France. I have done my secondary education in Salins-les-Bains and obtained in 1998 the Baccalauréat Scientifique (option mathematics, mention AB). In 2005, I received a master degree in applied mathematics (mention TB) from the University of Franche-Comté, France, after having done my master thesis project at the Swiss Federal Institute of Technology in Lausanne (EPFL). Since 2005, I have been working as a research assistant in the Chair of Numerical Analysis and Simulation of Prof. Jacques Rappaz. The theme of my research is the numerical simulation of electroosmotic-driven microflows and adaptive finite element method.